

## Durham E-Theses

---

### *The Electrical and Mechanical Study of the Flexible Organic Light Emitting Diodes*

CHIANG, CHIEN-JUNG

#### How to cite:

---

CHIANG, CHIEN-JUNG (2011) *The Electrical and Mechanical Study of the Flexible Organic Light Emitting Diodes*, Durham theses, Durham University. Available at Durham E-Theses Online:  
<http://etheses.dur.ac.uk/907/>

#### Use policy

---

The full-text may be used and/or reproduced, and given to third parties in any format or medium, without prior permission or charge, for personal research or study, educational, or not-for-profit purposes provided that:

- a full bibliographic reference is made to the original source
- a [link](#) is made to the metadata record in Durham E-Theses
- the full-text is not changed in any way

The full-text must not be sold in any format or medium without the formal permission of the copyright holders.

Please consult the [full Durham E-Theses policy](#) for further details.

## Abstract

This work begins from depositing the same organic light emitting diode (OLED) structure on the glass substrate and the Polyethylene terephthalate (PET) substrate. The result suggests that the transparency of the substrates, the microcavity effect arising from different anode thicknesses and the surface roughness of the anode all come into play to lower the device efficiency of the PET device. The Young's moduli of the Tris-(8-hydroxyquinoline) aluminum (Alq<sub>3</sub>) and N,N'-Bis(naphthalen-1-yl)-N,N'-bis(phenyl)benzidine (NPB) are measured using the nanoindentation technique. Although the substrate effect cannot be completely filtered out due to the thin film thickness and the softness of base (PET), with a Young's modulus of around 40-100 GPa, the small molecule layer can still be considered to be applied in the flexible devices. The stress in the indium-tin-oxide (ITO) of the multi layer OLED device when being bent is then calculated using this elastic parameter. A buffer layer inserted between the ITO and PET substrate with an optimized Young's modulus and film thickness is suggested so that, according to theoretical calculations, the stress in the ITO layer can be reduced by up to 60%. Finally the flexible OLED devices were fabricated and their electroluminescence (EL) was measured when the OLED layers were applied with a tensile strain and compressive strain. It is observed that the compressive strain caused less damage than the tensile strain during the bending. It is also observed that a 4 μm thick buffer layer does protect the OLED device in terms of EL brightness while bending with the radius of curvature  $R = 6$  mm. Without the buffer layer, the brightness of the device drops by 40% compares to merely 10% with this buffer layer.

It is finally concluded that with the proper mechanical design of the device structure, the small molecule based OLED devices using the ITO as anode can still be considered as one of the candidates of the flexible display or lighting devices.

# **The Electrical and Mechanical Study of the Flexible Organic Light Emitting Diodes**

Chien-Jung Chiang

A thesis submitted to the Faculty of Science, The University of Durham,  
for the degree of Doctor of Philosophy

Organic Electroactive Materials Group  
Department of Physics  
University of Durham  
January 2011

## **Declaration**

All material contained in this thesis is original and is the result of my own work except where explicit reference is made. Material from work of others has been suitably indicated.

This thesis has not been submitted in whole or in part for the award of a degree at this or any other university.

The copyright of this thesis rests with the author. No quotation from it should be published without their prior consent and information derived from it acknowledged.

## **Acknowledgements**

I want to thank all the people who have supported me during my PhD course and who have made this work possible.

I want to first thank Kodak European Research Centre for the funding of my PhD research. Without them, nothing in this thesis can ever happen.

I want to thank my supervisor, Professor Andy P. Monkman, who gives me the opportunity to study and live in this beautiful city of Durham, and always supplies all I need for my research.

I want to thank Dr. Chris Winscom, my supervisor in Kodak. He is an outstanding researcher and engineer, who always give me practical guidance for my experiment and life.

I want to thank my parents for their full support of my study financially and spiritually.

I want to thank my wife, Mun-Ying, for her accompanies to allow me to focus on my research fully.

I want to thank, last but not least, all my colleagues in the office 129, Rochester Building. For all these years, people come and go, but I remember every one of you! Working and chatting and playing Xbox with you guys are awesome! Thanks for letting me enjoy the final part of my education.

# Table of contents

## Table of Contents

Acknowledgement.....	3
Abstract.....	4
<b>Chapter 1 Introduction.....</b>	<b>13</b>
1.1 Introduction.....	13
1.2 References.....	23
<b>Chapter 2 Theory.....</b>	<b>25</b>
2.1 History of OLED development.....	25
2.2 Some basic elastic properties.....	29
2.3 Pure bending of a rectangular beam.....	32
2.4 The strength properties of solids.....	35
2.5 Creep and stress relaxation.....	40
2.6 Summary.....	43
2.7 References.....	44
<b>Chapter 3 Experimental</b>	
3.1 Thermal Evaporation: Thin-Film Deposition Methods.....	46
3.2 Parameter determination.....	48
3.3 Film Thickness Detection by Interferometry.....	53
3.4 Substrate Preparation.....	55
3.5 Electrical and Optical Measurement.....	56
3.6 Nanoindentation.....	59
3.7 Summary.....	64
3.8 References.....	65
<b>Chapter 4: Comparison of the plastic-based and the glass-based OLED devices in terms of electroluminescence performance</b>	
4.1 Background .....	66
4.2 Experiment.....	67
4.3 Results and discussion.....	69
4.4 Summary.....	77
4.5 References.....	78

**Chapter 5: A nano-indentation study of the reduced elastic modulus of Alq<sub>3</sub> and NPB thin-film used in OLED devices**

**5.1 Background .....80**  
**5.2 Experiment.....82**  
**5.3 Results and discussion.....84**  
**5.4 Summary.....93**  
**5.5 References.....94**

**Chapter 6: Mechanical modeling of flexible OLED devices**

**6.1 Background.....95**  
**6.2 Experiment.....96**  
**6.3 Results and discussion.....103**  
**6.4 Summary.....109**  
**6.5 References.....111**

**Chapter 7: Electroluminescence characterization of FOLED devices under two types of external stresses caused by bending**

**7.1 Background.....112**  
**7.2 Experiment.....114**  
**7.3 Results and discussion (I)... .....119**  
**7.4 Results and discussion (II)... .....127**  
**7.5 Summary.....132**  
**7.6 References.....134**

**Chapter 8**

**Conclusion.....136**

## List of figures and table captions

Fig. 1.1 Some examples of conductive polymers: (a) polyacetylene

(b) polyaniline (c) polypyrrole (d) polythiophene.

Fig. 1.2 Sony XEL-1 11" OLED TV[1.22].

Fig. 1.3. Demonstration of a 4.1" prototype flexible display from Sony[1.22].

Fig. 2.1 The typical energy structure of an OLED device. The open circle is the free hole, and the yellow circle is the free electron. HTL: Hole Transporting Layer; EBL: Electron Blocking Layer; LEL: Light Emitting Layer; HBL: Hole Blocking Layer; ETL: Electron Transporting Layer.

Fig. 2.2 The Jablonski diagram shows all the energy transferring routes of the exciton. S denotes the singlet state, and T denotes the triplet state.

Fig. 2.3 The bar in its original status with a square cross section of side  $a$  and unstrained length  $l_0$  (the solid line). The dash line is the bar suffered from strain in the x-axis (longitudinal) with the strain  $\epsilon_x$  and accompanied by the lateral contraction with the strain  $\epsilon_y$ .

Fig. 2.4 The rectangular element is applied with shear force  $F$ .  $A$  is the area of the upper surface of the object,  $\Delta x$  is the displacement of the upper surface and  $h$  is the original height.

Fig. 2.5 The cross-section of the rectangular beam with the width  $w$  and thickness  $h$ .

Fig. 2.6 The rectangular beam before and after bending with the radius of curvature  $R$ . The segment  $G'H'$  has the same length as segment  $GH$ , and is defined as neutral axis. In this figure, the segments above it is stretched, and below it, compressed.

Fig. 2.7 Distribution of the bending stresses giving null total longitudinal force and a bending moment  $M$ .

Fig. 2.8 The specimen which is subjected to a tensile strength  $F$ .

Fig. 2.9 Typical stress-strain characteristic of a ductile material, which shows an elastic deformation along  $OA$  and plastic yielding at  $Y$  (yielding stress).  $YC$  is the work-hardening process.



- Fig. 3.1 The Kurt J. Lesker Spectros II Deposition System including the operation chamber at the right and the controller panel using the sigma instrument software at the left.
- Fig. 3.2. The illustration of a simple deposition system. The heating source is at the bottom, and the sensor is shown in two different settings[3.2].
- Fig. 3.3. The % Error in Rate/Thickness from using the wrong Z-Factor. This shows at 90% life of the sensor crystal, the error is negligible within a wide range of Z-Factor[3.3]
- Fig. 3.4 The normalized photopic response curve of human eyes. The peak response is 683 lm/W at  $\lambda=555$  nm[3.8].
- Fig. 3.5 The Hysitron TI 950 TriboIndenter
- Fig. 3.6 The schematic representation of a section through an indentation.  $a$  is the radius of the indenter  $h_c$  is the contact depth,  $h_f$  is the final residual depth,  $h_s$  is the displacement of the surface at the perimeter of the contact, and  $h$  is the total displacement.
- Fig. 3.7 (a) to (e) is the sequence of how the tested surface responds to the indenter. (a) to (c) is the loading process, where the deformation from (a) to (b) is mainly plastic. While at (c) the indenter reaches the maximum penetration depth  $h_{max}$ . (c) to (e) is the unloading process, where the displacement from (c) to (d) is mainly elastic.  $h_f$  in (e) is the final depth or the residual depth of the indentation.
- Fig. 3.8 The schematic load-displacement curve of the organic thin-film.
- Fig. 4.1 Device plan. The OLED is sandwiched by the yellow, 10mm x 30mm stripe of ITO at the bottom, and the grey, 10mm x 20mm stripe of aluminium stripe on the top. The light is emitted from the back.
- Fig. 4.2 The J-V characteristic of the OLED devices based on substrates A, B, and C.
- Fig. 4.3 The current efficiency vs. current density of the OLED devices based on substrates A, B, and C.
- Fig. 4.4 The external quantum efficiency of the OLED devices vs. applied voltage based on substrates A, B, and C.
- Fig. 4.5 The normalized EL spectrum (W/nm) of the OLED devices based on substrates A, B, and C.
- Figure 4.6a, 4.6b The simulation results of the CIE<sub>x</sub> (left) and CIE<sub>y</sub>(right) changes with the ITO thickness and the exciton recombination zone of the OLED structure Al(100 nm)/TPBi(200 nm)/ITO(90 nm – 160 nm)/Sub (n = 1.5). The

recombination zone varies from 0 (interface of TPBi and Al) to 1 (interface of TPBi and ITO). The colour of the blocks indicate the value of CIE index. Red is relatively larger than purple in the same diagram.

Fig. 4.7 The luminance of OLED against the ITO thickness for the exciton recombination zone being 0.4, 0.5, and 0.6. The luminance is normalized at the value at ITO thickness of 150 nm of each curve.

Fig. 4.8 The transmittance of the substrate A (black), B (red), and C (green). The dash line indicates the peak, and the region of two dot lines the Full Width at Half Maximum (FWHM) of the EL spectrum.

Fig. 4.9a , 4.9b The AFM image of the ITO surface of the substrate A (4.9a) and substrate B (4.9b).

Fig. 5.1a, 5.1b Structure of Tris-(8-hydroxyquinoline) aluminum (Alq3) (5.1a) and N,N'-Bis(naphthalen-1-yl)-N,N'-bis(phenyl)benzidine (NPB) (5.1b).

Fig. 5.2 Load-displacement curve for the 200 nm thick NPB coated on a PET film obtained

under open loop control at maximum indenter displacement ( $h_{max}$ )=475 nm.

Fig. 5.3 Reduced elastic modulus against contact depth for the samples Ia, Ib and Ic.

Fig. 5.4 Reduced elastic modulus against contact depth for the samples IIa and IIb.

Fig. 5.5 Extrapolation to zero depth of the curve in figure 5.4 when considering the contact depth from 5 nm to 10 nm.

Fig. 5.6 Reduced elastic modulus against relative indentation depth (RID) for the samples Ia, Ib and Ic.

Fig. 5.7 Reduced elastic modulus against relative indentation depth (RID) for the samples IIa and IIb.

Fig. 5.8 Elastic modulus against relative indentation depth (RID) for the polycrystalline copper coated on softer (polyimide) and stiffer (sapphire) bases.

Fig. 6.1 One segment of a single-material beam before (a) and after (b) bending.

Layer ab is the Neutral Layer; Layer cd, c'd' is the same layer before and after bending with radius R.

Fig. 6.2 Cross-section (a) and effective cross-section according to the top layer (b) of a two-material composite beam. The thickness of each layers are  $h_i$  and  $h_s$ .

Fig. 6.3 The stress in ITO against the thickness of glass buffer layer with the fixed “glass/PET” composite substrate thickness of 175  $\mu\text{m}$ . The bending radius is 10 mm.

Fig. 6.4 The stress in ITO against the thickness of buffer layer with different buffer layer Young’s modulus in the five-layers structure:

PET(100 $\mu\text{m}$ )/Buffer(0-100 $\mu\text{m}$ )/ITO(100nm)/OLED(100nm)/Aluminium(100nm).

The bending radius is 15 mm.

Fig. 6.5 The stress in ITO against the device bending radius with different buffer layer Young’s modulus in the five-layers structure:

PET(100 $\mu\text{m}$ )/Buffer(20 $\mu\text{m}$ )/ITO(100nm)/OLED(100nm)/Aluminium(100nm).

Fig. 6.6 The stress in ITO against the device bending radius with different buffer layer Young’s modulus in the five-layers structure:

PET(100 $\mu\text{m}$ )/Buffer(100 $\mu\text{m}$ )/ITO(100nm)/OLED(100nm)/Aluminium(100nm).

Fig. 7.1 The FOLED device was mounted and bent on the sample holder to be measured by the Konica-Minolta LS-110 Luminance meter fixed above the sample holder as shown in figure 7.1. The curved line is the FOLED device. It is fixed at the left end of the long side (position D). The dash line is the active OLED area which emits light. The right end is to be fixed at the position A, B, and C for different radius of curvature.  $\overline{DC} = 25$  mm,  $\overline{DB} = 35$  mm,  $\overline{DA} = 45$  mm.

Fig. 7.2 The FOLED device plan. The darker area is the ITO layer. The lighter oblong shape covered on it is the aluminium layer. The dimensions are in unit of mm. The OLED is thermal evaporated everywhere on the 40 mm x 30 mm PET substrate and between these two electrodes. The OLED active area is 10 mm x 5 mm.

Fig. 7.3 The cylindrical rods used to estimate the bending radius of curvature of the device.

Fig. 7.4 The traced curves from the 2.5 x images of the FOLED device bent with position A, B, and C.

Fig. 7.5 the 2<sup>nd</sup> derivative of the curves in figure 7.4 around the active OLED area (x=5)

- Fig. 7.6 The lifetime measurement of the non-encapsulated FOLED device under constant current supply at  $9.4 \text{ mA/cm}^2$ .
- Fig. 7.7 The brightness of the FOLED device against the testing runs. In the Expt. 1 (filled square), the OLED device was given a stretched stress while in the Expt. 2 (open circle), a compressive stress.  $R_x$  denotes the radius of curvature:  $R_1 =$  position A,  $R_2 = B$ , and  $R_3 = C$ .
- Fig. 7.8a, 7.8b Current efficiency and JV characteristic of the FOLED device Expt.3 against the testing runs. The device was given a tensile stress with  $R_c =$  position C in run 2 and 4 (open symbols). The device was unbent in run 1, 3, and 5 (filled symbols).
- Fig. 7.9a, 7.9b Current efficiency and JV characteristic of the FOLED device Expt.4 against the testing runs. The device was given a compressive stress with  $R_c =$  position C in run 2 and 4 (open symbols). The device was unbent in run 1, 3, and 5 (filled symbols).
- Fig. 7.10 The AFM images of the aluminum surface of the FOLED device in Expt.1 after the bending tests. The device was given a tensile stress.
- Fig. 7.11 The AFM images of the aluminum surface of the FOLED device in Expt.2 after the bending tests. The device was given a compressive stress.
- Fig. 7.12. The reduced elastic modulus of the buffer material vs. the contact depth.
- Fig. 7.13. The stress in ITO varies depending on the thickness of the buffer layer.
- Fig. 7.14 The normalized brightness of the FOLED device against the testing runs when OLED layers were given a stretched strain. The Expt. 1 (filled square) is the reference device and the Expt. 5 (open circle) and 6 (filled triangle) shows the devices with  $4\mu\text{m}$  thick of buffer layer.
- Fig. 7.15 The normalized brightness of the FOLED device against the testing runs when OLED layers were given a compressive strain. The Expt. 2 (open circle) is the reference device and the Expt. 7 (filled square) shows the devices with  $4\mu\text{m}$  thick of buffer layer.
- Fig.7.16. Strain of the OLED thin-films (including ITO and Al) vs.  $R_c$  for the device structure: aluminium (100 nm)/ OLED (100 nm)/ ITO (100 nm)/ BL( $4\mu\text{m}$ )/ PET (0.127 mm).
- Fig.7.17. Microscopy image of the aluminum surface of the device Expt.1 (left) and Expt.5 (right). Cracks caused by bending can be observed clearly on device Expt.1, while on the device Expt.5, there were only some scratches observed.

Table 1.1 Comparison of oxygen permeation rate (OTR) and water vapor transmission rate (WVTR) values of Polyethylene terephthalate (PET) containing inorganic thin film coatings normalized to 1 mil thickness. **RH**: relative humidity. **STP**: Standard Temperature & Pressure (273 K, 1 atm)

Table 1.2 Evaluation of the main players in the new generation display competition.  
VG: very good; G: good; A: acceptable; P: poor

Table 4.1 Substrate B is the ITO(35Ω/sq)/PET, substrate C is the ITO(60Ω/sq)/PET, and the substrate A is the ITO(15Ω/sq)/glass.

Table 5.1 Samples investigated.

Table 5.2 Reduced elastic moduli of samples determined by different methods.

The error is about 11% for the coatings on stiff substrates (IIa and IIb) and about 25% for the coating on soft substrates (Ia, Ib and Ic).

Table 5.3 Young's modulus of selected materials

Table 6.1 The value of Young's modulus and reduced elastic modulus used in the simulation.

Table 7.1 The experimental details about the bending curvature at different runs.

Table 7.1 The experimental details about the bending curvature at different runs.

# ***Chapter 1***

## ***Introduction***

### ***1.1 Introduction***

The organic light emitting diode (OLEDs), first proposed by C. W. Tang and S. A. Vanslyke in 1987[1] with a bi-layer thin-film structure, is a “self-emitting” technology with wide viewing angle (over 170 degrees), fast reaction time (less than 1  $\mu$ s), high efficiency (100 lm/W), low operation voltage ( $\sim$ 3V). It could be produced as thin as 2mm for a device, with large area, the ability to be flexible in shape, and free from mercury. Therefore it has been regarded as one of the frontrunners of the candidates in flat panel display and solid state lighting applications for tomorrow.

In terms of the flat panel display applications, the first decade of the 21<sup>st</sup> century has seen the growth of demand for hand-held information devices, such as the smart phone, mp4 player, and the tablet PC, to interact with the web and Cloud-computing. All these devices require a high quality, small display (less than 10 inches) which could be made as thin as possible, and with high power efficiency, high contrast ratio, fast reaction time, and wide viewing angle. The most highly developed technology to do the job over the past 10 years was the liquid crystal display (LCD). Although LCD has some undesirable characteristics such as filters that reduce the light generated by

the display back light by more than 50% (using polarization and colour filters), the power efficiency of these devices has been improved by using light emitting diodes (LED) as the back light source. Another notorious problem, the narrow viewing angle, has been improved by various technologies such as in-plane switching[2] (IPS) and multi-domain vertical alignment[3] (MVA). Thus the advantage of wide viewing angle and low power consumption OLED once held a decade ago against LCD has been gradually eroded, and more and more reports of comparison of the super-LCD and OLED displays on similar products can be found in the technology reviews[4]. The league table of OLED along with other candidates of display is listed in table 1.2.

As for solid state lighting, the rising star for the past few years is the inorganic LED. With its high power efficiency (~100 lm/W), and matured production process, it is widely used and promoted by the governments and artists, notably in the open ceremony of 2008 Olympics and the World Expo 2010. After further development, OLED lighting is expected to achieve the same level in terms of efficiency. In addition, OLED has the advantage that whilst LED is a point light source, OLED is a surface source which puts it in a different category in terms of application, and OLED will be even more attractive if it is made conformable or even flexible.

Although there are high expectations of OLED devices in terms of potential energy cutting and wide viewing angle, what really makes OLED superior to its competitors is the possibility of being flexible. This will bring in at least five more advantages:

1. Light weight. It can save further energy from being easier to transport.
2. Highly robust. This is especially important for the more and more popular portable displays.

3. Curved displays. The one-off bending panel can be applied widely in automobile industry and architectural lighting design.
4. Roll-up displays. A display which can be bent many times allows new genre of applications to be created.
5. Roll-to-roll manufacturing process. This is very important for the cheaper mass production of OLED devices.

With so many good reasons to have OLED go flexible, there are still challenges to be overcome[5]:

### **1. Flexible Substrate.**

Polymers, metals and thin glasses were considered as the substrates of Flexible OLEDs (FOLEDs)[6]. The polymeric substrate is light-weight, transparent, but permeable to water and oxygen and thus it requires a barrier layer. The other significant challenge is the processing temperature required by subsequent device layers is generally high, especially when FOLEDs in the foreseeable future are likely to be a hybrid of inorganic and organic layers and components. However, the processing temperature required for many inorganic layers has dropped[7] and the thermal stability of polymer substrates has been improved recently[8]. A metal substrate, for example stainless steel, is a good barrier, a good thermal conductor and is robust. But it is reflective, it is heavier than polymers and it is conductive, thus it needs to be coated with an insulator to avoid forming a short circuit. Thin glass, on the other hand, is transparent, thermally stable and almost impermeable to water and oxygen. The lack of flexibility used to be an issue, but a method of processing a 30  $\mu\text{m}$  glass film coated with a polymeric composite layer has been developed to



enable one to capitalize on the positive attributes of glass as well as to enable it to be more flexible and suitable for process handling[9].

## **2. Barrier Layers and Encapsulation.**

When polymeric substrates are employed in FOLEDs applications, a barrier is required to protect the enclosed functional materials from oxygen and water permeation which the OLEDs are sensitive to. The latter, in particular, has proved to be an important issue which leads to the creation of non-emissive black spots and pixel shrinkage [10, 11]. Display manufacturers in general require the water vapor transmission rate (WVTR) of  $<10^{-5}$  g/m<sup>2</sup> per day at 25°C and 100% relative humidity (RH). There are currently two ways to encapsulate a flexible device: lamination and multi-film deposition. There are more reports concerning the latter as the former is still not a mature technology. To cover the OLED with one or more inorganic protection films is a straight forward solution, however the inorganic thin film is too brittle and might crack when being bent, and therefore lose its function as a protection layer against the water and oxygen. Therefore a hybrid of organic and inorganic multi-layers seems to be a more realistic choice. Table 1.1[12] shows that an inorganic/organic hybrid multilayer can form a barrier layer which could potentially satisfy the demanding requirements of the OLED materials, but there is still much scope to improve. Recently the thin film encapsulation (TFE) process proposed by H. Kim *et al.* used the inorganic-organic multilayer system (a number of repeated structure consisting of a sputtered Al<sub>2</sub>O<sub>3</sub> layer sandwiched by polyacrylate layers) as the covering layer and successfully extended the OLED lifetime by a factor of 4[13].

Nevertheless, preventing the permeation of oxygen and water vapor remains one of the major tasks for the development of FOLEDs in the next few years.

<b>Barrier Layers</b>	<b>OTR (cm<sup>3</sup>(STP)/m<sup>2</sup>) per day per atm)</b>	<b>WVTR (g/m<sup>2</sup>) per day at 90- 100% RH)</b>	<b>Deposition method</b>
PET/SiO <sub>x</sub>	2.0	1.1	Evaporation
PET/AlO <sub>x</sub>	1.5	5.0	Evaporation
PET/AlO <sub>x</sub> N <sub>y</sub>	2.8	4.3	Sputtering
PET/ITO	1.56	0.2	Sputtering
PET/Al	0.31-1.55	0.31-1.55	Evaporation
PET/7 mm Al foil	0.001	N/A	Lamination
PET	79	10.7	N/A

Table 1.1 Comparison of oxygen permeation rate (OTR) and water vapor transmission rate (WVTR) values of Polyethylene terephthalate (PET) containing inorganic thin film coatings normalized to 1 mil thickness. **RH**: relative humidity. **STP**: Standard Temperature & Pressure (273 K, 1 atm)

### **3. Inorganic Conducting Layers and Mechanical Properties.**

Inorganic conducting materials such as Indium tin oxide (ITO) are widely used in display technologies. However, the processing temperature required for depositing these layers on glass to obtain low sheet resistance and high optical transmittance is incompatible with polymeric substrates. Therefore lower-temperature deposition processes need to be developed. When under tensile and compressive strain, cracks and buckles on the ITO surface were observed[14]. A relation between the presence of ITO surface failures and the onset of sheet resistance was also suggested [15].

### **4. Organic Conducting Layers and Mechanical Properties.**

The majority of Polymers used for applications in daily life are generally insulators, but conjugated polymers are exceptions. The charge carriers can hop across the polymer chains between delocalized  $\pi$  bond, and they are therefore electrically conductive and were considered for flexible OLED applications[16]. Some examples of such polymers are shown in figure 1.1. Although the sheet resistance and optical properties still cannot match ITO, they do show satisfying mechanical properties and require a lower processing temperature. A third option to form a transparent and ductile electrode was also proposed by dispersing carbon nanotubes in combination with wet coating processes and printing technologies[17, 18].

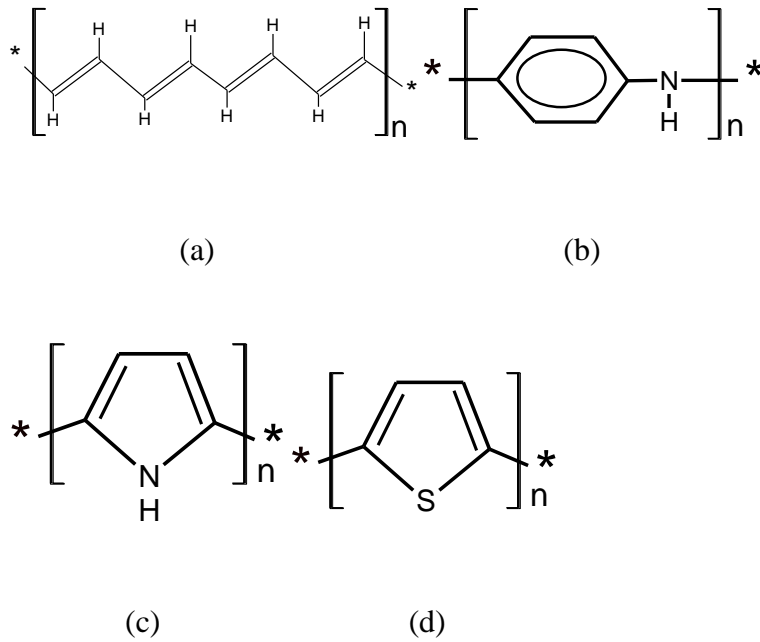


Fig. 1.1 Some examples of conductive polymers: (a) polyacetylene

(b) polyaniline (c) polypyrrole (d) polythiophene.

## 5. Optical Coatings.

Optical coatings such as polarizers, color-filters, antireflection films, and alignment layers, have been widely used on the glass-based display technologies. They can still play an important role in FOLED applications.

## 6. Thin Film Transistors (TFTs).

FOLED applications require an active matrix backplane to enhance the performance, so a lot of work has been done in developing various processes to print and pattern organic electronics on polymeric substrates[19]. There are also efforts to developing a process to create inorganic TFTs on metal foil based substrates[20], as well as understand the failure mechanism of TFTs on flexible substrates[21].

This thesis is focused on the electrical and mechanical characterization of FOLEDs, which were fabricated by depositing the organic thin films onto a soft substrate, such as a polyethylene terephthalate (PET) film. The key problem to be solved here is to choose the proper material for the electrode (especially the anode). For a conventional bottom-emitting glass-based OLED device, indium tin oxide (ITO) is sputtered on the glass substrate as a highly transparent, highly conductive, and work function matched anode. But the use of ITO on PET substrate is controversial as has been mentioned already. The most important reason is the large difference the Coefficient of Thermal Expansion (CTE) between ITO ( $8.5 \times 10^{-6} / ^\circ\text{C}$ ) and PET ( $1.2 \times 10^{-4} / ^\circ\text{C}$ ). So a new technology for sputtering ITO at lower temperature is needed. Although there are already some commercialized ITO coated plastic substrates available, so far the surface quality of this newly developed technology is not as good as the ITO coated glass. Irrespective of the rougher ITO surface, if the OLED structure used on a glass substrate were transferred directly to a PET substrate, would it be significantly different in terms of the electroluminescent (EL) performance? This is explored in Chapter 4. When a bendable ITO based FOLED device is operated, heat is also generated. An approximate measurement suggested that the operating temperature is no higher than  $50\text{ }^\circ\text{C}$ . Although as mentioned above, the CTE difference between ITO and PET could induce thermal stress in the films, at  $50\text{ }^\circ\text{C}$  the stress caused by the CTE difference is similar to the stress caused by external bending when the radius of curvature is about 20 mm. Therefore if the radius of curvature of the bending is around 10 mm, the bending stress is higher and the thermal stress is negligible. This was confirmed as no cracks were observed in the devices after 40 heating cycles to  $50\text{ }^\circ\text{C}$  were applied to the ITO coated PET substrate, so the mechanical study of the FOLEDs undertaken focused on the bending stress, beginning from the measurement

of the reduced elastic modulus of small molecules used in OLEDs, which is in chapter 5. The theoretical stress in the multi-layer FOLED device is deducted and two different examples for practical use are simulated in the Chapter 6, and finally the comparison of the EL performance of the FOLED devices under different bending conditions is reported in the Chapter 7. The Conclusion is in chapter 8.

	<b>Cathode Ray Tube (CRT)</b>	<b>Liquid Crystal Display (LCD)</b>	<b>Organic Light- Emitting Diode (OLED)</b>	<b>Light Emitting Diode (LED)</b>	<b>Plasma Display Panel (PDP)</b>
<b>Brightness</b>	<b>G</b>	<b>G</b>	<b>VG</b>	<b>A</b>	<b>A</b>
<b>Efficiency</b>	<b>G</b>	<b>G</b>	<b>VG</b>	<b>A</b>	<b>A</b>
<b>Life</b>	<b>VG</b>	<b>G</b>	<b>G</b>	<b>VG</b>	<b>A</b>
<b>Weight</b>	<b>P</b>	<b>VG</b>	<b>VG</b>	<b>A</b>	<b>G</b>
<b>Thickness</b>	<b>P</b>	<b>VG</b>	<b>VG</b>	<b>A</b>	<b>G</b>
<b>Reacting Time</b>	<b>VG</b>	<b>A</b>	<b>VG</b>	<b>VG</b>	<b>G</b>
<b>View Angle</b>	<b>VG</b>	<b>G</b>	<b>VG</b>	<b>A</b>	<b>A</b>
<b>Cost</b>	<b>VG</b>	<b>G</b>	<b>A</b>	<b>G</b>	<b>A</b>

Table 1.2 Evaluation of the main players in the new generation display competition.

VG: very good; G: good; A: acceptable; P: poor



Fig. 1.2 Sony XEL-1 11" OLED TV[22].



Fig. 1.3. Demonstration of a 4.1" prototype flexible display from Sony[22].

## 1.2 References:

- [1] C. W. T. a. S. A. Vanslyke, "Organic electroluminescent diodes," *Applied Physics Letters*, vol. 51, pp. 913-915, 1987.
- [2] Y. C. Yang and D. K. Yang, "Wider Viewing Angle in In-Plane Switching Mode Liquid Crystal Displays by Self-Compensated Phase Retardation Films," in *2009 Sid International Symposium Digest of Technical Papers, Vol XI, Books I - Iii*, J. Morreale, Ed. Campbell: Soc Information Display, 2009, pp. 1563-1566.
- [3] Y. C. Lu, C. S. Cheng, C. J. Hu, C. M. Chang, F. Y. Gan, and Sid, "New multi-domain vertical alignment LCD with high contrast ratio," in *2007 Sid International Symposium, Digest of Technical Papers, Vol Xxxviii, Books I and Ii*. vol. 38 Playa Del Rey: Soc Information Display, 2007, pp. 725-727.
- [4] D. R. M. Soneira, "Smartphone "Super" LCD-OLED Display Technology Shoot-Out," 2010.
- [5] G. P. Crawford, "Flexible Flat Panel Display Technology," in *Flexible Flat Panel Displays*, G. P. Crawford, Ed.: John Wiley & Sons, Ltd, 2005, pp. 1-9.
- [6] W. A. MacDonald, "Engineered films for display technologies," *Journal of Materials Chemistry*, vol. 14, pp. 4-10, 2004.
- [7] K. Zhang, F. R. Zhu, C. H. A. Huan, and A. T. S. Wee, "Indium tin oxide films prepared by radio frequency magnetron sputtering method at a low processing temperature," *Thin Solid Films*, vol. 376, pp. 255-263, 2000.
- [8] M. A. Simone Angiolini, Carlo Barlocco, Roberto Bracco, Joseph J. Bacskey, John-Henry Lipian, Phillip S. Neal, Larry F. Rhodes, Robert A. Shick, Xiao-Mei Zhao, Gary Freeman, "high performance plastic substrates for flexible flat panel display," *Digest of Technical Papers*, pp. 1-4, 2000.
- [9] S. D. A. Plichta, A. Weber and A. Habeck, "Thin glass-polymer systems as substrates for flexible displays," in *SID Proceedings*, 2002.
- [10] P. E. Burrows, V. Bulovic, S. R. Forrest, L. S. Sapochak, D. M. McCarty, and M. E. Thompson, "Reliability and degradation of organic light emitting devices," *Applied Physics Letters*, vol. 65, pp. 2922-2924, Dec 1994.
- [11] D. Kolosov, D. S. English, V. Bulovic, P. F. Barbara, S. R. Forrest, and M. E. Thompson, "Direct observation of structural changes in organic light emitting devices during degradation," *Journal of Applied Physics*, vol. 90, pp. 3242-3247, Oct 2001.
- [12] P. E. B. Gordon L. Graff, Rick E. Williford and Robert F. Praino, "Barrier Layer Technology for Flexible Displays," in *Flexible Flat Panel Displays*, G. P. Crawford, Ed.: John Wiley & Sons, Ltd, 2005, pp. 57-77.
- [13] A. B. Chwang, M. A. Rothman, S. Y. Mao, R. H. Hewitt, M. S. Weaver, J. A. Silvernail, K. Rajan, M. Hack, J. J. Brown, X. Chu, L. Moro, T. Krajewski, and N. Rutherford, "Thin film encapsulated flexible organic electroluminescent displays," *Applied Physics Letters*, vol. 83, pp. 413-415, Jul 2003.
- [14] S. K. Park, J. I. Han, D. G. Moon, and W. K. Kim, "Mechanical stability of externally deformed indium-tin-oxide films on polymer substrates," *Japanese*



*Journal of Applied Physics Part I-Regular Papers Short Notes & Review Papers*, vol. 42, pp. 623-629, Feb 2003.

- [15] Y. Leterrier, L. Medico, F. Demarco, J. A. E. Manson, U. Betz, M. F. Escola, M. K. Olsson, and F. Atamny, "Mechanical integrity of transparent conductive oxide films for flexible polymer-based displays," *Thin Solid Films*, vol. 460, pp. 156-166, Jul 2004.
- [16] J. T. W. J. Feast, K. L. Pouwer, L. Groenendaal and E. W. Meijer, "Synthesis, processing and material properties of conjugated polymers," *Polymer*, vol. 37, pp. 5017-5047, 1996.
- [17] P. G. D. Arthur, P. Wallis, and M. Trottier, "Flexible Transparent Circuits from Carbon Nanotubes," *SID Symposium Digest of Technical Papers*, vol. 35, pp. 582-585 May 2004 2004.
- [18] P. G. C. M. Trottier, P. Wallis, and J. Luo, "Properties and characterization of carbon-nanotube-based transparent conductive coating," *Journal of the SID*, vol. 13/9, pp. 759-763, 2005.
- [19] B. Crone, A. Dodabalapur, Y. Y. Lin, R. W. Filas, Z. Bao, A. LaDuca, R. Sarpeshkar, H. E. Katz, and W. Li, "Large-scale complementary integrated circuits based on organic transistors," *Nature*, vol. 403, pp. 521-523, 2000.
- [20] J. H. Cheon, J. H. Choi, J. H. Hur, J. Jang, H. S. Shin, J. K. Jeong, Y. G. Mo, and H. K. Chung, "Active-matrix OLED on bendable metal foil," *Ieee Transactions on Electron Devices*, vol. 53, pp. 1273-1276, 2006.
- [21] H. Gleskova, I. C. Cheng, S. Wagner, J. C. Sturm, and Z. G. Suo, "Mechanics of thin-film transistors and solar cells on flexible substrates," *Solar Energy*, vol. 80, pp. 687-693, 2006.
- [22] "Organic light-emitting diode," [http://en.wikipedia.org/wiki/Organic\\_light-emitting\\_diode](http://en.wikipedia.org/wiki/Organic_light-emitting_diode), Wikipedia, 27/01/11

## ***Chapter 2***

### ***Theory***

#### ***2.1 History of OLED development***

Since the first organic EL related research reported by Professor Pope about the electroluminescence (EL) of anthracene crystals under more than 700 volts driving voltage[1] in 1963, the history of organic EL has come to about half a century.

Initially because of the high drive voltage and poor efficiency, no further notice was taken of these materials until 1987. In this year Dr. Ching W. Tang and Dr. Steve Vanslyke of Kodak Ltd. developed the multi-layer small molecule based OLED device using thermal deposition [2]. With its low operating voltage (6 V) and high efficiency (1 cd/A), this bi-layer design attracted the world's attention almost immediately. The key of the success was to confine the excitons (the electron-hole pairs) at the interface of a Hole Transporting Layer (HTL) and an Electron Transporting Layer (ETL) to emit light.

In the mean time, on the other side of the Atlantic Ocean, Professor Richard Friend and J. Burroughs of Cambridge University successfully fabricated Poly-LEDs based on conjugated polymers deposited by the spin-coating method[3] in 1990. This very simple process can be operated in air instead of in high level of vacuum, which is required for the thermal deposition process. This discovery again showed the world the huge potential of the self-emitting organic devices.

The OLED device usually contains several functional layers and one or more major emitter layers, which are finally sandwiched by two electrodes as shown in the Fig.

2.1. When an electrical field is applied, charge carriers are injected into the functional layers by overcoming the potential barrier between the electrode work function and the energy state of the highest occupied molecule orbital (HOMO) or the lowest unoccupied molecule orbital (LUMO). The injected electrons and holes are driven by the electric field, and hop from one molecule to another. Some of them are trapped by the empty energy state of defects, some travel all the way to the other electrode and generate heat. The rest meet each other and form the electron-hole pairs (excitons). These excitons then decay, with a given fraction producing light.

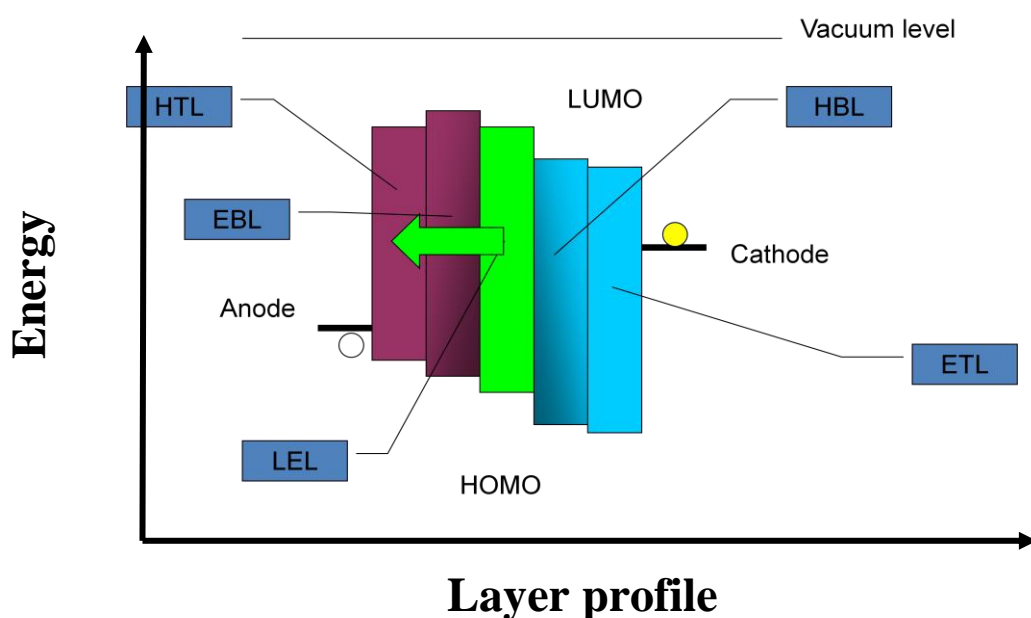


Fig. 2.1 The typical energy structure of an OLED device. The open circle is the free hole, and the yellow circle is the free electron. HTL: Hole Transporting Layer; EBL: Electron Blocking Layer; LEL: Light Emitting Layer; HBL: Hole Blocking Layer; ETL: Electron Transporting Layer.

Generally speaking, only 25% of these excitons formed by charge recombination will be singlet states as determined by quantum mechanics, and thus recombine to emit

light. The other 75% of the excitons are formed in the triplet state. They have longer lifetime (up to milliseconds) than their singlet counterpart because of the forbidden  $T_1$  (triplet state)  $\rightarrow S_0$  (ground state) transition preventing radiative decay. This allows them to migrate in the bulk for up to several nanometers [4]. They may either transfer to the lower energy states or recombine to pass the energy to the surrounding lattice (heat) or collide with each other to form another singlet exciton (triplet-triplet annihilation)[5, 6]. The energy transfer routes for the excitons are shown in Fig. 2.2. Therefore, how to make the most of the injected electrons and holes to form the excitons, and how most of the excitons can then emit light at the wavelength we want, has become the Holy Grail for the OLED researchers.

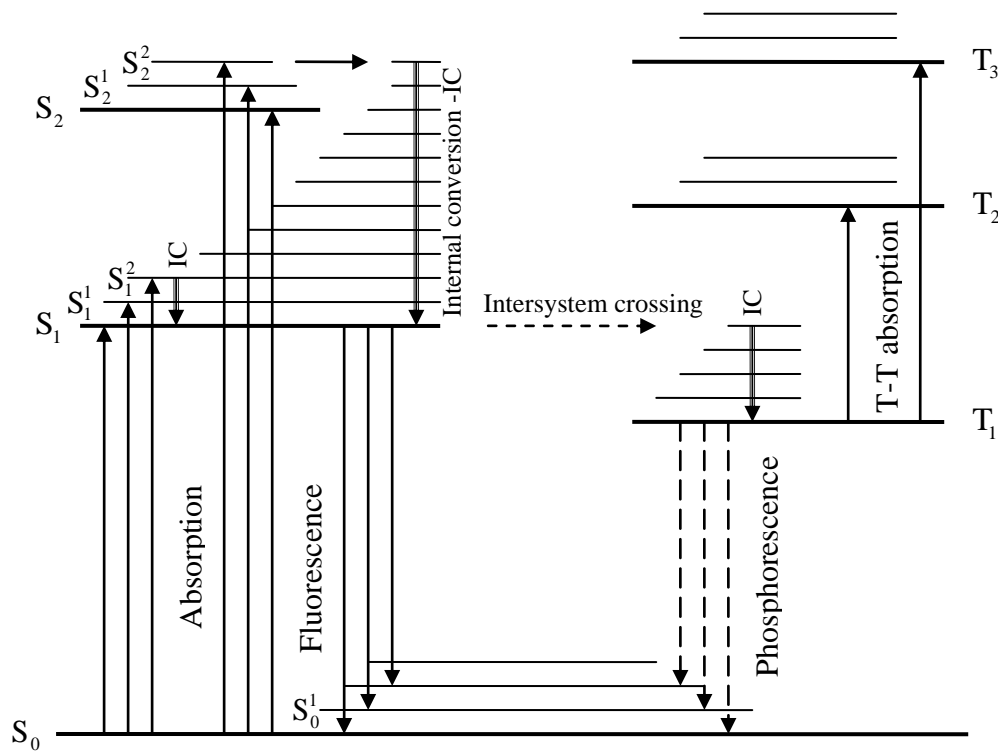


Fig. 2.2 The Jablonski diagram shows all the energy transferring routes of the exciton.

S denotes the singlet state, and T denotes the triplet state.

In the last decade, the performance of OLED devices has improved significantly by employing many creative ways. Some of the most important examples are highlighted as follows:

1. Better matching between the energy levels of each functional layer, especially between the electrode and its adjacent layer, by introducing composite electrode or through the doping[7-9].
2. Inserting the hole and electron blocking layers to achieve better charge carrier balance[10].
3. Recycling the 75% of the triplet excitons by doping the emissive layer with a phosphorescent material and optimizing density to emit light through a dopant species[11].
4. Optimizing the optical structure of the device by depositing high refractive index material outside of the transparent electrode to extract the most of the light produced inside the device[12].

In the meantime, the hermetic sealing process has also improved to extend the device lifetime to a reasonable level. So the issues for the future really would be the synthesis of new materials to provide a wider range of luminescence wavelength, the improvement of device production yield, the design of electrical driving circuits, and finally creating a way that would lead to realistic flexible OLEDs. This last point is the concern of this thesis work. In the following chapters, the basic properties of flexible substrates and how these effect OLEDs fabricated on them are discussed.

## 2.2 Some basic elastic properties

In order to understand the stress in the FOLED devices, some basic knowledge of the elastic properties of solids is required. When a solid rod of uniform cross-sectional area  $A$  has a tensile force  $F$  applied to it, the tensile stress in the rod  $\sigma$  is defined as

$$\sigma = \frac{F}{A} \quad (2.1)$$

If, during the process, the length of the rod increases from  $l$  to  $l + \Delta l$ , then the linear strain induced,  $\varepsilon$ , is defined by

$$\varepsilon = \frac{\Delta l}{l} \quad (2.2)$$

If within the elastic range, Hooke showed that the stress is proportional to the strain:

$$\sigma = E\varepsilon \quad (2.3)$$

where  $E$  is the Young's modulus.

As the rod stretches along the direction of the applied force  $F$ , it must contract in the direction at right angles to the direction of the tension. The fractional contraction  $\varepsilon_t$  in the transverse direction is found to be proportional to  $\varepsilon$ . The ratio is defined as the Poisson's ratio  $\nu$ :

$$\nu = \frac{\varepsilon_t}{\varepsilon} \quad (2.4),$$

Most materials have a Poisson's ratio value between 0.0 and 0.5[13]. For a stable, isotropic, linear elastic material such as rubber, the Poisson's ratio is  $\sim 0.5$ [14].

Stainless steel is  $\sim 0.3$ [14]. A perfectly incompressible material deformed elastically at small strains would have a Poisson's ratio of exactly 0.5. The reason is as follows:

If a bar of a material M is stretched longitudinally with the strain  $\epsilon_x$  as shown in figure 2.3, it will accompany by the lateral contraction  $\epsilon_y$ . By equation (2.4)

$\epsilon_y = \nu\epsilon_x$ , and  $\nu$  is the Poisson's ratio of M.

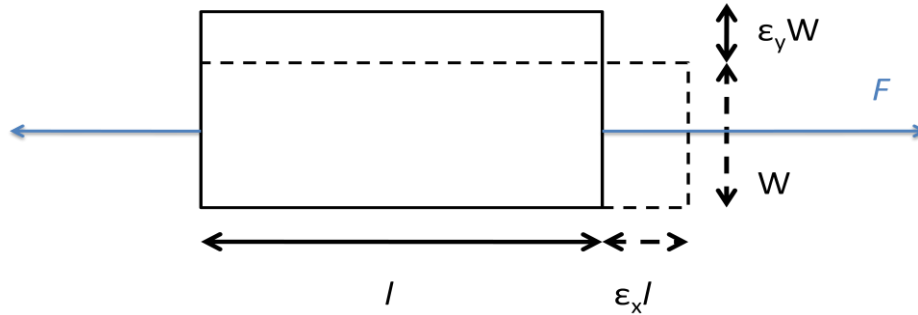


Fig. 2.3 The bar in its original status with a square cross section of side  $a$  and unstrained length  $l_0$  (the solid line). The dash line is the bar suffered from strain in the  $x$ -axis (longitudinal) with the strain  $\epsilon_x$  and accompanied by the lateral contraction with the strain  $\epsilon_y$ .

The volume of the bar before and after stretching is:

$$V_0 = w^2 l_0$$

$$V = (w - \epsilon_y w)^2 (L_0 + \epsilon_x l_0) = V_0 (1 - \epsilon_y)^2 (1 + \epsilon_x)$$

If  $\epsilon_x$  and  $\epsilon_y$  are  $\ll 1$ ,

$$(1 - \epsilon_y)^2 (1 + \epsilon_x) \sim (1 - 2\epsilon_y)(1 + \epsilon_x) \sim 1 + \epsilon_x - 2\epsilon_y$$

Therefore,

$V = V_0 (1 + \epsilon_x - 2\epsilon_y)$ , and the volumetric strain would be

$$\frac{V - V_0}{V_0} = \epsilon_x - 2\epsilon_y = \epsilon_x (1 - 2\nu) \quad (2.5)$$

So, from equation (2.5), if there is no change of volume before and after stretching,  $v=0.5$ .

A solid may also be deformed in shear. Figure 2.4 shows a rectangular element with a shear force  $F$  applied to the upper surface. The shear stress ( $\tau$ ) is then defined as

$\tau = \frac{F}{A}$ , where  $A$  is the area of the upper surface.

The shear strain ( $\epsilon_s$ ) is defined as  $\epsilon_s = \frac{\Delta x}{h} = \tan \theta$ , which is found to be proportional to shear stress. Therefore the shear modulus,  $G$ , is defined as

$$G = \frac{\tau}{\epsilon_s} \quad (2.6)$$

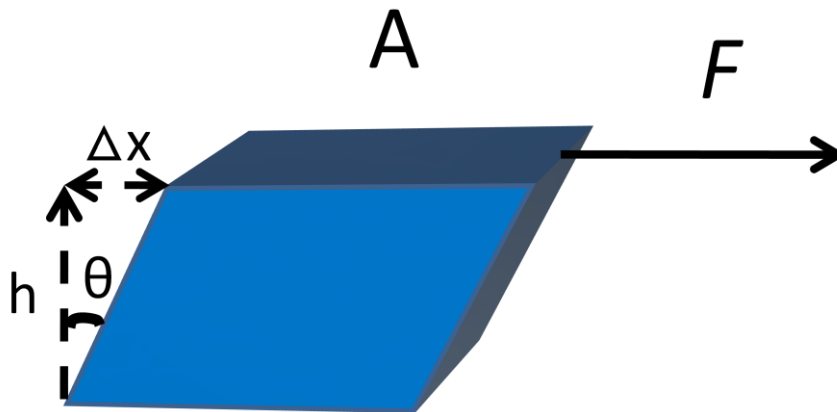


Fig. 2.4 The rectangular element is applied with shear force  $F$ .  $A$  is the area of the upper surface of the object,  $\Delta x$  is the displacement of the upper surface and  $h$  is the original height.



### 2.3 Pure bending of a rectangular beam

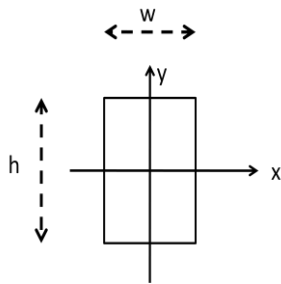


Fig. 2.5 The cross-section of the rectangular beam with the width  $w$  and thickness  $h$ .

Consider a straight uniform beam with a rectangular cross-section of width  $w$  and thickness  $h$  as shown in figure 2.5. The beam is now applied with end couples as shown in figure 2.6 with the radius of curvature  $R$ . Compare the block  $A'B'D'C'$  with block  $ABDC$ , it is found that segment  $A'C'$  is stretched, and segment  $B'D'$  is compressed. So it is reasonable to assume that there exists a segment  $GH$ , which has the same length as  $G'H'$ , i.e. unstrained after bending, and is defined as the neutral axis.

Now consider the segment  $EF$ , which is on the tension side of the beam after bending ( $E'F'$ ), and at the distance  $y$  from the neutral axis. To find out how much  $EF$  has stretched after bending, the length of  $E'F'$  is

$$\overline{E'F'} = (R + y)\theta$$

The length of  $EF$  is equal to the length of  $GH$ . Since  $GH$  is the neutral axis, the length of  $G'H'$  is equal to the length of  $GH$ . Therefore

$$\overline{EF} = \overline{GH} = \overline{G'H'} = R\theta.$$

So the stretched length is

$$\overline{E'F'} - \overline{EF} = y\theta$$

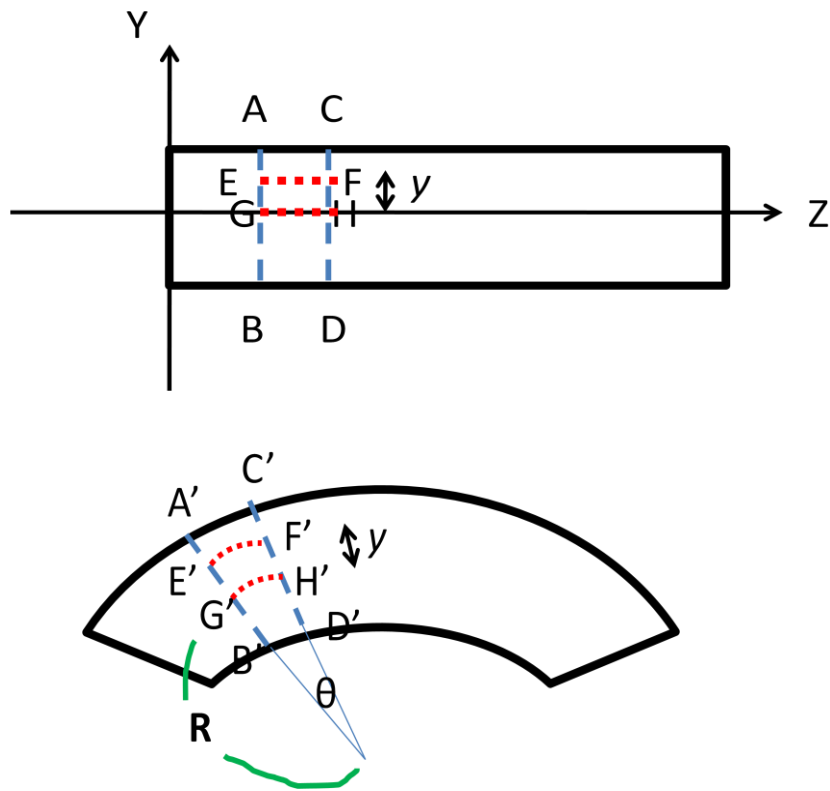


Fig. 2.6 The rectangular beam before and after bending with the radius of curvature R. The segment G'H' has the same length as segment GH, and is defined as neutral axis. In this figure, the segments above it is stretched, and below it, compressed.

From equation (2.2), the strain  $\epsilon$  can be found

$$\epsilon = \frac{\overline{E'F'} - \overline{EF}}{\overline{EF}} = \frac{y\theta}{R\theta} = \frac{y}{R} \quad (2.7)$$

If the beam is within the linear elastic limit, from equation (2.3), the stress that the segment E'F' experienced,  $\sigma$ , is

$$\sigma = E \frac{y}{R}, \quad (2.8)$$

where E is the Young's modulus of the rectangular beam.

So the stress in each segment inside the beam is proportional to its distance from the neutral axis and inversely proportional to the bending radius of curvature. The distribution of the longitudinal stress over the block element A'B'D'C' is shown in figure 2.7.

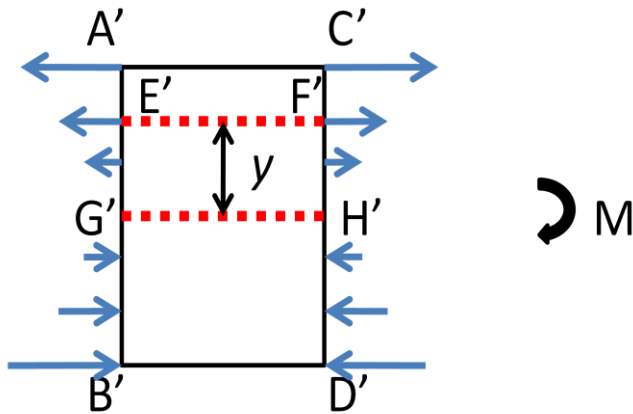


Fig. 2.7 Distribution of the bending stresses giving null total longitudinal force and a bending moment  $M$ .

Because there is no net motion of the block element A'B'D'C', so total longitudinal force is zero. The total bending moment  $M$  is

$$\begin{aligned}
 M &= w \int \sigma y \, dy \\
 &= w \frac{E}{R} \int y^2 \, dy \\
 &\equiv \frac{EI_x}{R} \quad (2.9)
 \end{aligned}$$

$I_x$  is the second moment of area. And the bending moment,  $M$ , is inversely proportional to the uniform radius of curvature,  $R$ . The constant in the equation (2.9),  $EI_x$ , is called the bending stiffness, or the flexural stiffness. With the same bending moment, the larger the bending stiffness, the larger the radius of curvature would be

(i.e. more difficult to bend). Also, since the bending stiffness is determined by both Young's modulus and the 2<sup>nd</sup> moment of area (The shape and the density distribution of the beam), therefore it is possible to create a structure that is hard to bend using material with smaller Young's modulus by increase  $I_x$ .

From equations (2.3) and (2.9), we conclude the following important relation:

$$\frac{\sigma}{y} = \frac{E}{R} = \frac{M}{I_x} \quad (2.10)$$

With equation (2.10), it is possible to calculate the stress in any position of the beam when being bent with any radius of curvature, no matter what shape the beam is, if the Young's modulus of the material is known.

## *2.4 The strength properties of solids*

In the last section, we began with Hooke's law, equation (2.3), which assumes that the object deforms linearly to the applied stress ( $\sigma$ ). But in reality, this linear relationship is only valid within a specific range of strain ( $\epsilon$ ). Now consider the behaviour of a homogeneous specimen of uniform cross-section subjected to uniaxial tension as shown in figure 2.8. The curve of the stress ( $\sigma$ ) against the strain ( $\epsilon$ ) is plotted in figure 2.9.

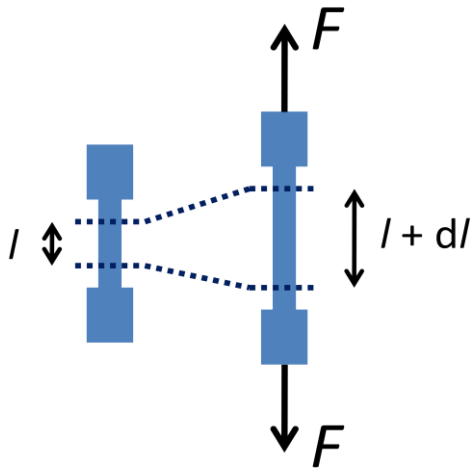


Fig. 2.8 The specimen which is subjected to a tensile strength  $F$ .

The portion OA represents the elastic deformation, which is covered by Hooke's law that  $\sigma$  is proportional to  $\epsilon$  and the deformation is reversible. If the material is ductile, elastic deformation will proceed until some critical stress  $Y$ , where plastic deformation occurs. If continuing along the plastic curve there is generally an increase in yield stress with deformation, which is known as work-hardening. If at the point B, the stress was reduced, the material will recover elastically along the path  $BO'$ , which is nearly parallel to OA. The displacement  $OO'$  is the permanent plastic extension produced in the rod. If applying the stress again, the deformation will follow the path  $O'BC$ . For a brittle material, the material could break at point A. So A is defined as the rupture point, and the stress at such point is called the tensile strength[15].

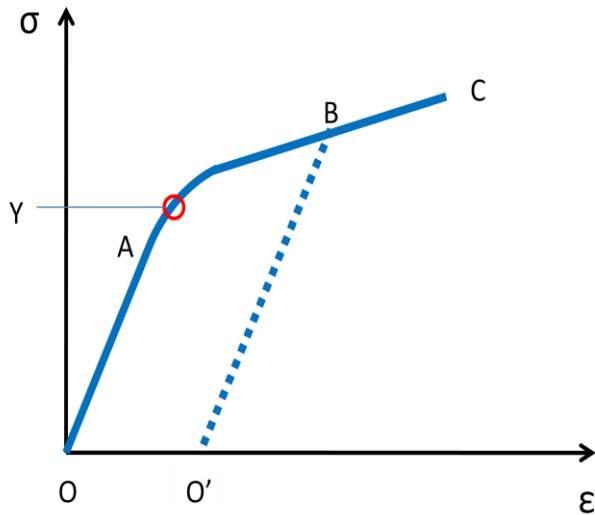


Fig. 2.9 Typical stress-strain characteristic of a ductile material, which shows an elastic deformation along OA and plastic yielding at Y (yielding stress). YC is the work-hardening process.

As to the case of compression, experiments showed that under the same condition, the rod will first deform elastically and then plastically beyond the same critical stress Y. The rod could also be subjected to hydrostatic pressure, in which case the specimen is under the same compressive stress in all directions. It is found that the plastic deformation mode does not occur even when the stress exceeds Y. If now a uniaxial stress is applied to the bar, the plastic deformation will occur when the magnitude of stress is larger than Y.

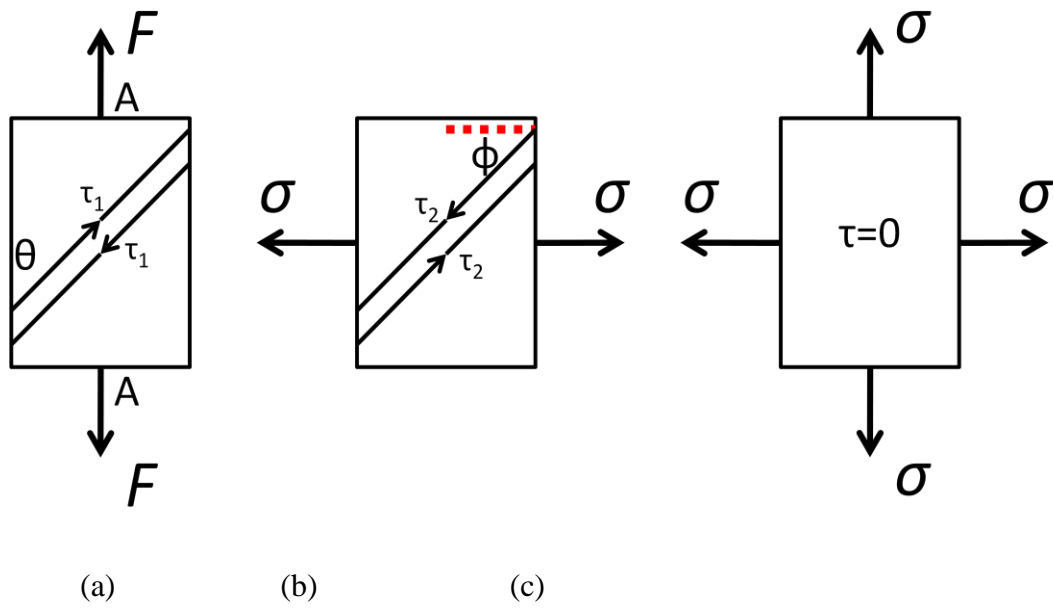


Fig 2.10 Shear stresses ( $\tau$ ) produced by tensile stresses. (a) is the vertical stress  $F$ . (b) is the horizontal stress  $\sigma$ . (c) is the 2-dimensional hydrostatic stress, which results in a null shear stress.

To explain this, consider a rectangular bar of a uniform cross-sectional area  $A$  as shown in figure 2.10(a). Suppose a tensile force  $F$  is applied to the face with the area  $A$ , the stress will be  $\sigma = F/A$ . Consider a thin slice of material with an angle  $\theta$  to the direction of stress. On one side of the slice, there is a force  $F \cos \theta$ , and on the other side the force of the same magnitude but in the opposite direction. These forces constitute a shear. The surface area of the slice is  $A/\sin \theta$ , so the shear stress  $\tau_1$  becomes

$$\begin{aligned}
 \tau_1 &= \frac{F \cos \theta}{A/\sin \theta} \\
 &= \frac{F}{A} \cos \theta \sin \theta \\
 &= \sigma \cos \theta \sin \theta \quad (2.11)
 \end{aligned}$$

So the maximum shear stress  $\tau_1$  occurs for  $\theta = 45^\circ$  with the magnitude of  $\sigma/2$ .

If the same magnitude of tensile stress  $\sigma$  is applied to the other pair of faces as shown in figure 2.10(b), the shear stress  $\tau_2$  will be

$$\begin{aligned}\tau_2 &= \sigma \cos \phi \sin \phi \\ &= \sigma \sin \theta \cos \theta \quad (2.12)\end{aligned}$$

Notice that  $\tau_1 = \tau_2$ , but in the opposite direction. So if the rectangular bar is applied with the hydrostatic pressure as mentioned in the end of last section, now shown in figure 2.10(c), the pair of shear stresses completely annuls one another. This is the basis for the statement that the hydrostatic stresses do not change the existing shear stresses in a system.

A tensile stress  $Y$  produces a maximum shear stress at  $45^\circ$  to the direction of  $Y$ . For an isotropic material, shear will therefore occur in the slip direction at  $45^\circ$  to the direction of the applied stresses. If the material is not isotropic shear may occur more easily in some direction than others. If the shear stress is exceeded in this direction slip will occur in these more favorably oriented directions. This is often observed in single crystals for example.

Finally, we may go back to the figure 2.9 to explain the interesting behaviour of permanent plastic extension. When the stress is first applied, the atoms are displaced from their equilibrium positions. The resistance to the deformation at this stage comes from the inter-atomic forces. When the tensile stress reaches the critical value of  $Y$ , the shear stress is sufficient to produce slip along an appropriate plane and plastic yielding occurs. However, the whole stress must still be supported by the displaced



atoms. This is why when the stress is removed, the rod recovers elastically and the modulus, which arises from the inter-atomic forces, is almost the same as originally.

## *2.5 Creep and stress relaxation*

So far the steady state of the stress-strain behaviour has been dealt with. However, for a ductile material such as aluminium and amorphous polymers (both are used in OLED devices), when a load has been applied and the rapid yielding has occurred, prolonged application of the same load causes the metal to continue to deform slowly with time. This time-dependent deformation at constant stress is called creep deformation. It is a diffusion-controlled process, and can be described by the equation[16]:

$$\dot{\epsilon} = B\sigma^n e^{-Q/kT} \quad (2.13)$$

where B is constant (sensitive to microstructure),  $\sigma$  is the stress, n is dictated by a range of different mechanisms of creep and is usually between 4 and 6, Q is an active energy for self-diffusion (the energy required to produce the diffusive motion of one mole of atoms), k is Boltzmann's constant, and T is the temperature in degrees Kelvin. Under low stress, thermal creep of metals is due to diffusional flow caused by diffusion of atoms in the material and is correlated to the melting temperature ( $T_m$ ). At low temperatures in the range of 0.55 to 0.8  $T_m$  (in K) diffusion occurs only at grain boundaries (Coble creep) [17], while at temperatures above 0.8  $T_m$  there is also lattice diffusion (Nabarro–Herring creep)[18], although creep deformation does occur at

lower temperature. Ordinary engineering creep rates ( $d\varepsilon/dt$ ) fall in the range of  $10^{-6} - 10^{-3} \text{ h}^{-1}$  [15, 19].

Because the traditional creep models such as equation (2.13) do not describe the very rapid initial rate of creep of which decreases within a small strain range, a power function of time must be introduced to account for this behaviour. For a constant stress:

$$\varepsilon = \varepsilon^0 + \varepsilon^+ t^m \quad (2.14)$$

, where  $t$  is the time,  $m$  is a constant independent of stress,  $\varepsilon^0$  is the time-independent strain,  $\varepsilon^+$  is the coefficient of the time-dependent term.  $\varepsilon^0$  and  $\varepsilon^+$  are both functions of stress. Take aluminium as an example, at about 178 degree C and applied stress of 138 MPa (tension),  $\varepsilon^0 = 0.21\%$ ,  $\varepsilon^+ = 0.024\%$  [20].

On the contrary, when a fixed strain is applied to an amorphous polymer, the stress will decrease with time. This process is called stress relaxation, and can be measured by the relaxation modulus ( $E_r(t)$ ):

$$E_r(t) = \frac{\sigma(t)}{\varepsilon_0} \quad (2.15)$$

, where  $\varepsilon_0$  is the strain level and  $\sigma(t)$  is the measured time-dependent stress. So basically the  $E_r(0)$  will be the young's modulus of the material.

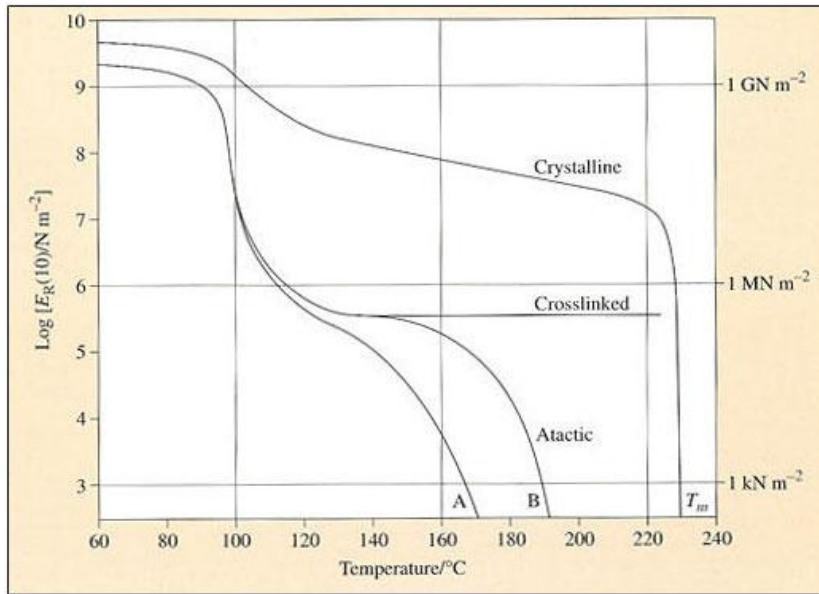


Figure 2.11 Variation of stress relaxation modulus of polystyrene (at 10 s after the strain was applied) with temperature[21].

Figure 2.11 shows the  $\log E_r$  vs. temperature behaviour of the different molecular configurations of polystyrene (PS) at 10 s after the strain was applied. The curve of the atactic (amorphous) PS shows most decay of the stress. As the temperature increase,  $E_r(10)$  drops by about a factor of 1000 within a 20 degree C span when approaching the glass transition temperature ( $T_g$ ) of PS (100 degree C). At this stage the material is leathery, that is deformation will be time dependent and not totally recoverable on release of the applied load. The plateau region of the curve at higher temperature is the rubbery region when the matter deforms in a rubbery manner. At even higher temperature, the specimen will begin to act like a liquid. The behaviour of stress relaxation will be less severe when increasing the order in the structure. For a crosslinked PS, the rubbery region forms a plateau at high temperature and will not transform into the viscous state. For the crystalline PS, the decrease in stress at  $T_g$  is already much less pronounced than other PS species.

## ***2.6 Summary***

OLED devices consist of multiple thin films and each of them has different elastic properties. Some are well known such as aluminium (generally used as cathode material) and glass (used as substrate material). Some are less well known and have been studied more recently such as indium-tin-oxide (usually used as anode material). Others are almost unknown, such as the functional small molecules of OLED because they are relatively new materials and they were expected to be used on a rigid substrate. The film thickness ( $\sim 100$  nm) also makes the mechanical characteristics difficult to measure. But even for the unknown material, acquiring an understanding of the elastic behaviour for the ductile and brittle materials can still give us an idea about how differently they may react against the stress. For the brittle materials in the flexible OLED device, it is therefore important to reduce the stress in these layers. Using the method explained in this chapter, one can calculate the stress in any layer by designing the device structure to protect the device from the possible damage caused by bending and therefore extend the usage of the flexible OLED devices in the future.

## 2.7 References

- [1] M. P. a. H. K. M. Sano, " Electroluminescence and band gap in anthracene," *Journal of Chemical Physics*, vol. 43, pp. 2920-2921, 1965.
- [2] C. W. T. a. S. A. Vanslyke, " Organic electroluminescent diodes," *Applied Physics Letters*, vol. 51, pp. 913-915, 1987.
- [3] D. D. C. B. J. H. Burroughes, A. R. Brown, R. N. Marks, K. Mackay, R. H. Friend, P. L. Burns, A. B. Holmes, "Light-emitting diodes based on conjugated polymers," *Nature*, vol. 347, pp. 539-541, 11 October 1990.
- [4] C. Rothe and A. P. Monkman, "Triplet exciton migration in a conjugated polyfluorene," *Physical Review B*, vol. 68, Aug 2003.
- [5] S. M. King, D. Dai, C. Rothe, and A. P. Monkman, "Exciton annihilation in a polyfluorene: Low threshold for singlet-singlet annihilation and the absence of singlet-triplet annihilation," *Physical Review B*, vol. 76, Aug 2007.
- [6] C. Rothe, S. King, and A. P. Monkman, "Systematic study of the dynamics of triplet exciton transfer between conjugated host polymers and phosphorescent iridium (III) guest emitters," *Physical Review B*, vol. 73, Jun 2006.
- [7] G. F. He, M. Pfeiffer, K. Leo, M. Hofmann, J. Birnstock, R. Pudzich, and J. Salbeck, "High-efficiency and low-voltage p-i-n electrophosphorescent organic light-emitting diodes with double-emission layers," *Applied Physics Letters*, vol. 85, pp. 3911-3913, Oct 25 2004.
- [8] G. F. He, O. Schneider, D. S. Qin, X. Zhou, M. Pfeiffer, and K. Leo, "Very high-efficiency and low voltage phosphorescent organic light-emitting diodes based on a p-i-n junction," *Journal of Applied Physics*, vol. 95, pp. 5773-5777, 2004.
- [9] F. C. Wang, S. Liu, H. L. Zhou, S. Sun, B. L. Qi, and G. P. Ou, "Bright green organic light-emitting devices having a composite electron transport layer," *Microelectronics Journal*, vol. 37, pp. 916-918, Sep 2006.
- [10] Z. Y. Xie, L. S. Hung, and S. T. Lee, "High-efficiency red electroluminescence from a narrow recombination zone confined by an organic double heterostructure," *Applied Physics Letters*, vol. 79, pp. 1048-1050, Aug 2001.
- [11] C. Adachi, M. A. Baldo, S. R. Forrest, and M. E. Thompson, "High-efficiency organic electrophosphorescent devices with tris(2-phenylpyridine)iridium doped into electron-transporting materials," *Applied Physics Letters*, vol. 77, pp. 904-906, Aug 2000.
- [12] W. X. Li, R. A. Jones, S. C. Allen, J. C. Heikenfeld, and A. J. Steckl, "Maximizing Alq(3) OLED Internal and External Efficiencies: Charge Balanced Device Structure and Color Conversion Outcoupling Lenses," *Journal of Display Technology*, vol. 2, pp. 143-152, Jun 2006.
- [13] "Poisson's ratio." [http://en.wikipedia.org/wiki/Poisson%27s\\_ratio](http://en.wikipedia.org/wiki/Poisson%27s_ratio), Wikipedia, 09/08/10

- [14] "Poissons ratio." [http://www.engineeringtoolbox.com/poissons-ratio-d\\_1224.html](http://www.engineeringtoolbox.com/poissons-ratio-d_1224.html), The Engineering ToolBox, 09/08/10
- [15] E. Gillam, *Materials Under Stress*. London: Newnes-Butterworths, 1969.
- [16] Z. Y. Ma and S. C. Tjong, "Creep deformation characteristics of discontinuously reinforced aluminium-matrix composites," *Composites Science and Technology*, vol. 61, pp. 771-786, 2001.
- [17] J. Fischer, N. Baltzer, and P. W. Fleetwood, "Thermal creep analysis of noble metal alloys for the ceramic-fused-to-metal technique," *Journal of Biomedical Materials Research*, vol. 48, pp. 258-264, 1999.
- [18] R. L. Bertolotti and J. P. Moffa, "Creep rate of porcelain-bonding alloys as a function of temperature," *Journal of Dental Research*, vol. 59, pp. 2062-2065, 1980.
- [19] J. S. L. William N. Findley, and Kasif Onaran, *Creep And Relaxation of Nonlinear Viscoelastic Materials with an Introduction to Linear Viscoelasticity*. Amsterdam, New York, Oxford: North-Holland Publishing Company, 1976.
- [20] J. J. a. F. Blass, W. N., "Short-Time biaxial creep of an aluminium alloy with abrupt changes of temperature and state of stress," *Trans. ASME, J. App. Mech.*, vol. 38E, p. 489, 1971.
- [21] "Physical properties of polymers."  
<http://technologyplastics.net/mod/resource/view.php?id=51>,  
OpenUPolymer101, 09/08/10

## ***Chapter 3***

### ***Experimental***

#### ***3.1 Thermal Evaporation: Thin-Film Deposition Methods***

Film deposition, by thermal evaporation, was first reported in 1887 by Nahrwold, who successfully deposited the platinum film by sublimation in vacuum[1]. In the past 50 years the number of vacuum deposition techniques has multiplied and thin film uses grown exponentially. Many modern products for the consumer, commerce, military, medical, or research applications depend on thin films. The methods used to deposit thin films are split into: Physical Vapour Deposition (PVD) and Chemical Vapour Deposition (CVD) depending on the underlying principles causing film deposition. A PVD method evaporates or sputters a material, producing a gaseous plume or beam that deposits a film on the substrate. A CVD method uses reactive, volatile compounds that decompose on a heated substrate. The starting materials are often organo- or hydrido-compounds that pyrolyse at relatively low temperatures into a non-volatile (film) component and a pumpable vapour/gas. Both methods sub-divide into a variety of techniques with auxiliary mechanisms to achieve some goal. The method we use in this work is more like PVD, a thermal evaporation method. Thus here only this method is introduced in more detail.

Thermal evaporation is a major thin film deposition technique particularly used in R&D applications where the low installation costs and inexpensive, disposable evaporant 'containers' are clear advantages. The disadvantages are: precise

temperature control may not be simple and refractory metals sometimes alloy, unexpectedly, with evaporants (evaporating Al from a W boat for example). It is necessary to define the word 'evaporation' first. Almost all information about thin film deposition characterizes material transfer from bulk-to-film as evaporation. However the correct usage of evaporation covers the 'change of state' from a liquid to gas. A 'change of state' from a solid to gas should be called sublimation. In general thin film work, however, the physical state of the bulk material is of little consequence and is probably unknown. Throughout the thesis the word 'evaporation' covers both phenomena. A common misconception is that an evaporant's vapour pressure somehow changes markedly during a transition from sublimation to evaporation. That is, a solid evaporant at its melting point has a different vapour pressure when compared to the liquid form at its melting point. This is simply not true, for any material the vapour pressure versus temperature curve is smooth at all temperatures. To give an example from everyday experience, in a glass containing ice cubes and water at 0°C, both phases have exactly the same vapour pressure.

To deposit thin film in Durham University, we use a Kurt. J. Lesker. Spectros II deposition system as shown in figure 3.1. The upright cylinder at the right is the main operation vacuum chamber featured 6 thermal heating sources for organic material and another 3 for the metal. It can be pumped down to about  $1 \times 10^{-7}$  mbar and allows two different organic materials to be evaporated at the same time. The left side of the system is the control panel using the Sigma Instruments controllers software. There is also a handle intergraded to the chamber to allow the change of the shadow-mask during operation without breaking the vacuum.



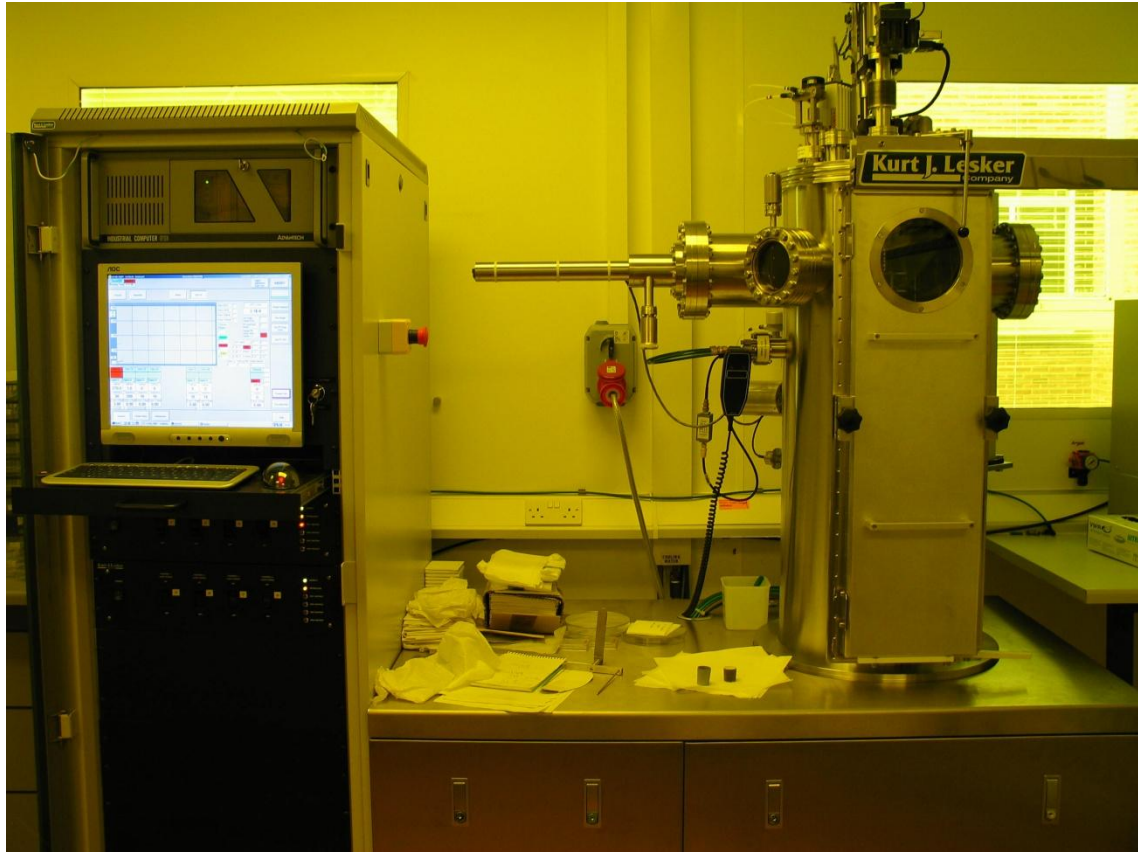


Fig. 3.1 The Kurt J. Lesker Spectros II Deposition System including the operation chamber at the right and the controller panel using the sigma instrument software at the left.

### ***3.2 Parameter determination***

In order to evaporate the thin-film to the required thickness, there are 3 parameters that are needed to be determined beforehand: tooling factor; film density; and Z-Factor (acoustic impedance). Except for the film density, which is explained by its name - the density of the thin-film, the other two parameters will be introduced in this chapter. But before that, the Quartz Crystal Microbalance (QCM) which is used to measure the thickness of the evaporated films in our evaporation system will be introduced first.

### 3.2.1 Determination of the film thickness by QCM

The thickness of the deposited film during the thermal evaporation is determined by the QCM. In an electronic oscillator circuit, a quartz crystal's natural resonant frequency determines the frequency of oscillation of the circuit. The quartz crystal is located in the vacuum deposition system above the thermal evaporating source. The relative position between the substrate and the quartz sensor is shown in Fig. 3.2. As the material is deposited on both the substrate and the crystal, the crystal becomes heavier and the resonant frequency decreases.

Equation 3.1, the so called the QCM Equation, correlates this frequency change with film thickness. Deposition rate is then derived from thickness, by dividing the change in thickness by the time period between measurements.

$$T_f = \frac{N_q \times D_q}{\pi \times D_m \times F_c \times Z} \times \tan^{-1} \left( Z \times \tan \left( \frac{\pi \times (F_q - F_c)}{F_q} \right) \right) \quad (3.1)$$

Where the crystal constant  $N_q = 1.668 \times 10^{13} \text{ Hz/m}^{-10}$

density of quartz  $D_q = 2.648 \text{ gm/cm}^3$

$T_f$  = The thickness of the deposited material

$F_q$  = the beginning quartz frequency

$F_c$  = the ending quartz frequency

$D_m$  = density of the deposited material

$Z$  = Z-factor of the deposited material

### 3.2.2 Tooling Factor

Tooling Factor compensates for the difference in material deposited on the quartz sensor versus the substrate. Tooling may be less than or greater than 100% as shown in figure 3.2.

To determine the tooling factor for the material one wants to evaporate, the standard calibration procedure as follows is used:

1. Place the substrate and a new quartz sensor in their normal position.
2. Set Tooling to an approximate value; Set Density and Z-Factor for your material.

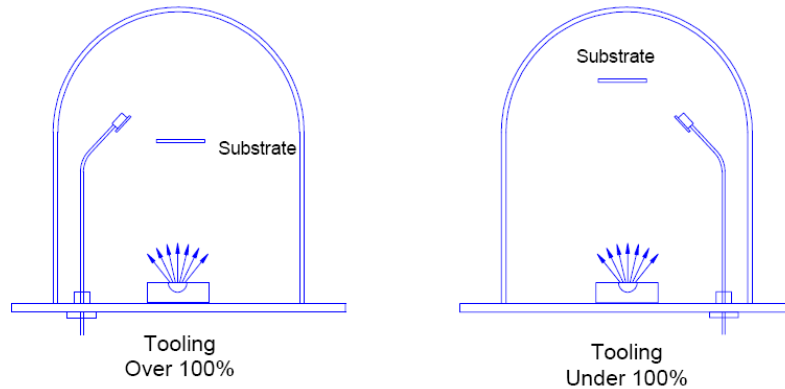


Fig. 3.2. The illustration of a simple deposition system. The heating source is at the bottom, and the sensor is shown in two different settings[2].

3. Deposit approximately 100 to 500 Å of material.
4. Use a profilometer or interferometer to measure the substrate's film thickness.
5. The correct Tooling Factor is calculated by:

$$\text{Tooling}_{\text{actual}} = \text{Tooling}_{\text{approx}} \times \frac{\text{Thickness}_{\text{actual}}}{\text{Thickness}_{\text{QCM}}}, \quad (3.2)$$

where  $\text{Thickness}_{\text{QCM}}$  denotes the thickness reading from the deposition monitor using the method of QCM.  $\text{Tooling}_{\text{approx}}$  is the tooling factor that you chose in the step 2.

$\text{Thickness}_{\text{actual}}$  is the thickness obtained in the step 4.  $\text{Tooling}_{\text{actual}}$  is the tooling factor we want for this specific material evaporated by this specific facility.

### 3.2.3 Z-Factor:

Z-Factor is a ratio of the acoustic impedances of two materials. It is used to match the acoustic impedance of the deposited material ( $Z_m$ ) to that of the base quartz sensor material ( $Z_q=8.83$ ):

$$Z = \frac{Z_q}{Z_m} \quad (3.3)$$

For example, the acoustic impedance of gold is  $Z=23.18$ ,

therefore the Z-Factor of Gold =  $8.83 / 23.18 = 0.381$

#### *Calculation of Z-Factor*

Z-Factor can also be calculated using the Shear Modulus of quartz ( $U_q$ ) and the deposited material ( $U_m$ ):

$$Z = \sqrt{\frac{D_q \times U_q}{D_m \times U_m}} \quad (3.4)$$

where  $U_q \sim 32\text{Gpa}$ ,  $D_q$  and  $D_m$  denote the density of quartz and deposited material separately.

#### *Experimental Determination of Z-Factor*

Unfortunately, Z-Factor and Shear Modulus are not readily available for many materials.

Therefore Z-Factors can also be determined empirically using the following method:

1. Deposit material until crystal life is near 50%, or near the end of life, whichever is sooner.

2. Place a new substrate adjacent to the used quartz sensor.
3. Set QCM Density to the calibrated value; Tooling to 100%.
4. Deposit approximately 1000 to 5000 Å of material on the substrate.
5. Use a profilometer or interferometer to measure the actual substrate film thickness.
6. Adjust the Z-Factor of the instrument until the correct thickness reading is shown.

Fortunately, the Z-Factor does not affect the accuracy of thickness measurement greatly if crystals are changed frequently. Fig. 3.3 shows the % Error in Rate/Thickness from using the wrong Z-Factor. For a crystal with 90% life, the error is negligible for even large errors in the programmed versus actual Z-Factor.

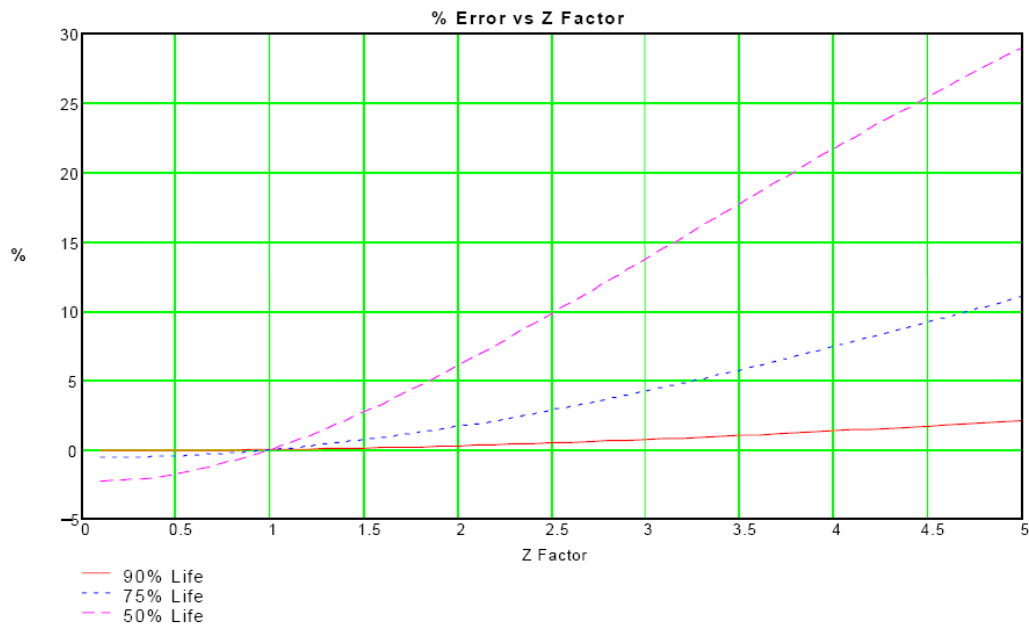


Fig. 3.3. The % Error in Rate/Thickness from using the wrong Z-Factor. This shows at 90% life of the sensor crystal, the error is negligible within a wide range of Z-Factor[3].

### 3.2.4 Unknown materials

If the film density and Z-Factor of an evaporated material is known, the tooling factor can be fixed when using the same system, the QCM equation (3.1) can be applied directly to determine the thickness of the film. However, most of the organic materials used in OLEDs have no film density information or Z-Factor determined. In this case, one can only set their value to be 1 and calibrate the 3<sup>rd</sup> parameter, the tooling factor, for each of the material. This is called the ‘effective tooling factor.’ To do so, another film-thickness determination technique other than QCM is required.

## ***3.3 Film Thickness Detection by Interferometry***

The Thin-Film analyzer F-20 is a spectral reflectivity system that is PC-based and integrates measurement and analysis software with the spectrophotometer and fiber optic measurement hardware. The system is capable of modeling complex multilayer thin films.

### 3.3.1 Theory

In the case of a thin film on the surface of another material, both the top and bottom surfaces of the film reflect light, with the total amount reflected being dependent upon the sum of these two reflections. Furthermore, these two reflections may add together constructively or destructively depending upon their phase relationship. This phenomenon is due to the wavelike nature of light, with the phase relationship determined by the difference in optical path lengths of the two reflections.

The resulting interference pattern (interference fringes) can be used to determine the thickness of the film in question, assuming that refractive index and angle of

incidence are both known. Conversely, refractive index can be determined if film thickness is known. Film thickness can thus be calculated using the following equation:

$$d = \frac{m}{2D_n \sqrt{n^2 - \sin^2 \theta}} \quad (3.5)$$

Where:  $d$  = film thickness

$m$  = number of fringes in wavenumber region used

$n$  = refractive index

$\theta$  = angle of incidence

$D_n$  = wavenumber region used ( $\nu_1 - \nu_2$ ;  $\text{cm}^{-1}$ )

### 3.2.2 Method Used for Determining Film Thickness Using the F20 Interferometer:

1. Evaporating the unknown material on 2 Si substrates to 2 different prospective thickness, marked as film A and film B, with the following parameter: (Density, Z-factor, Tooling factor) = (1, 1, System tooling factor.)
2. Using the F-20 system to determine the real thickness of film A by measuring the reflected light interference pattern.
3. To do so, one needs to also know about the material's refractive and absorption index. But neither is known.
4. Set the thickness to be the initial setting value. Use a physical model to fit the interference profile by adjusting refractive and absorption indexes to obtain the best fitting mathematically.

5. Using the Optical index thus found, determine the thickness of the film B.
6. Comparing this new thickness of film B with the prospective thickness by using equation 1.1 to obtain the 'effective tooling factor'.
7. Using the new 'effective tooling factor' to evaporate another 2 films again with 2 different thicknesses.
8. Once again measuring the real thickness by F-20
9. Keep repeating steps 4-8 until the thickness measured by F-20 is equal to the thickness setting to be evaporated.

The 'effective tooling factor' needs to be determined for every material to be evaporated.

### ***3.4 Substrate Preparation***

The cleanness of the substrate is very crucial for both OLED and Poly-LED devices. The device tends to degrade from the contaminated area which spreads to the whole device very quickly[4]. The standard chemical washing procedure is as follows:

1. Put the ITO/Glass substrate in the beaker and put the beaker in the ultrasonic bath.
2. Fill the beaker with deionized water (to remove the detergent), detergent (to remove oil), acetone (to remove most of the chemical contaminant), and isoproponal in sequence for 5 minutes each.



3. Load the substrate into the UV-Ozone box for 5 min. This treatment is roved to further lower the work function of ITO to 5.1 eV[5, 6].

### ***3.5 Electrical and Optical Measurement***

*Current-Voltage characteristic and efficiency measurement:*

Measuring the EL performance is the most common way to evaluate the OLED devices. According to Prof. Forrest of Princeton University, there are several different ways to define device efficiency[7]. First is the external quantum efficiency ( $\eta_{\text{ext}}$ ). It is the total number of photons emitted from the device in all directions divided by the number of electrons injected into the device. Now, consider the case that the device was put into an integrating sphere so that photons in all directions can all be collected and counted. The number of total emitted photons is then detected by a standard Si photodiode inside the sphere. Assume  $f(\lambda) < 1$  is the ratio of the number of photon emitted from the device to that coupled into the photodiode, and  $R(\lambda)$  is the photodiode responsivity (in unit of A/W).

$$R(\lambda) = \frac{I_{\text{det}}(\lambda)}{f(\lambda)P_{\text{OLED}}(\lambda)}$$

where  $I_{\text{det}}$  is the photocurrent generated in the photodiode, and  $P_{\text{OLED}}(\lambda)$  is the power emitted at center wavelength  $\lambda$ .

So the total number of photons emitted from the device is

$$n_{\text{photon}} = \frac{\int \lambda I_{\text{det}}(\lambda) d\lambda}{hc \int f(\lambda) R(\lambda) d\lambda}$$

where  $h$  is the Planck's constant, and  $c$  is the speed of light.

While the total number of electrons injected into the device is

$$n_{electron} = \frac{I_{OLED}}{q}$$

$q$  is the electron charge. The external quantum efficiency ( $\eta_{ext}$ ), by definition, would be

$$\begin{aligned} \eta_{ext} &= \frac{n_{photon}}{n_{electron}} \\ &= \frac{q \int \lambda I_{det}(\lambda) d\lambda}{hc I_{OLED} \int f(\lambda) R(\lambda) d\lambda} \quad (3.6) \end{aligned}$$

Notice that equation (3.6) only concerns energy, so  $\eta_{ext}$  weighs the light at every wavelength equally. However the human eye is not equally sensitive to all visible wavelengths, so the luminous power efficiency ( $\eta_p$ ) (lm/W) which includes the photopic response of human eyes is also used. The normalized spectral curve,  $g(\lambda)$ , as shown in the figure 3.4 is based on the nature of human eye, which has the peak response to the light of  $\lambda=555$  nm.

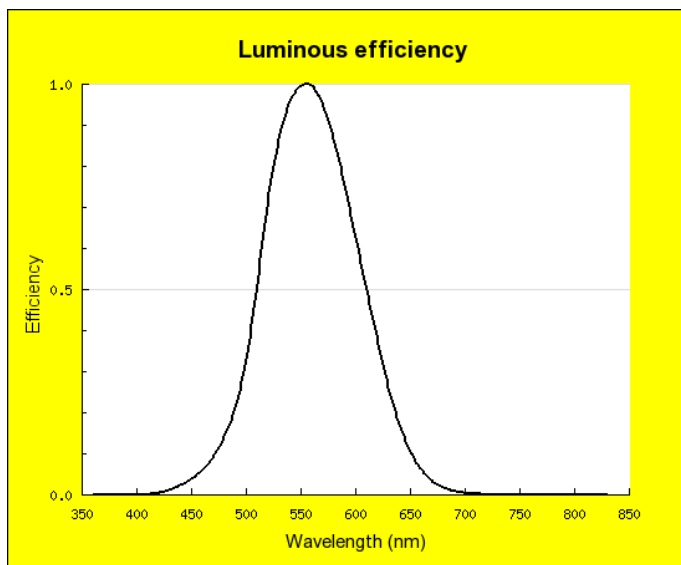


Fig. 3.4 The normalized photopic response curve of human eyes. The peak response is 683 lm/W at  $\lambda=555$  nm[8].

So the luminous power efficiency ( $\eta_p$ ) can be defined as

$$\eta_p = \frac{\phi_0 \int g(\lambda) I_{det}(\lambda) d\lambda}{I_{OLED} V \int f(\lambda) R(\lambda) d\lambda} \quad (3.7)$$

$\Phi_0 = 683 \text{ lm/W}$ .  $V$  is the voltage applied to the device.

From power efficiency (lm/w), which is a unit handy to engineers, it is favorable to convert to another commonly used efficiency: the current efficiency ( $\eta_j$ ) (cd/A), as this unit provides a clear view about how many electrons in and how many photons out. Lumen and candela are related by  $1 \text{ cd} = 1 \text{ lm/sr}$ , therefore for a Lambertian source emitting into the half plane,  $1 \text{ lm} = \pi (1 \text{ cd})$ . One can calculate the current efficiency ( $\eta_j$ ) by

$$\eta_j = \frac{AL}{I_{OLED}} \quad (3.8)$$

$A$  is the device active area and  $L$  is the brightness in unit of  $\text{cd/m}^2$ .

Finally, in my study of OLED devices throughout this thesis, an Agilent 6632B (20 V, 5 A) power supply is used as the current source to drive the devices. The electroluminescence (EL) was measured by an integrating sphere (Labsphere LMS-100), which had been calibrated using a NIST traceable standard lamp according to the different OLED sample holder used.

The Luminance meter Konica-Minolta LS-110 was also used to measure the brightness of the EL as the reference of the results from the integrating sphere.

#### *EL Spectrum measurement:*

The EL spectrum is obtained using the Ocean Optics USB 4000 device, which is connected to the back of the Labsphere LMS-100 integrating sphere through the optical fibre.

### ***3.6 Nanoindentation***

A very important part of this thesis is the determination of the elastic properties of the small molecule thin-films used in the OLED devices. To obtain such information, the nanoindentation technique was applied using the Hysitron TI 950 TriboIndenter as shown in figure 3.5 and the analysis introduced by W. C. Oliver and G. M. Pharr[9]. For the test, a sharp triangular pyramid indenter (Berkovich indenter) made by diamond was used to indent the surface of the thin-film, and the shape of the deformation of the surface was observed by a scanning electron microscope (SEM) spontaneously. A cross-section of an indentation is shown in figure 3.6.



Fig. 3.5 The Hysitron TI 950 TriboIndenter[11].

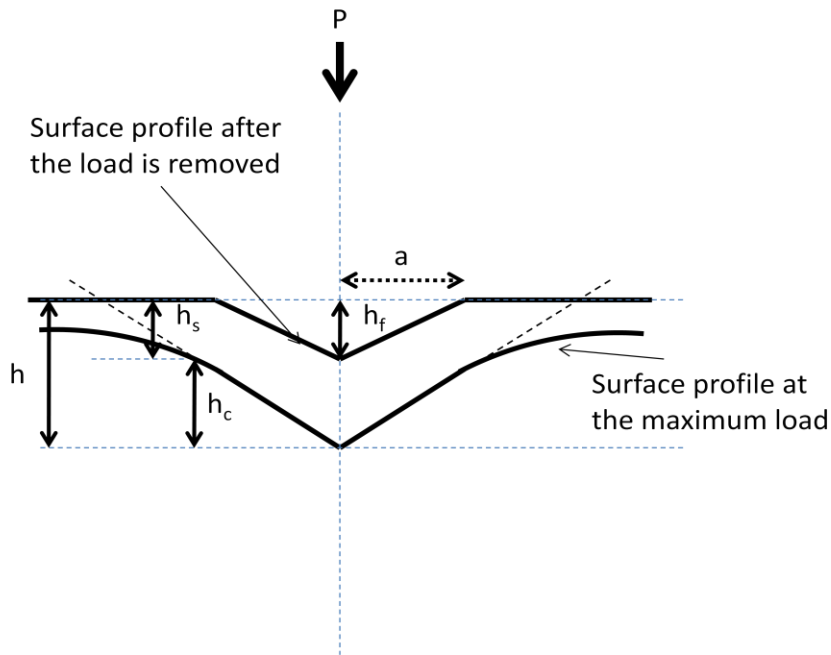


Fig. 3.6 The schematic representation of a section through an indentation.  $a$  is the radius of the indenter  $h_c$  is the contact depth,  $h_f$  is the final residual depth,  $h_s$  is the displacement of the surface at the perimeter of the contact, and  $h$  is the total displacement.

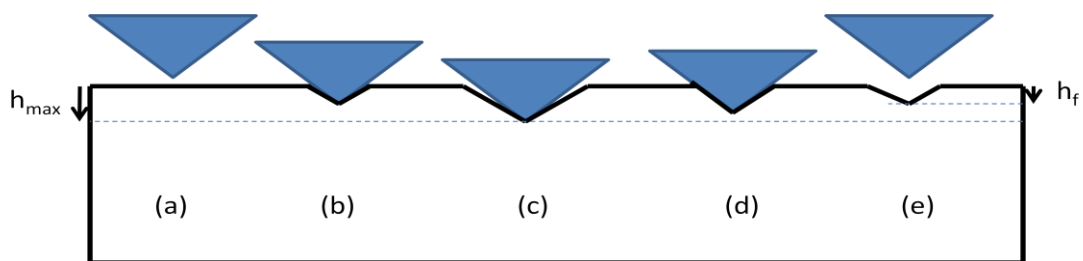


Fig. 3.7 (a) to (e) is the sequence of how the tested surface responds to the indenter. (a) to (c) is the loading process, where the deformation from (a) to (b) is mainly plastic. While at (c) the indenter reaches the maximum penetration depth  $h_{max}$ . (c) to (e) is the unloading process, where the displacement from (c) to (d) is mainly elastic.  $h_f$  in (e) is the final depth or the residual depth of the indentation.

The sequence of indentation is shown in figure 3.7. At anytime during the loading and unloading, the total displacement  $h$  can be written as

$$h = h_c + h_s \quad (3.9)$$

where  $h_c$  is the contact depth (vertical distance along which contact is made) and  $h_s$  is the displacement of the surface at the perimeter of the contact. Initially, the displacement is mainly plastic deformation. As the load increases, the surface will begin to deform elastically. At peak load, the load and displacement are defined as  $P_{max}$  and  $h_{max}$ , and the radius of the contact circle is  $a$ . Upon unloading, the displacement is recovered elastically and when the indenter is fully withdrawn, the residual depth is defined as the final depth and denoted by  $h_f$ .

The magnitude of the load and the displacement of the surface were also recorded as shown in the typical curve plotted in the figure 3.8.

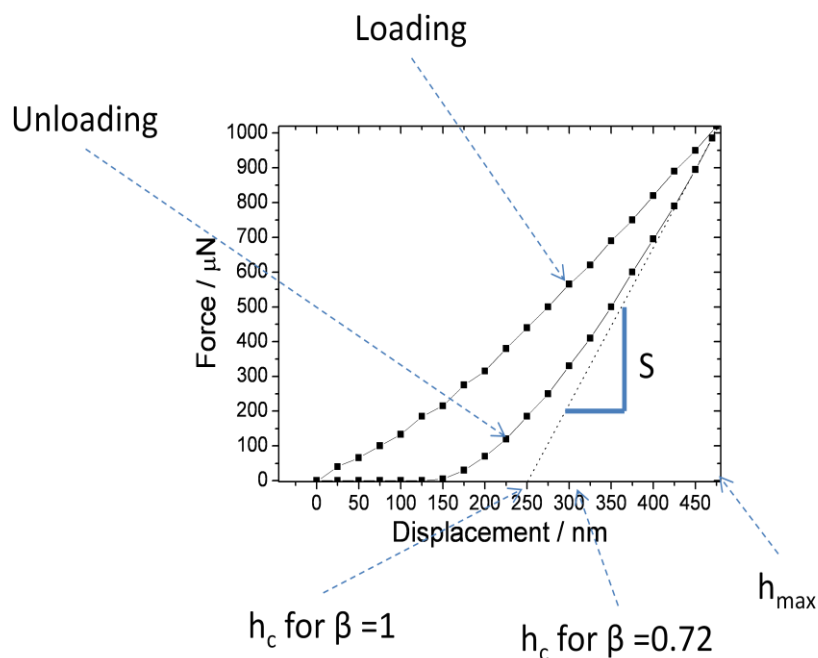


Fig. 3.8 The schematic load-displacement curve of the organic thin-film.

Now,  $P$  is the loading pressure,  $h$  is the displacement according to the load, and  $S$  is the initial unloading contact stiffness. According to Sneddon's solution[10] to the case of indentation of an elastic half-space for a cylindrical punch approach to the elastic behaviour, the relation of these 3 key parameters is

$$P = \frac{4\mu a}{1-\nu} h \quad (3.10)$$

where  $\nu$  is the Poisson's ratio,  $\mu$  is the shear modulus and  $a$  is the radius of the cylinder.

Because the area of the contact circle projected onto the surface,  $A$ , is  $\pi a^2$  and the shear modulus ( $\mu$ ) is related to the elastic modulus ( $E$ ) as shown below:

$$E = 2\mu(1 + \nu) \quad (3.11)$$

By substituting equation (3.11) into equation (3.10), one can obtain

$$\begin{aligned} S &= \frac{dP}{dh} \\ &= \frac{2}{\sqrt{\pi}} E_r \sqrt{A} \end{aligned} \quad (3.12)$$

$E_r$  is the reduced elastic modulus, where

$$\frac{1}{E_r} = \frac{1-\nu_i^2}{E_i} + \frac{1-\nu^2}{E} \quad (3.13)$$

$E$  and  $E_i$  are the Young's moduli of the specimen and the indenter, and  $\nu$  and  $\nu_i$  are the Poisson's ratio of the specimen and the indenter as well.

Equation (3.12) can be rewritten as

$$E_r = \frac{\sqrt{\pi}}{2} \frac{S}{\sqrt{A}} \quad (3.14)$$

Therefore from the initial unloading slope (S), the reduced elastic modulus of the specimen will be obtained once A is known. A is determined by the geometry of the indenter and the contact depth ( $h_c$ ). So we can assume that  $A = f(h_c)$ , where the function  $f$  should be established experimentally prior to the analysis. From equation (3.9),  $h_c = h_{max} - h_s$ . Since  $h_{max}$  is measurable, the only term to be determined is the displacement of the surface at the contact perimeter ( $h_s$ ).

The deformation of the surface at the contact perimeter obviously depends on the indenter geometry again. For a conical indenter, according to the deduction by Sneddon[10], the relation of  $h_s$ ,  $h$ , and  $h_f$  is

$$h_s = \frac{\pi-2}{\pi} (h - h_f) \quad (3.15)$$

, where the quantity  $(h - h_f)$  is the elastic component of the displacement. In addition, Sneddon's force-displacement relationship for the conical indenter yields

$$(h - h_f) = 2 \frac{P}{S} \quad (3.16)$$

Remembering that S is the slope of the initial unload curve, substitution of equation (3.16) into equation (3.15) gives us;

$$h_s = \beta \frac{P_{max}}{S} \quad (3.17)$$

where  $\beta$  (~0.72) is the geometric constant for the conical indenter and is defined by

$$\beta = \frac{2}{\pi} (\pi - 2) \quad (3.18)$$

Taking figure 3.8 as an example, from equation (3.9) and (3.17),  $h_c$  will be  $475 - (0.72 \times 225) \sim 313$  nm. The same argument can be applied to different geometry of indenters: for the flat punch,  $\beta = 1$ , and for the paraboloid,  $\beta = 0.75$ . Oliver, in his



report, concluded that by studying various materials,  $\beta = 0.75$  is the best approximation for the Berkovich indenter[9] used in our experiment. Finally, once  $h_c$  is known, the projected area of the elastic contact,  $A$ , could be determined using  $A = f(h_c)$ , so that  $E_r$  is obtained by equation (3.14), and subsequently the Young's modulus  $E$  of the specimen by equation (3.13).

### ***3.7 Summary***

The thickness of the OLED layers (excluding the substrate), as mentioned before, is generally only 100 – 200 nm. Any variation of the thickness could affect both optical and electrical characteristics of the device. Therefore the calibration of the deposition system described in this chapter is crucial to the further analysis of the OLED devices throughout the thesis. The nano-indentation technique will further provide the mechanical information on the organic thin films used in the OLED devices, which is a first and important step toward evaluating the usage of OLED in the flexible applications.

### 3.8 References

- [1] R. Nahrwold, *Ann. Physik*, vol. 31, p. 467, 1887.
- [2] "Z factor," <http://www.sig-inst.com/faqpage.htm>, Sigma Instruments FAQs, 02/03/08
- [3] "QCM life," <http://www.sig-inst.com/faqpage.htm>, Sigma Instruments FAQs, 02/03/08
- [4] H. Aziz and G. Xu, "A degradation mechanism of organic light-emitting devices," *Synthetic Metals*, vol. 80, pp. 7-10, Jun 15 1996.
- [5] Y. Park, V. Choong, Y. Gao, B. R. Hsieh, and C. W. Tang, "Work function of indium tin oxide transparent conductor measured by photoelectron spectroscopy," *Applied Physics Letters*, vol. 68, pp. 2699-2701, May 1996.
- [6] W. K. C. S.K. So, C.H. Cheng, L.M. Leung and C.F. Kwong, "Surface preparation and characterization of indium tin oxide substrates for organic electroluminescent devices," *Applied Physics A*, vol. 68, pp. 447-450, 1999.
- [7] S. R. Forrest, D. D. C. Bradley, and M. E. Thompson, "Measuring the efficiency of organic light-emitting devices," *Advanced Materials*, vol. 15, pp. 1043-1048, Jul 2003.
- [8] "Luminous efficiency functions," <http://www-cvrl.ucsd.edu/cie.htm>, Older CIE Standards, 20/12/10
- [9] W. C. Oliver and G. M. Pharr, "An improved technique for determining hardness and elastic modulus using load and displacement sensing indentation experiments," *Journal of Materials Research*, vol. 7, pp. 1564-1583, Jun 1992.
- [10] I. N. Sneddon, "The relation between load and penetration in the axisymmetric boussinesq problem for a punch of arbitrary profile," *International Journal of Engineering Science*, vol. 3, pp. 47-57, 1965.
- [11] "hysitron instrument platform comparison," <http://www.hysitron.com/products/ti-series/ti-950-triboindenter>, Hysitron Instrument Website, 13/06/11

## ***Chapter 4***

### ***Comparison of the plastic-based and the glass-based OLED devices in terms of electroluminescence performance***

In this chapter an identical OLED structure was deposited onto the ITO/glass and the ITO/PET substrates and their EL performance were compared to evaluate the FOLED device using ITO as the anode.

#### ***4.1 Background***

One of the biggest challenges blocking the way to commercialize the bottom-emitting FOLED devices is the lack of a mechanically robust: it has to be highly transparent, highly conductive, work function matched, and deposited via low temperature process. ITO, the most commonly used anode material for rigid OLEDs, has been questioned about its usage in FOLED because of the high temperature processing required ( $> 300$  °C) for sputtering, which leads to the appearance of cracks on the ITO due to different coefficients of thermal expansion (CTE) for the ITO and PET substrate[1]. Various alternative anode materials have been proposed recently to replace the ITO, such as  $\text{TiO}_2/\text{Ag}$  composite anode[2], ruthenium-oxide-coated anode[3], and metal lines supported poly(3,4-ethylenedioxythiophene) poly(styrenesulfonate) (PEDOT:PSS)[4].

Although they are all claimed to be very competitive in device performance, none has comparable sheet resistance to ITO, which has been well-studied and established as a stable material with matured industrial fabrication. For the past few years, low-temperature ITO sputtering techniques have also been developed to improve the film quality and thus enhance the conductivity of ITO coating on the plastic film [5]. Therefore in this chapter, identical OLED structures were thermally evaporated onto the ITO/PET and ITO/Glass substrates and their EL performance was compared to see whether ITO is suitable to be used as the anode of the FOLED devices.

## 4.2 Experiment

The FOLED devices were fabricated using ITO coated PET sheets purchased from Sigma-Aldrich with two different ITO thicknesses and sheet resistances. The reference devices were fabricated on to ITO/glass substrates supplied by Visiontek Systems Ltd. The specifications of the substrates quoted from the suppliers' web page are listed in the table 4.1.

Substrate material / thickness (mm)			ITO thickness (nm)	ITO sheet resistance ( $\Omega$ /sq)	Transmittance at 550 nm
A	Glass	1.1	150	15	89%
B	PET	0.127	120	35	>86%
C	PET	0.127	100	60	>79%

Table 4.1 Substrate B is the ITO(35 $\Omega$ /sq)/PET, substrate C is the ITO(60 $\Omega$ /sq)/PET, and the substrate A is the ITO(15 $\Omega$ /sq)/glass.

The sheet resistance of ITO on the glass substrate is 4 times lower than the ITO on the PET when their thicknesses are both 100 nm. The time required to etch the ITO/glass sample while patterning the anode is about 4 times longer than to etch the ITO/PET sample as well. This indicated that the adherence of the ITO to the PET substrate is not as good as that to the glass substrate.

To prepare the samples, all the substrates were cleaned by acetone and isopropanol in the ultrasonic bath for 10 minutes respectively, then exposed in the UV Ozone box for 7 minutes, and finally loaded into the Kurt J. Leskur Spectros II Deposition System. The component layers of the OLED were then deposited under vacuum of  $4 \times 10^{-7}$  mbar with the structure of aluminium (100 nm)/lithium fluoride (1 nm)/ TPBi : Ir(ppy)<sub>3</sub> (200 nm)(1:0.2 by rate)/ ITO / Sub.

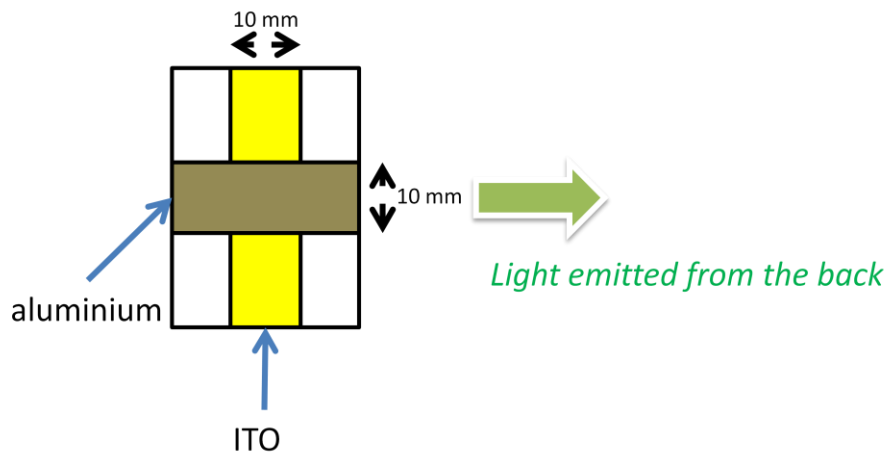


Fig. 4.1 Device plan. The OLED is sandwiched by the yellow, 10mm x 30mm stripe of ITO at the bottom, and the grey, 10mm x 20mm stripe of aluminium stripe on the top. The light is emitted from the back.

The fabricated device with the 10 mm x 10 mm OLED pixel is showed in figure 4.1. The EL of device A, B and C were finally measured in an integrating sphere (Labsphere LMS-100) with the DC power supply Agilent 6632B.

### ***4.3 Results and discussion***

To compare the EL performance of the OLED devices on the glass substrate and the PET substrate, more than 30 devices were fabricated and tested (3 devices were made on substrate A, B and C at the same time in one deposition, and more than 10 runs of deposition were conducted). Figure 4.2 shows the typical JV characteristic difference of the OLED devices on the 3 difference substrate from 0 to 8V. At 8V, the current density of device A, B and C (with the glass substrate) are about 4.1, 2.7, and 2.66 mA/cm<sup>2</sup> respectively (1 : 0.66 : 0.65) and J of the two PET devices are similar despite of the sheet resistance difference. Although sheet resistance of the three ITO/substrates were measured and confirmed to be the same as claimed in table 4.1 beforehand, it should not be the major factor that contributed to the difference of J since comparing to the electrical resistance of OLED device, the sheet resistance of the ITO is not significant. So the lower J of the device B and C might be due to the roughness of the ITO surface, which will be discussed later in this chapter.

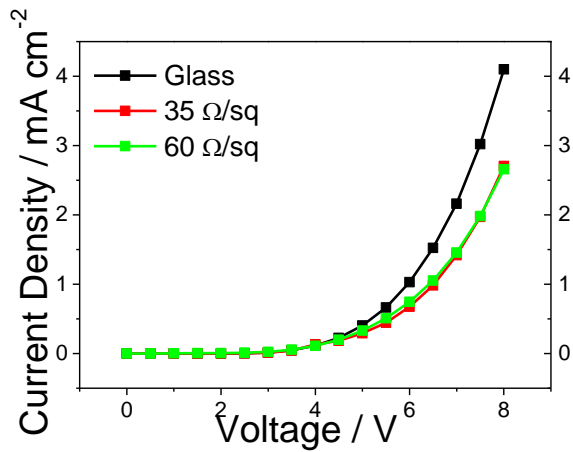


Fig. 4.2 The J-V characteristic of the OLED devices based on substrates A, B, and C.

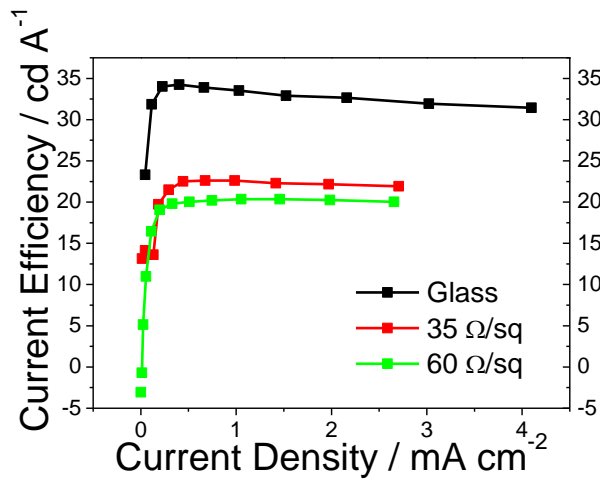


Fig. 4.3 The current efficiency vs. current density of the OLED devices based on substrates A, B, and C.

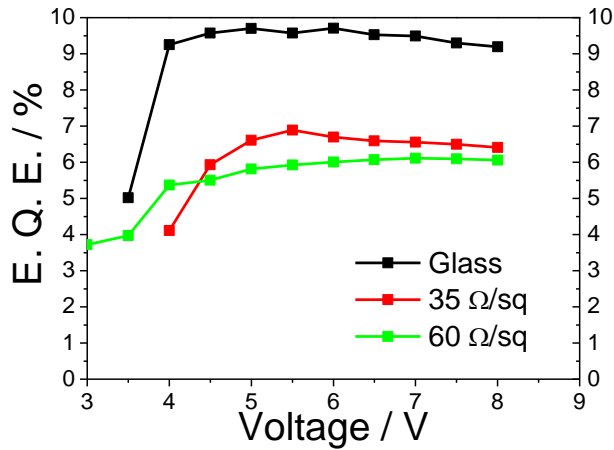


Fig. 4.4 The external quantum efficiency of the OLED devices vs. applied voltage based on substrates A, B, and C.

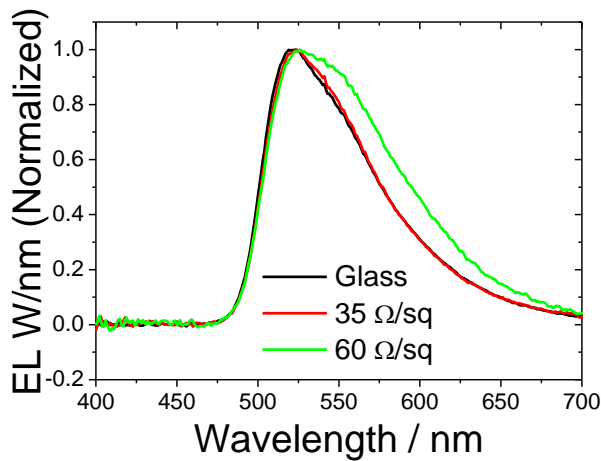
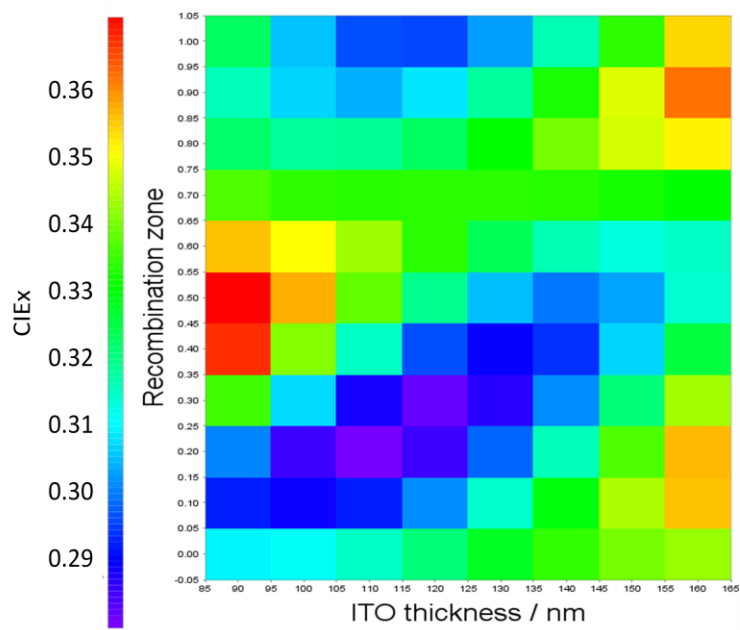


Fig. 4.5 The normalized EL spectrum (W/nm) of the OLED devices based on substrates A, B, and C.

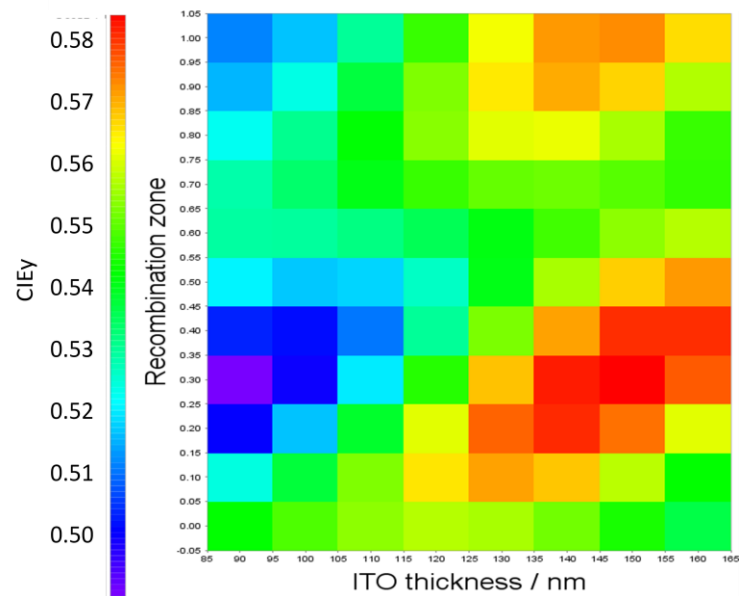
The current efficiency of the 3 devices at 8V is about 31.4, 21.9, and 20 cd/A (1 : 0.7 : 0.64) as shown in figure 4.3. The two PET based devices again show similar efficiency and worse than their glass based counterpart. As so the external quantum efficiency (E.Q.E., or  $\eta_{\text{ext}}$ ) shown in figure 4.4 (9.2% : 6.4% : 6% or 1 : 0.7 : 0.65) follows the same trend.  $\eta_{\text{ext}}$  is the multiple of the internal quantum efficiency ( $\eta_{\text{int}}$ )



and the out-coupling efficiency ( $\eta_c$ ), and  $\eta_c$  can depend on the ITO thickness, the refractive index of the substrate, and the transmittance of the composite substrate. It is worth mentioning here that the meaning of  $\eta_{\text{ext}}$  and current efficiency is similar, just that the former weighs all photons equally, while the latter weighs the photons according to the photopic response of the eye[6]. Finally, the normalized EL spectrum (W/nm) at 8V is shown in figure 4.5. It is seen that the spectrum of device A and B are similar while device C becomes broader. This can be a micro-cavity effect and arises from the different thickness of ITO. The commercial optical simulation software, SETFOS, is used to confirm the hypothesis. It is assumed that the refractive index of the substrate is 1.5 for all three devices and sweeping the combination zone across the whole organic layer, the simulation result does showed a significant optical effect on the thickness of ITO to the luminance, as reported by Kim and Kim[7], as well as the EL spectrum. The latter is used to determine the possible recombination position. For device (A, B, C), the thickness of ITO is (150 nm, 120 nm, 100 nm), the measured CIE<sub>x</sub> is (0.341, 0.343, 0.373), and the CIE<sub>y</sub> is (0.609, 0.607, 0.585). So basically the trend is the CIE<sub>x</sub> decreases and the CIE<sub>y</sub> increases as the thickness of ITO increased from 100 nm to 150 nm.



(4.6a)



(4.6b)

Figure 4.6a, 4.6b The simulation results of the CIE<sub>x</sub> (left) and CIE<sub>y</sub>(right) changes with the ITO thickness and the exciton recombination zone of the OLED structure Al(100 nm)/TPBi(200 nm)/ITO(90 nm – 160 nm)/Sub (n = 1.5). The recombination

zone varies from 0 (interface of TPBi and Al) to 1 (interface of TPBi and ITO). The colour of the blocks indicate the value of CIE index. Red is relatively larger than purple in the same diagram.

Comparing to the simulation result as shown in figure 4.6a and 4.6b, it is found that the CIE diagram shift of the recombination zone from 0.4 to 0.6 (0 is the interface of Al/TPBi and 1 is the interface of TPBi/ITO) correspond to the experimental results, which suggests that the recombination zone of the OLED devices is somewhat near the centre of the OLED layer. Figure 4.7 shows further the normalized luminance change as the ITO thickness change from 90 nm to 160 nm for the exciton recombination zone being 0.4, 0.5, and 0.6.

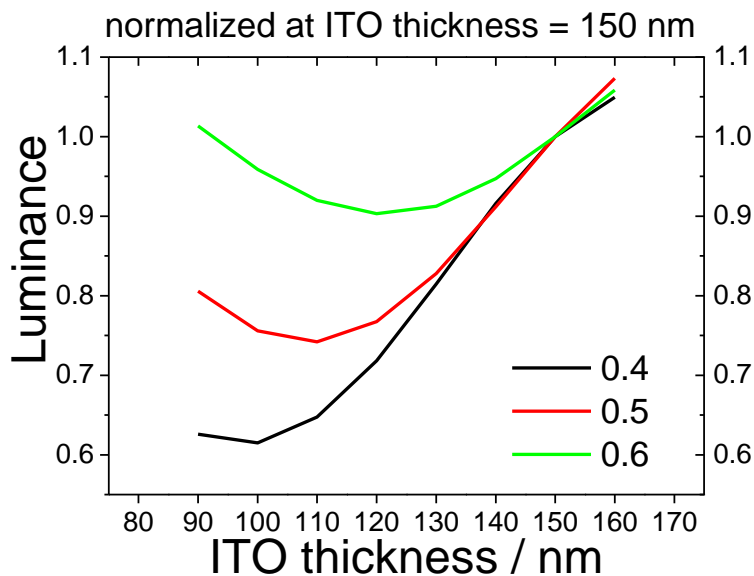


Fig. 4.7 The luminance of OLED against the ITO thickness for the exciton recombination zone being 0.4, 0.5, and 0.6. The luminance is normalized at the value at ITO thickness of 150 nm of each curve.

For the curve 0.6, the luminance of ITO thickness 150 nm is similar to 100 nm, while 120 nm has the minimum. For the curve 0.4, the luminance of ITO thickness 100 nm is merely 60% of the 150 nm, and 85% of the 120 nm. For the curve 0.5, the luminance of ITO thickness 100 nm and 120 nm are similar and both are about 75% of the 150 nm. Compares with the experiment data that the devices B and C had similar performance and both are worse than device A, the curve of the exciton recombination zone being 0.5, that is in the centre of the TPBi:Irppy layer, is the most reasonable choice. Therefore about 25% of the out-coupling light lost (compares to device A) can be related to the ITO thickness change.

The other factor is the transmittance difference of the substrates. The Shimadzu UV 3600 was used to measure the transmittance of the substrate A, B, and C, and the result is shown in figure 4.8.

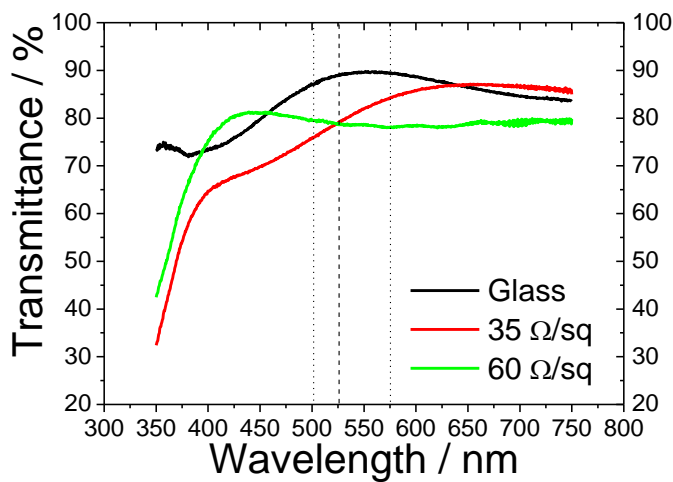
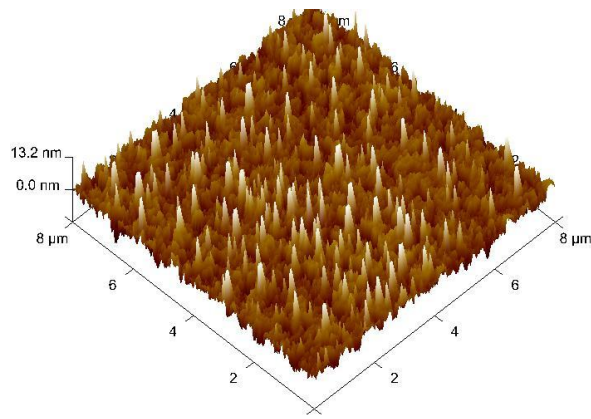


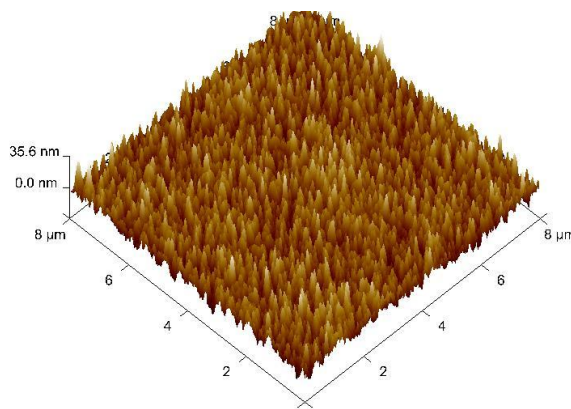
Fig. 4.8 The transmittance of the substrate A (black), B (red), and C (green). The dash line indicates the peak, and the region of two dot lines the Full Width at Half Maximum (FWHM) of the EL spectrum.

Although the transmittances at the wavelength 550 nm are indeed as claimed by the supplier for three of them, but the curves behave differently. If integrating the area between the two dot lines (the Full Width at Half Maximum (FWHM) of the EL spectrum), the ratio of the three substrates is about 1 : 0.9 : 0.88. Again, the two PET devices are similar and both are smaller than the glass device. So another 10% lost of light can be related to the transmittance of the substrate.

Combining the transmittance lost and the micro-cavity effect would give us 10% + 25% ~ 35% total optical lost ( $\eta_c$ ), which is close to the number of E.Q.E lost. Since E.Q.E ( $\eta_{ext}$ ) is the product of out-coupling efficiency ( $\eta_c$ ) and internal quantum efficiency ( $\eta_{int}$ ), it implied that the internal quantum efficiency does not change when the same OLED structure was evaporated onto the PET substrate instead of the glass substrate. The last unanswered question is the smaller injected current of the PET based devices than the glass based device. The AFM images, as shown in figure 4.9a and 4.9b, suggest that the ITO surface of the PET substrate is rougher than the glass substrate, and it has been reported that the ITO roughness can affect the current injection into the OLED dramatically[8, 9]. Secondly, since the injecting barrier on the cathode side is fixed, it might be the ITO work function changed because of different sputtering technology that affects the hole injecting on the anode side, as the work function of ITO can be sensitive to different surface conditions[10]. Thirdly the electrical contact of the soft PET-based device when measuring is worse than the hard glass-based device. The above three issues might all together contribute to the 33% lost of the inject current for the PET devices.



(4.9a)



(4.9b)

Fig. 4.9a, 4.9b The AFM image of the ITO surface of the substrate A (4.9a) and substrate B (4.9b).

#### ***4.4 Summary***

To sum up, it has been shown that the E.Q.E. and the current efficiency of the two PET based devices are all similar despite of their sheet resistance difference, and are 30 - 35% worse than the glass based device. This can be explained by the micro-cavity effect of the ITO thickness difference and the transmittance of the substrates. On the other hand, the 30% lower inject current density of the PET device than the

glass device can be due to the rougher ITO surface of the PET substrate, the change of ITO work function because of different coating technology, and the worse electrical contact when taking measurement. Most importantly, it is shown that the OLED internal quantum efficiency does not change when fabricating on the PET substrate. Therefore with a proper thickness of ITO and improved transmittance and ITO surface roughness, with the same applied voltage, it is possible to make the FOLED device with brightness 70% to 80% of its glass-based OLED counterpart.

## 4.5 References

- [1] M. Boehme and C. Charton, "Properties of ITO on PET film in dependence on the coating conditions and thermal processing," *Surface & Coatings Technology*, vol. 200, pp. 932-935, Oct 2005.
- [2] K. Yamada, K. Tamano, T. Mori, T. Mizutani, M. Sugiyama, and I. Ieee, "Organic light-emitting diodes using semi-transparent anode for flexible display," in *Proceedings of the 7th International Conference on Properties and Applications of Dielectric Materials, Vols 1-3* New York: Ieee, 2003, pp. 49-52.
- [3] K. Hong and J. L. Lee, "Enhancement of electroluminescence properties in OLEDs on polyethylene terephthalate with ruthenium-oxide-coated anode and Mg-Al alloy cathode," *Journal of the Electrochemical Society*, vol. 154, pp. H782-H788, 2007.
- [4] S. M. Stephan Harkema, Marco Barink, Harmen Rooms, Joanne S. Wilson, Ton van Mol and Dirk Bollen, "Large Area ITO-free Flexible White OLEDs with Orgacon™ PEDOT:PSS and Printed Metal Shunting Lines," *Proc. of SPIE: Organic Light Emitting Materials and Devices XIII*, vol. 7415, pp. 74150T-1, 2009.
- [5] S. J. Wakeham, M. J. Thwaites, B. W. Holton, C. Tsakonas, W. M. Cranton, D. C. Koutsogeorgis, and R. Ranson, "Low temperature remote plasma sputtering of indium tin oxide for flexible display applications," *Thin Solid Films*, vol. 518, pp. 1355-1358, Dec 2009.
- [6] S. R. Forrest, D. D. C. Bradley, and M. E. Thompson, "Measuring the efficiency of organic light-emitting devices," *Advanced Materials*, vol. 15, pp. 1043-1048, Jul 2003.

- [7] S. Y. Kim and J. J. Kim, "Outcoupling efficiency of organic light emitting diodes and the effect of ITO thickness," *Organic Electronics*, vol. 11, pp. 1010-1015, Jun.
- [8] S. H. Kim and C. Yoon, "Comparison of ITO prepared by capacitive RF magnetron sputtering and DC facing target sputtering as an anode on the organic light emitting diode," *Physica Status Solidi a-Applications and Materials Science*, vol. 206, pp. 2206-2211, Sep 2009.
- [9] Y. H. T. a. Y. S. H. e. a. K. B. Kim, "Relationship between surface roughness of indium tin oxide and leakage current of organic light-emitting diode," *Japanese Journal of Applied Physics Part 2-letters*, vol. 42, pp. L438-L440, 2003.
- [10] W. K. C. S.K. So, C.H. Cheng, L.M. Leung and C.F. Kwong, "Surface preparation and characterization of indium tin oxide substrates for organic electroluminescent devices," *Applied Physics A*, vol. 68, pp. 447-450, 1999.



## ***Chapter 5***

### ***A nano-indentation study of the reduced elastic modulus of Alq<sub>3</sub> and NPB thin-film used in OLED devices***

In the last chapter, it is shown that the PET based FOLED device can be competitive to the glass based OLED device if the thickness of ITO is optimized and the transmittance and the surface roughness of the ITO on the PET film can be improved further. In this chapter, the Young's moduli of the conventional small molecules: Tris-(8-hydroxyquinoline) aluminum (Alq<sub>3</sub>) and N,N'- Bis(naphthalen-1-yl)-N,N'-bis(phenyl)benzidine (NPB) were investigated in order to evaluate their use in the FOLED device. The work has been published in **Organic Electronics** Volume 11, Issue 3, March 2010, Pages 450-455

#### ***5.1 Background***

Organic Light Emitting Diode (OLED) distinguishes itself by having the potential to be mechanically flexible. Unlike LCDs and inorganic LEDs, OLEDs or printable Polymer LEDs can be fabricated on a plastic substrate to make the device flexible, and amenable to roll-to-roll manufacture. It is therefore essential to understand how this rolling process might mechanically damage the multi-layer structured OLED, and

studies towards this aim have appeared in the last 5 years. Most of these studies, however, have focused on what was estimated to be the most brittle layer in the structure- the commonly-used Indium Tin Oxide (ITO) layer as the anode[1, 2]. However, study of the elasticity properties of the organic conducting and emissive layers is still rare in literature[3]; to obtain such information from a 100 nm thick thin-film is not a simple task. One method potentially able to perform this task is nano-indentation.

Nano-indentation, as explained shortly in chapter 3, has been used routinely in the mechanical characterization of thin films and thin surface layers in recent years[4]. The technique applies a programmed function of increasing and decreasing load to the surface of interest with an indenter of well-defined shape and continuously measures the indenter displacement. The advantage of this method is that mechanical information, such as elastic modulus, can be obtained through the analysis of the load-displacement behaviour alone with a coating of the material to be tested on a substrate made from different material. This makes it an ideal tool for our task. The technique has been used to assess the elastic and plastic properties of micron thick coatings on a range of substrates but there are limitations in measuring the properties of much thinner coatings, particularly when elastic properties are required[5, 6]. For coatings of a few hundred nanometres thickness it has been suggested that extrapolating the properties determined at a range of peak loads or indenter displacements to zero load/depth can be used to determine the coating only properties. With high quality, sharp indenters it is possible to assess coatings down to 100nm thick by this method [7]. This has been attempted in this study.

## 5.2 Experiment

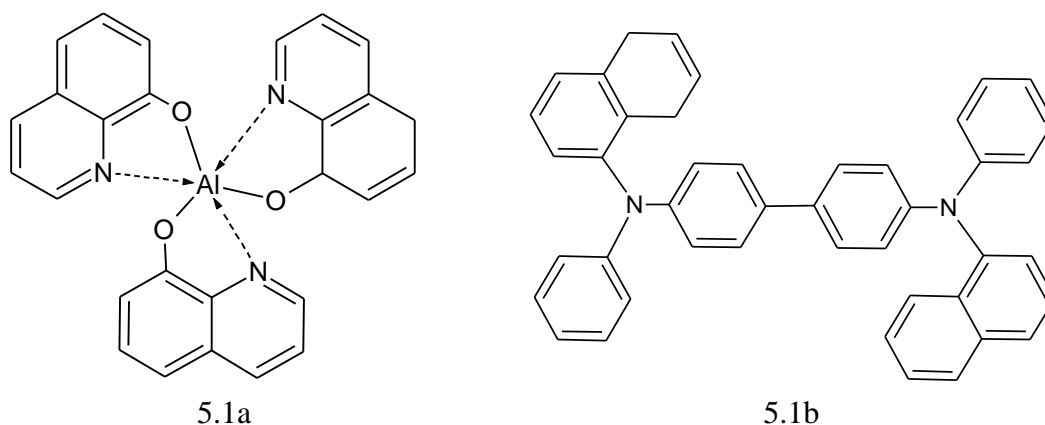


Fig. 5.1a, 5.1b Structure of Tris-(8-hydroxyquinoline) aluminum (Alq<sub>3</sub>) (5.1a) and N,N'-Bis(naphthalen-1-yl)-N,N'-bis(phenyl)benzidine (NPB) (5.1b).

Among all the small molecules used in OLEDs, Tris-(8-hydroxyquinoline) aluminum (Alq<sub>3</sub>) (fig. 5.1a) and N,N'-Bis(naphthalen-1-yl)-N,N'-bis(phenyl)benzidine (NPB) (fig. 5.1b) are two of the most popular materials. Because of the relatively high stabilities of the structures during operation and good electrical conductivities, they can be found in almost every OLED device structure. Therefore it is reasonable to expect that they would be used in the flexible OLED devices, too. So it is important to understand their elastic characteristic. In order to evaluate the effect of the substrate[8], two different kinds of substrates were used: polyethylene terephthalate (PET) supplied from DuPont Teijin Films and standard silicon wafers. All the substrates were cleaned in an ultrasonic bath with acetone, and then isopropanol for 5 minutes each. The substrates were then loaded into the Kurt J. Lesker Spectros II Deposition System. The tested materials were deposited under a vacuum of  $5 \times 10^{-7}$  mbar. Finally, the samples with 100 nm of Alq<sub>3</sub>, 200 nm of Alq<sub>3</sub> and 200 nm of NPB on three individual PET substrates and samples with 100 nm of Alq<sub>3</sub>, 100 nm of NPB on two silicon wafers were prepared respectively (see table 5.1).

Sample ID	Ia	Ib	Ic	IIa	IIb
Substrate material	PET	PET	PET	silicon wafer	silicon wafer
Substrate thickness / mm	<b>0.1</b>	<b>0.1</b>	<b>0.1</b>	<b>1</b>	<b>1</b>
Coating material	Alq <sub>3</sub>	Alq <sub>3</sub>	NPB	Alq <sub>3</sub>	NPB
Coating thickness / nm	<b>100</b>	<b>200</b>	<b>200</b>	<b>100</b>	<b>100</b>

Table 5.1 Samples investigated.

The Young's moduli of the samples were measured by standard nano-indentation techniques. For each material nano-indentation tests were performed under open loop, load and displacement control with maximum displacements ( $h_{max}$ ) from 10 nm to 1000 nm using a Hysitron Triboindenter fitted with a sharp Berkovich diamond indenter (tip end radius ~50 nm). In open loop control the indentation loading and unloading segments were controlled by timed ramps whereas in the other loading schemes feedback loops were used to ensure that the desired peak loads and displacements were achieved. The indentation systems frame stiffness and the diamond tip shape was carefully calibrated with a fused silica test sample, using the standard Oliver and Pharr method [9] as explained in chapter 3, before and after measurements with no change in either recorded. Nano-indentation load (P) vs. displacement (h) curves were then recorded for each indent and only those where evidence of plastic deformation was observed (i.e. the loading and unloading curves are different) were used in the analysis of Young's modulus by the Oliver and Pharr method [9]. The indenter displacement is in fact made up of two components: the plastic depth of the indent, or contact depth, and the elastic deflection of the surface at

the edge of the contact. The relationship between the contact depth ( $h_c$ ) and the maximum displacement ( $h_{max}$ ) can be determined from equation (5.1):

$$h_c = h_{max} - \beta \frac{P_{max}}{S} \quad (5.1)$$

where,  $P_{max}$  is the maximum loading, and  $\beta$  is a constant that depends on the shape of the indenter [10]. Empirical studies have shown that for a Berkovich indenter, the typical value of  $\beta$  is about 0.75.  $S$  is the unloading stiffness, which comes from the empirical equation:

$$S = \left. \frac{dP}{dh} \right|_{h=h_{max}} = mB(h_{max} - h_f)^{m-1} \quad (5.2)$$

where,  $m$  and  $B$  are fitting parameters, and  $h_f$  is the final displacement after completely unloading.

In this approach,  $S$ , the initial slope of the unloading curve, can finally be used to determine the reduced elastic modulus of the sample (effectively from the recovery of the elastic deflection of the surface) based upon the Sneddon flat punch solution [11] and the following equation:

$$E_r = \frac{1}{\alpha} \frac{\sqrt{\pi}}{2} \frac{S}{\sqrt{A}} \quad (5.3)$$

where,  $A$  is the contact area which can be deduced from  $h_c$  based upon an accurate knowledge of the tip end shape, and  $\alpha$  is a constant also depends on the geometry of the indenter ( $\alpha = 1.034$  for the Berkovich indenter)[10]

### ***5.3 Results and discussion***

Figure 5.2 shows one example of our load-displacement curve for the sample Ic obtained under open loop control at  $h_{max}=475$  nm. There is little difference to curves

obtained by the other control schemes (load or displacement control) showing that time dependent deformation (creep viscoelasticity) is not significant in this sample. Such load-unload experiment cycle was repeated at different indentation depth and each cycle contributed to one data point in the curve of reduced elastic modulus to the contact depth as shown in figure 5.3 to 5.7.

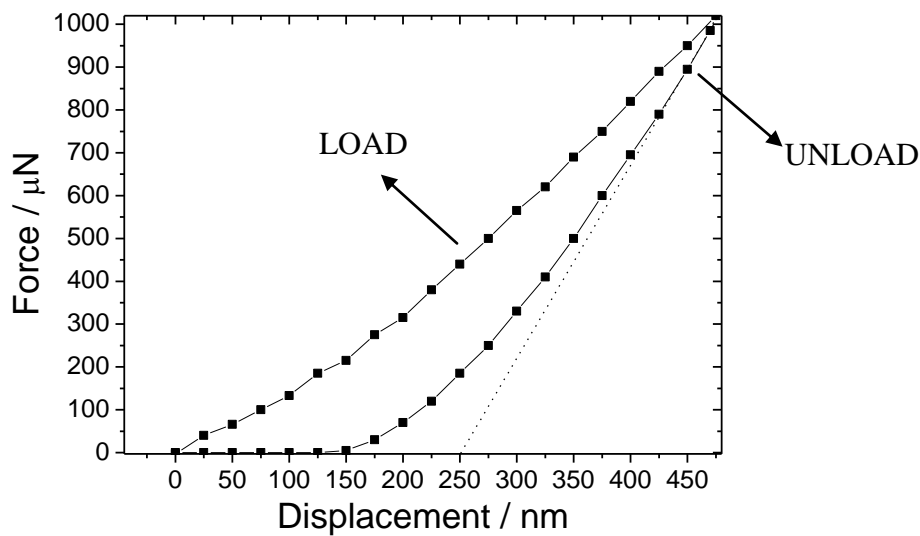


Fig. 5.2 Load-displacement curve for the 200 nm thick NPB coated on a PET film obtained under open loop control at maximum indenter displacement ( $h_{max}$ )=475 nm.

The load-unload curve with the maximum indenter displacement=475 nm shows the typical behaviour of a material undergoing a nanoindentation test. The initial slope ( $\sim 4.4 \mu\text{N}/\text{nm}$ ) of the unloading process is used to deduce the reduced elastic modulus of the coating material (in this case, NPB) at the specific  $h_c$ . There are a number of jumps (pop-ins) in the loading curve initially. These are most likely related to through-thickness cracking in the coating. Once the coating cracks it no longer supports as much load and the load support is transferred to the substrate – hence the behaviour is dominated by substrate deformation. The cracked coating will also have a lower effective Young's Modulus. The reason for the cracking is probably the

mismatch in properties between substrate and coating; a lower Young's modulus substrate material will expand elastically more than the coating for a given contact stress and as the coating tries to follow this expansion (because it is adhered to it) it is stretched beyond its fracture strain.

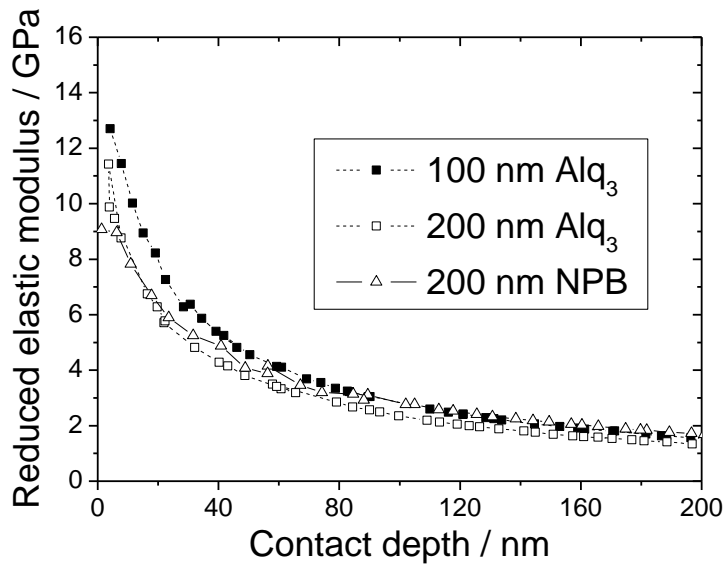


Fig. 5.3 Reduced elastic modulus against contact depth for the samples Ia, Ib and Ic.

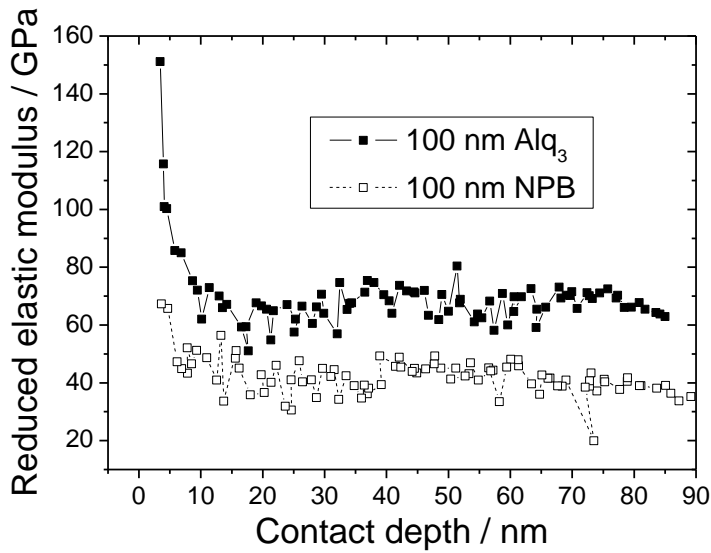


Fig. 5.4 Reduced elastic modulus against contact depth for the samples IIa and IIb.

The reduced elastic modulus of sample Ia, Ib and Ic against the contact depth are shown in figure 5.3. It is clear that the 100 nm Alq<sub>3</sub> coating has a greater stiffness than the 200 nm Alq<sub>3</sub> and NPB coatings. Since the coating thicknesses of all the samples is relatively smaller than the substrates all the values of reduced elastic modulus are expected to be affected by the substrate material. Therefore the value when the contact depth is extrapolated to zero should approximate the reduced elastic modulus of the coating layer deposited (ISO 14577-4 (2007)). From Figure 5.3, all the three samples have a Young's Modulus between 9 to 13 GPa when  $h_c$  approaches zero. Figure 5.4, however, shows a completely different result when using a silicon wafer as the substrate. The reduced elastic modulus of Alq<sub>3</sub> and NPB are over 160 GPa and 100 GPa respectively as  $h_c$  approaches zero which seems too large for a molecular film. If we omit the data when  $h_c < 5$  nm because of the effect of surface roughness, and do the extrapolation of the curve only between  $h_c=5$  and 10 nm as shown in figure 5.5, the reduced elastic modulus would become about 100 GPa (Alq<sub>3</sub>) and 60 GPa (NPB). All the different reduced Young's moduli obtained from different substrate materials and different analysis methods are listed in Table 5.2.

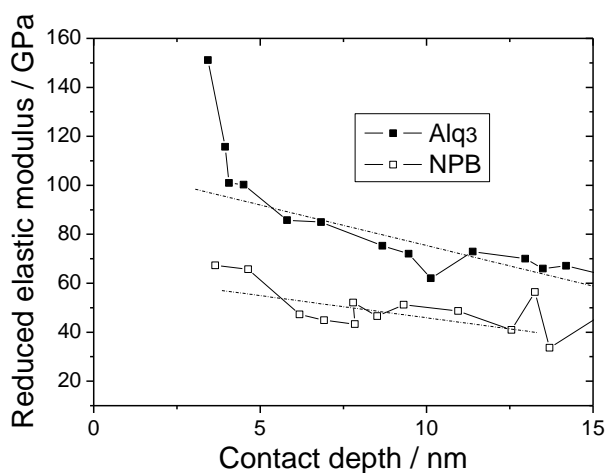


Fig. 5.5 Extrapolation to zero depth of the curve in figure 5.4 when considering the contact depth from 5 nm to 10 nm.



elastic modulus / GPa Data analysis method	Reduced Sample ID	Ia	Ib	Ic	IIa	IIb
	Extrapolation to 0		<b>13±3.25</b>	<b>12±3</b>	<b>9±2.25</b>	<b>100±11</b>
Series of springs - Equation (4)		<i>N/A</i>	<i>N/A</i>	<i>N/A</i>	<b>123.5±13.6</b>	<b>61±6.7</b>
Plateau in measured value as function of RID		<i>N/A</i>	<i>N/A</i>	<i>N/A</i>	<b>70±7.7</b>	<b>40±4.4</b>

Table 5.2 Reduced elastic moduli of samples determined by different methods.

The error is about 11% for the coatings on stiff substrates (IIa and IIb) and about 25% for the coating on soft substrates (Ia, Ib and Ic).

Material	Young's modulus (GPa)
PET	2.8-3.1
Aluminum	69
Glass	50-90
Gold	79
ITO	120
Steel	200
Diamond	1220

Table 5.3 Young's modulus of selected materials

There is a question about the validity of the data when  $h_c < 25\text{nm}$  since the accuracy of the measurement depends on the relative indentation depth (RID, i.e. the penetration divided by the coating thickness). This is due to the fact that for a blunt conical indenter there is a transition from spherical contact to conical contact behaviour – for the Berkovich indenter used here this transition occurs at  $h_c = \text{indenter radius}/4$ , i.e.

12nm and data at lower depths should be treated with caution as it has been shown that the contact modulus measured varies considerably with tip radius under spherical contact conditions [12]. The decrease in Modulus as  $h_c$  increases to 20nm could be due to this but may also be due to the fracture of the thin coating. It is not likely that the measured values in this depth range are due to an increasing contribution from the substrate since the plateau in Modulus at greater contact depths is not equal to the Young's Modulus of the substrate.

When a coating/substrate system is compressed between the indenter and sample support the measured reduced elastic modulus can be regarded as a combination of springs in series via, to a first approximation,

$$\frac{1}{E_{reduced}} = \frac{1}{E_{indenter}} + \frac{1}{E_{substrate}} + \frac{1}{E_{coating}} \quad (5.4)$$

Given the indenter properties ( $E=1141$  GPa) and silicon wafer substrate properties ( $E=130$  GPa) and the plateau values of measured modulus above  $h_c=20$ nm using the equation (5.4),  $Alq_3$  would have a Young's modulus of 124 GPa and NPB of 61 GPa which are similar to the values produced by extrapolation of the data to zero contact depth. This gives us some confidence in the measured values.

However, as mentioned previously, the ratio of the indenter tip end radius (IR) to the coating thickness (t) also plays an important role in nanoindentation data analysis [12].

For  $IR=t$ , the data can only be reliable when the penetration depth is equal to or greater than half the thickness of the coating material. For IR down to  $0.1t$ , the reliable data can extend to  $RID=0.05$ . If we use this concept to examine our experimental data, with the IR of the indenter about 50 nm, and the thickness of the small molecule coatings between 100 nm and 200 nm, the range would sit between  $IR=0.25t$  to  $0.5t$ . In such circumstances the critical RID to achieve reliable data would be 0.25 for the 100nm coating and 0.125 for the 200nm coating – i.e. the contact

depth of 25nm as identified above. The reduced elastic modulus of the samples is plotted against RID in figure 5.6 (Ia, Ib, Ic) and 5.7 (IIa, IIb). In both cases the reliability of the data at  $RID < 0.1$  used in extrapolation to zero contact depth for coating property assessment is questionable and the Young's Modulus data should be determined by different methods to ensure good accuracy.

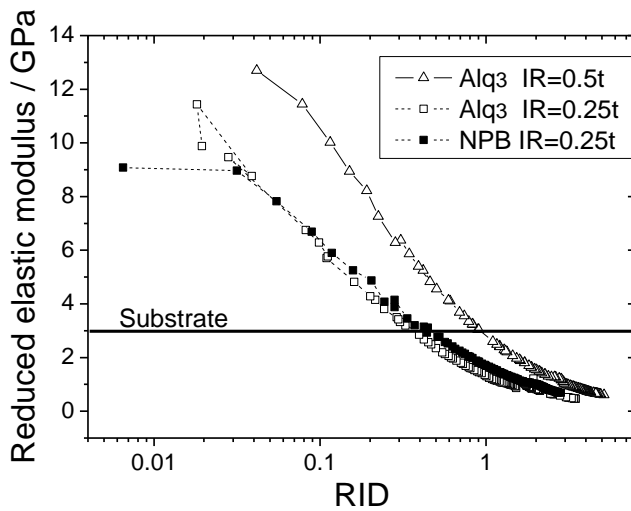


Fig. 5.6 Reduced elastic modulus against relative indentation depth (RID) for the samples Ia, Ib and Ic.

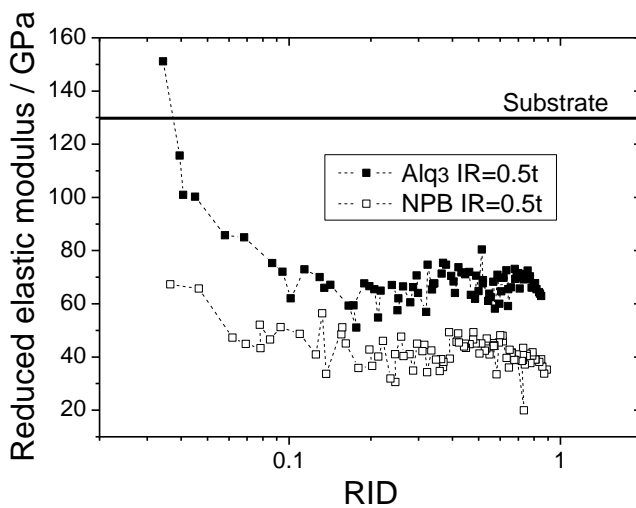


Fig. 5.7 Reduced elastic modulus against relative indentation depth (RID) for the samples IIa and IIb.

The fact that the measured Young's Modulus values do not converge to the Modulus of the substrate in either case shows that the indenter/coating/substrate system must be considered as a set of springs in series as described by equation (5.4). It is well known that the properties of a low modulus gasket will dominate the elastic properties of a bolted joint and in a similar manner a low modulus coating or substrate will dominate the properties of the system. The load jumps in the loading curve show that through-thickness fracture occurs at very low loads and the coating stiffness will depend on such cracking. The cracks are approximately parallel to the loading direction during indentation and are expected to have a relatively small effect on the Young's Modulus measured in this direction. However, the Young's Modulus necessary for OLED bending calculations is that in the direction perpendicular to these cracks which could be dramatically affected by cracking. The knowledge of the strain to failure in the film, as well as the knowledge of the modulus of uncracked material would be necessary to determine the bending resistance of these materials. In systems where the elastic properties of the coating are well known and the coating is deposited on a stiff and a polymer substrate (e.g. in the case of copper on sapphire and polyimide in Figure 5.8) the analysis methods used here only give the correct Young's Modulus for coatings on the stiff substrate. Thus for design purposes the properties of the films on a hard, stiff substrate should be used as these are more likely to be correct. The deposition of relatively stiff, stressed films on a polymeric substrate can lead to enhanced deformation of the substrate which cannot be accounted for by the simple, time-independent analysis that has been used here.

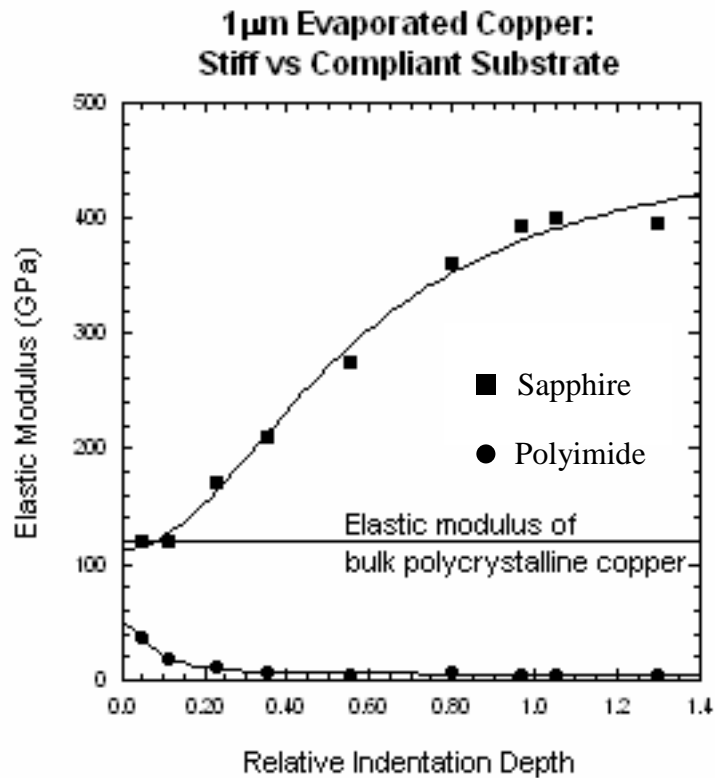


Fig. 5.8 Elastic modulus against relative indentation depth (RID) for the polycrystalline copper coated on softer (polyimide) and stiffer (sapphire) bases.

Given the different results from the two substrates (Table 5.2), we note first that the density of the thin-film, or the way it is grown might be different when deposited onto different materials, and both the film density and the structure of the aggregation can alter the elastic response of the thin-film. The mobility of added species on polymer substrates is often low when compared to materials like silicon leading to the formation of less dense coatings with lower elastic moduli. Thus the properties on silicon may not be totally correct for the films deposited on PET but are a better first approximation to the real properties than the values measured on the PET substrate unless a better model is developed to account for substrate deformation during indentation.

## ***5.4 Summary***

For such a thin coating on a compliant substrate (i.e. the samples Ia,b,c) it is difficult to completely filter out the effect of the substrate on the measurement and there may be considerable scatter in the extrapolated modulus due to the quality of the data available for extrapolation. Figure 5.6 actually show a monotonic increase in Reduced Modulus with relative indentation depth and there is considerable agreement between the samples with different coatings but the same thickness. An increase in coating thickness results in an increase in measured Reduced Modulus at a given depth which implies that differing substrate contributions have been recorded. However, on the silicon substrate there is much greater discrimination between the properties of the individual coatings as the results are dominated by the coatings rather than the substrate material. A group in Arizona State University recently cited my work and had a different opinion about the stiffness of Alq<sub>3</sub>[13]. However their results suggested that a thickness > 20 nm Alq<sub>3</sub> film has the Young's modulus of 1 GPa, which is even much softer than PET according to table 5.3, and makes it hard to believe. A better method to probe the elastic property of the OLED thinfilms is still to be developed.

To conclude, in this work the reduced elastic modulus of the Alq<sub>3</sub> and NPB thin-films used in the OLED devices are measured with different substrates using the nanoindentation method developed by Oliver and Pharr. Different methods of analysis have been applied. When measured on silicon, the reduced elastic modulus of Alq<sub>3</sub> and NPB are in the range of 60 to 120 GPa, which is similar to values obtained for amorphous carbonaceous coatings and heavily cross-linked materials where density is high. When the film is deposited on the PET film, however, the Young's modulus is much smaller (~13 GPa) due to changes in film density and structure.

## 5.5 References

- [1] S. K. Park, J. I. Han, D. G. Moon, and W. K. Kim, "Mechanical stability of externally deformed indium-tin-oxide films on polymer substrates," *Japanese Journal of Applied Physics Part 1-Regular Papers Short Notes & Review Papers*, vol. 42, pp. 623-629, Feb 2003.
- [2] G. P. Crawford, "flexible flat panel displays," in *Wiley-SID Series in Display Technology*, A. C. Lowe, Ed. Brown University, USA: John Wiley & Sons, Ltd, 2005, pp. 99-120.
- [3] C.-J. Chiang, C. Winscom, S. Bull, and A. Monkman, "Mechanical modeling of flexible OLED devices," *Organic Electronics*, vol. 10, pp. 1268-1274, 2009.
- [4] S. J. Bull, "Nanoindentation of coatings," *J. Phys. D: Appl. Phys.*, vol. 38, pp. R393-R413, 2005.
- [5] A. M. Korsunsky, M. R. McGurk, S. J. Bull, and T. F. Page, "On the hardness of coated systems," *Surface & Coatings Technology*, vol. 99, pp. 171-183, Feb 1998.
- [6] J. Chen and S. J. Bull, "A critical examination of the relationship between plastic deformation zone size and Young's modulus to hardness ratio in indentation testing," *Journal of Materials Research*, vol. 21, pp. 2617-2627, Oct 2006.
- [7] J. Chen and S. J. Bull, "On the factors affecting the critical indenter penetration for measurement of coating hardness," *Vacuum*, vol. 83, pp. 911-920, Feb 2009.
- [8] A. A. Pelegri and X. Huang, "Nanoindentation on soft film/hard substrate and hard film/soft substrate material systems with finite element analysis," *Composites Science and Technology*, vol. 68, pp. 147-155, 2008.
- [9] W. C. Oliver and G. M. Pharr, "An improved technique for determining hardness and elastic modulus using load and displacement sensing indentation experiments," *Journal of Materials Research*, vol. 7, pp. 1564-1583, Jun 1992.
- [10] G. M. Pharr, "Measurement of mechanical properties by ultra-low load indentation," *Materials Science and Engineering A*, vol. 253, pp. 151-159, 1998.
- [11] I. N. Sneddon, "The relation between load and penetration in the axisymmetric boussinesq problem for a punch of arbitrary profile," *International Journal of Engineering Science*, vol. 3, pp. 47-57, 1965.
- [12] A. M. Korsunsky and A. Constantinescu, "The influence of indenter bluntness on the apparent contact stiffness of thin coatings," *Thin Solid Films*, vol. 517, pp. 4835-4844, 2009.
- [13] J. M. Torres, N. Bakken, C. M. Stafford, J. A. Li, and B. D. Vogt, "Thickness dependence of the elastic modulus of tris(8-hydroxyquinolino)aluminium," *Soft Matter*, vol. 6, pp. 5783-5788, 2010

## ***Chapter 6***

### ***Mechanical modeling of flexible OLED devices***

In the Previous chapter, the Young's modulus of the commonly used OLED small molecules Alq<sub>3</sub> and NPB were investigated. This data will now be used to find out the stress in a FOLED device. The work has been published in **Organic Electronics**

Volume 11, Issue 11, November 2010, Pages 1870-1875

And oral presented at **7rd International Conference on Electroluminescence of**

**Molecular Materials and Related Phenomena**, Or 7a-2, 2008.

### ***6.1 Background***

Recently, glass substrate based OLED devices have been improved to achieve commercial application standard in most respects. With reported device lifetimes longer than 200 khr [1] and efficiencies larger than 100 lm/W [2], OLEDs appear increasingly more competitive with rivals such as backlit LCDs in displays, and inorganic LEDs or fluorescent lamps in lighting. To be cost competitive, the move to flexible lightweight supports is seen to be mandatory as far as OLED Solid State Lighting (SSL) applications are concerned [3]. It would open the way to a roll-to-roll



manufacturing processes, allow cost effective distribution and installation of lighting panel products, and if conformable would offer unique features to the consumer as a surface distributed source. However, there are still a number of problems to be solved. One of these problems concerns the material of the transparent anode. For two decades, indium-tin-oxide (ITO) has been commonly used as the highly conductive, transparent, and stable anode for both OLED and PLED devices on rigid supports. However, on the flexible supports, the brittleness of ITO becomes a major issue. Another problem is the permeation of oxygen and water vapour through the plastic substrate; both cause rapid deterioration of OLED devices according to previous degradation studies [4,5]. One solution for the latter issue is to insert one or more barrier layers involving  $\text{SiO}_x$  [6] between the substrate and ITO, to block the oxygen and water vapour from the sensitive thin organic layers of the device. Although researchers are trying hard to find a replacement material for the ITO, this material is best understood in OLED devices, and it would be most convenient if this component remained unchanged. For this to remain so, the mechanical forces of bending the device must be explored to understand the stress developed in the ITO layer with a view to reducing it by some means. The intriguing question is: if by inserting a buffer layer (BL), can an adequate solution to both issues at the same time be achieved?

## ***6.2 Theory***

In the chapter 2, the stress in a rectangular bar has been deduced. However the FOLED device usually consists of more than 4 layers: the substrate, the anode, the organic layer, and the cathode, therefore the theory needs to be extended further. We

should begin from the two-layered structure, say, the polyethylene terephthalate (PET) substrate topped with ITO anode. Imagine a 175  $\mu\text{m}$  PET substrate covered with a 100 nm ITO thin-film to have a structure somewhat analogous to a leaf spring, with 1750 soft leafs and 1 hard leaf, each 100nm thick and connected in parallel. In contrast to the leaf spring, however, here the adjacent surfaces of neighbouring leafs are firmly bound to one another. When the structure is bent so that the uppermost surface of the thin layer is concave, it is reasonable to assume that there will be one “leaf” out of the 1751, which maintains its original length, and all others laid above it are stretched while those below it are compressed. The one with its original length is called the neutral layer (NL). The position of this layer is crucial because the strain in any of these springs is proportional to the distance from itself to the neutral layer. This will be deduced later.

To determine the position of the NL in a multi-layer structure, others such as Kim [7] and Hsueh [8] have put forward analytical solutions. In these studies, both the position of the NL and the stress in the layers are considered to be unknown parameters, and are solved with equations of equilibrium of static force and torque in the cross-section. In the work presented here, the method introduced enables us to consider the multilayer bending situation, visually. It is not a new concept since engineers have routinely used it to deal with the stress problems that arise when building with multi-material composite beams [9]. However, it is equally applicable to the realm of plastic electronics, where the nano-architectures involved comprise multiple thin layers on a much thicker flexible support, a particular example of which would be a flexible OLED device.

For the longitudinal stress in a plain film being bent, the stress is given by:

$$\sigma = E' \varepsilon$$

$$E' = \frac{E}{1-\nu^2} \quad (6.1)$$

where the Young's Modulus of the film material is  $E$ ,  $\nu$  is the Poisson's ratio,  $E'$  is the reduced elastic modulus and the strain of the film is  $\varepsilon$ . This strain is defined by:

$$\varepsilon = \frac{\Delta l}{l} \quad (6.2)$$

where  $l$  is the original unbent length, and  $\Delta l$  is the change of length after bending.

Although these thin-films are not real springs, the strain caused by bending is only about 0.01 even when the radius is 10 mm. This means the higher order terms are negligible and Hooke's Law is still valid. When an arbitrary segment of a

homogeneous film with a symmetric cross-section is analysed, the NL should be right at the centre of the film.

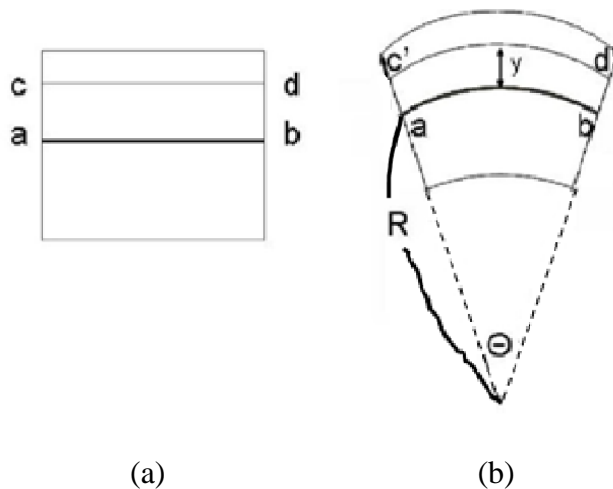


Fig. 6.1 One segment of a single-material beam before (a) and after (b) bending.

Layer  $ab$  is the Neutral Layer; Layer  $cd, c'd'$  is the same layer before and after bending with radius  $R$ .

Assume the layer denoted by  $\overline{ab}$  in figure 6.1a is the NL, and by definition its length remains unchanged on bending to an extent where  $R$  defines the radius of curvature experienced by the NL. Setting the length of  $\overline{ab}$  to be  $l$ . Now consider the strain of another layer in the film, say,  $\overline{cd}$ , when the radius of curvature at the NL ( $\overline{ab}$ ) is  $R$ . Before bending (figure 6.1a):

$$\overline{cd} = \overline{ab} = l \quad (6.3)$$

whilst after bending (figure 6.1b) the new length of  $\overline{cd}$  becomes  $\overline{c'd'}$ , so that

$$\overline{ab} = l = R\theta \quad (6.4)$$

$$\overline{c'd'} = l + \Delta l = (R + y)\theta \quad (6.5)$$

where  $y$  is the distance from the layer to the NL. The strain in the  $cd$  element at this distance from the NL thus becomes:

$$\varepsilon(y) = \frac{\Delta l}{l} = \frac{y}{R} \quad (6.6)$$

Therefore the stress in any layer in a film with its distance from the NL being  $y$  is

$$\sigma(y) = \frac{E'y}{R} \quad (6.7)$$

The total bending moment  $M$  at one end of the segment is

$$M = \int_{-c}^{h-c} \sigma wy dy$$

$$\begin{aligned}
&= \frac{E'}{R} \int_{-c}^{h-c} w y^2 dy \\
&= \frac{E'}{R} I_x
\end{aligned} \tag{6.8}$$

where  $h$  is the thickness of the film,  $C$  is the displacement from the bottom of the film to the NL,  $w$  is the width of the cross section and  $I_x$  is the second moment of area of the cross section. So we have the following equation to describe the stress developed in the layer as a result of bending completely:

$$\frac{\sigma}{y} = \frac{E'}{R} = \frac{M}{I_x} \tag{6.9}$$

From the above, the most critical property is the position of the NL. In a single material, the position of NL is easy to determine. It is just at the centroidal axis of the cross section, so the distance from the layer of interest to the NL,  $y$ , will be known. When the architecture comprises two or more layers of different materials, for example ITO on a PET substrate, slightly more effort is required.

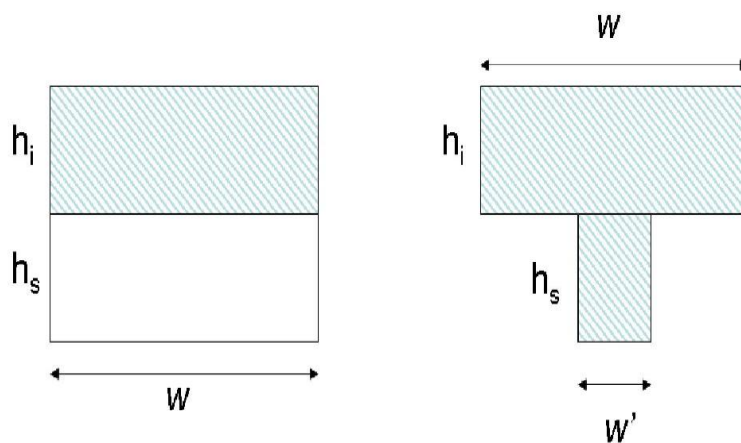


Fig. 6.2 Cross-section (a) and effective cross-section according to the top layer (b) of a two-material composite beam. The thickness of each layers are  $h_i$  and  $h_s$ .

Figure 6.2a shows the cross-section of the typical ITO coated PET substrate where  $h_s$  is the thickness of the substrate, and  $h_i$  is the thickness of ITO. Assume both layers are with the same width  $w$  and different Young's Modulus:  $E_s$  and  $E_i$ . The total bending moment is

$$\begin{aligned}
 M &= \int \sigma w y dy \\
 &= \frac{E'_s}{R} \int_{-c}^{h_s-c} \sigma w y dy + \frac{E'_i}{R} \int_{h_s-c}^{h_s-c+h_i} w y^2 dy \\
 &= \frac{E'_s}{R} I_x^s + \frac{E'_i}{R} I_x^i \\
 &= \frac{E'_i}{R} \left( \frac{E'_s}{E'_i} I_x^s + I_x^i \right) \\
 &\equiv \frac{E'_i}{R} I_x^{effective} \tag{6.10}
 \end{aligned}$$

$C$  is the position of the NL from the bottom of the substrate. The position of  $C$  is chosen at the  $y=0$  axis in the integration to determine the second moment of area instead of the conventional choice of the centroidal axis of the individual cross section. Formally, it is determined by equating the net force acting on the cross section under bending, to zero as follows:

$$0 = \frac{E'_s}{R} \int_{-c}^{h_s-c} w y dy + \frac{E'_i}{R} \int_{h_s-c}^{h_s-c+h_i} w y dy \tag{6.11}$$

Equation (6.10) shows that the total bending moment  $M$  of an ITO/PET composite film is the same as the pure ITO film with the effective cross section  $I_x^{effective}$ .

Compared with equation (6.8), it can be seen that the effective cross section is really the original cross section of ITO plus the cross section of PET with the new width  $w'$  given by:

$$W' = \frac{E'_s}{E'_i} W \quad (6.12)$$

Therefore, in the case of longitudinal stress, an ITO/PET composite film (as shown in figure 6.2a) is identical to the pure ITO film (as shown in figure 6.2b). This greatly reduces the effort of solving the position of the NL from equation (6.11) to simply determining the centroidal axis of the effective cross section as if it were made from a single material. When dealing with structures of more than two layers, with each layer having a different Young's modulus, the task of determining the position of the NL using the equation (6.11) becomes even more complicated. However the method we used here requires only the calculation of the effective cross section by determining  $w'$  of each layer, using the reduced elastic modulus of the layer of interest as the denominator in equation (6.12). Once the equivalent cross section is determined, with the assumption that all the layers are now made from an identical material to the layer of interest, the NL is targeted at the position of centroidal axis of this effective cross section, and the stress in the layer of interest is just a factor times its distance from the NL in the effective cross section: the calculation has transformed the multi-material composite film into a single material film made solely from the layer under investigation.

### ***6.3 Results and Discussion***

Due to the poor performance of plastic substrates with respect to permeation of water and oxygen, mentioned earlier, one or more extra barrier layers would usually be inserted between the ITO layer and the PET substrate. The question is: is it possible that a single additional layer could both reduce the stress in the ITO to give it an extra relief when bending and provide an adequate oxygen/water barrier at the same time?

Glass, for example, has a permeation rate of oxygen and water vapour lower than the detection limit [10] and is therefore a good candidate for the protecting layer. Typically, an oxygen permeation rate for soda lime float glass is given as  $<10^{-15}$  ( $\text{cm}^3$  STP)  $\text{cm}^{-2} \text{mm}^{-1} \text{s}^{-1} (\text{mm Hg})^{-1}$ . Applying the conventional assumption that permeability is inversely proportional to the layer thickness, and proportional to pressure difference across the layer, the permeability for a 1 mil (25 $\mu\text{m}$ ) film thickness, and a 1 atm. pressure difference, is estimated to be  $<2.6 \times 10^{-2} \text{cm}^3 \text{m}^{-2} \text{day}^{-1}$ , in the conventionally adopted units for discussing OLED device performance. By comparison, both oxygen and water permeation rates in 25 $\mu\text{m}$  thick films of  $\text{SiO}_x$  produced by plasma-enhanced chemical vapour deposition (PECVD) have been measured, and are  $8 \times 10^{-2} \text{cm}^3 \text{m}^{-2} \text{day}^{-1}$  at 1 atm pressure difference and  $0.5 \text{g m}^{-2} \text{day}^{-1}$  at  $>90\%$  relative humidity, respectively [11]. The upper limits for adequate OLED device performance are currently thought to be on the order of  $10^{-3} \text{cm}^3 \text{m}^{-2} \text{day}^{-1}$  (oxygen) and  $10^{-5} \text{g m}^{-2} \text{day}^{-1}$  (water), where material composition, layer thickness, and pressure difference are variables to achieve these values. Therefore supports consisting solely of glass would be effective enough as a barrier to moisture



and oxygen, but inevitably must also be thick enough to provide the physical robustness to support the area of the display as a whole. By adding the thin-glass film to the ITO/PET composite, the latter might protect the brittleness of the thin-glass when being bent, and the former could provide the barrier that the ITO/PET lacks of. Furthermore, the thin-glass might even help to reduce the stress in the ITO layer, which will be explored as the first example.

	Young's modulus (GPa)	Reduced elastic modulus (GPa)
Al	70	78
OLED	N/A	12
ITO	120	120
BL	N/A	6-70
PET	4	5
Glass	70	74

Table 6.1 The value of Young's modulus and reduced elastic modulus used in the simulation.

The reduced elastic modulus of ITO, glass, and PET film are assumed to be 120 GPa [12], 74 GPa, and 5 GPa, respectively, as in table 6.1. In addition, the yield stress of ITO is 1.2 GPa, and very rapid increase of sheet resistance changes were observed to occur for the strain of 2% or more, which equate to the stress of 2.4 GPa or more. If

the total thickness of glass plus PET composite substrate is kept constant at 175  $\mu\text{m}$ , with a typical ITO thickness of 100 nm coated on the glass side and the whole composite subjected to a bend radius of 1 cm, then from equation (6.7) the thicknesses of glass and PET optimized by simulation are 35  $\mu\text{m}$  and 140  $\mu\text{m}$ , respectively, as shown in figure 6.3 (black solid circle). This structure would reduce the stress in ITO from the plain PET substrate – and, indeed, also a plain glass substrate - by a factor of 2.5. On the contrary, if the ITO is coated on the PET side as shown in the red open square curve, the stress in the ITO will even be larger than without the glass buffer layer and comfortably (or uncomfortably) surpass the yield stress for glass thickness between 10 – 140  $\mu\text{m}$ .

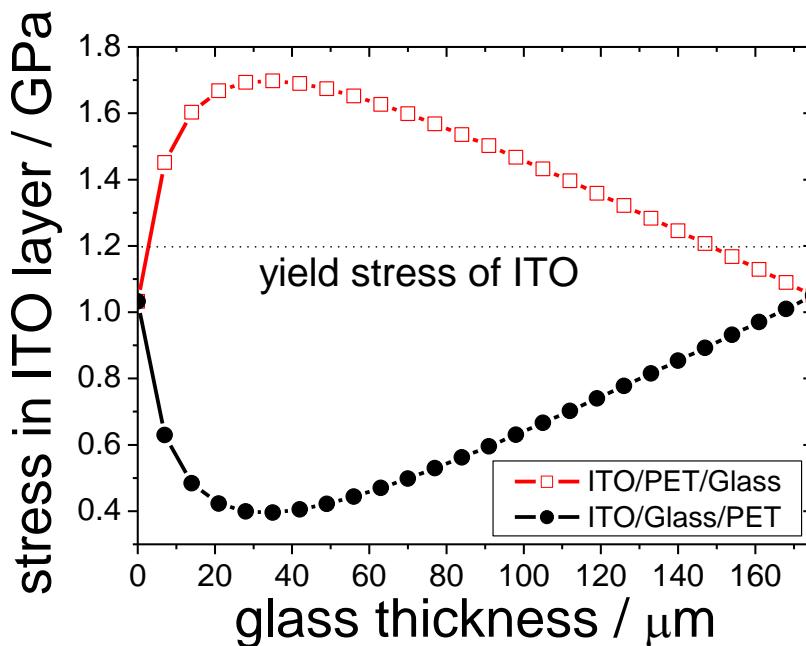


Fig. 6.3 The stress in ITO against the thickness of glass buffer layer with the fixed “glass/PET” composite substrate thickness of 175  $\mu\text{m}$ . The bending radius is 10 mm.

The second case study is the practical five-layered FOLED device.

The five layers structure: PET (100  $\mu\text{m}$ )/Buffer (x)/ITO (100 nm)/OLED (100 nm)/Aluminium (100 nm) is simulated with different values of reduced elastic modulus of the buffer layer (BL) and different thicknesses, x. The extension to accommodate the multiple thin layers in this case is particularly straightforward. The combined thickness of the thin layer stack is nearly three orders of magnitude less than that of the support, so the position of the neutral layer is determined almost exclusively by the composition of the thicker support. The stress in each of the thin layers is then determined by the reduced elastic modulus of the thin layer, the distance from the neutral plane to the surface on which the thin layer is coated and the bend radius, just as for the single thin layer case. The reduced elastic modulus of each layer can be referred in table 6.1. The value of the OLED is set to be 12 GPa as the obtained in the previous chapter for the sample of Alq<sub>3</sub> and NPB coated on the PET film. Although it was found, in the previous chapter, that the Young's moduli are different when the OLED is coating on the silicon substrate, but the simulation here only deals with the stress difference with and without buffer layer, so the absolute value of the Young's moduli of the OLED material won't affect the analysis.

Assuming the bending radius is 15 mm, the stress in ITO against the thickness of BL is shown in figure 6.4. This shows a series of different buffer layer moduli, in the whole device structure. In contrast to figure 6.3, the PET layer now has a constant thickness and the buffer thickness is increased from zero. As the buffer material modulus increases, values in the range 14-70 GPa exhibit minima in ITO stress at a thicknesses of 15- 20% of the PET layer. When the reduced elastic modulus of the BL is smaller than 14 GPa, the ITO stress is increased.

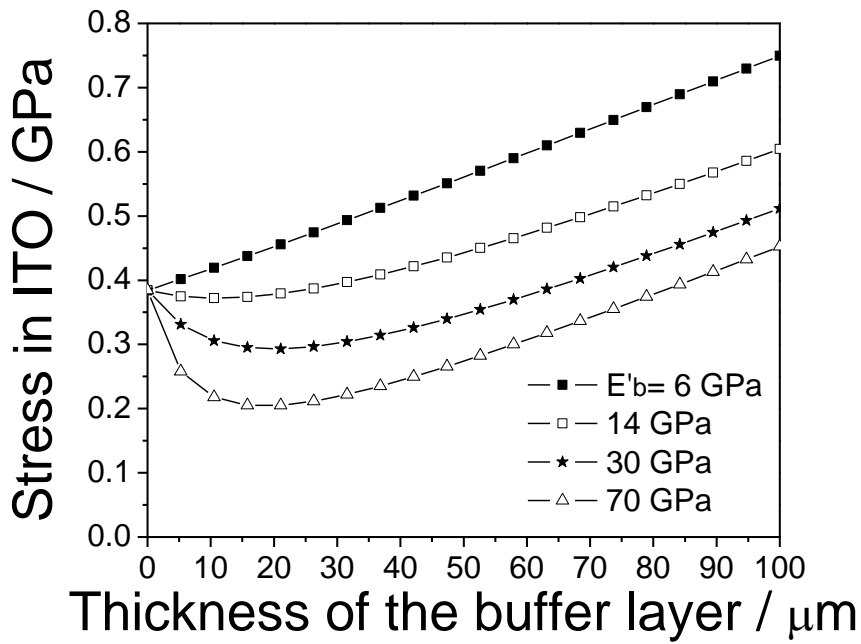


Fig. 6.4 The stress in ITO against the thickness of buffer layer with different buffer layer Young's modulus in the five-layers structure:

PET(100 $\mu\text{m}$ )/Buffer(0-100 $\mu\text{m}$ )/ITO(100nm)/OLED(100nm)/Aluminium(100nm).

The bending radius is 15 mm.

For a BL modulus of 70 GPa, the stress shows the maximum reduction -about 50% - for a thickness of 20  $\mu\text{m}$ . However, a larger stress occurs when it is thicker than 70  $\mu\text{m}$ . This is the result of the competition between the changing of the NL position and the distance of ITO layer from NL as mentioned before. The stress in ITO against the bending radius with BL thickness of 20  $\mu\text{m}$  and 100  $\mu\text{m}$  is shown in figure 6.5 and 6.6.

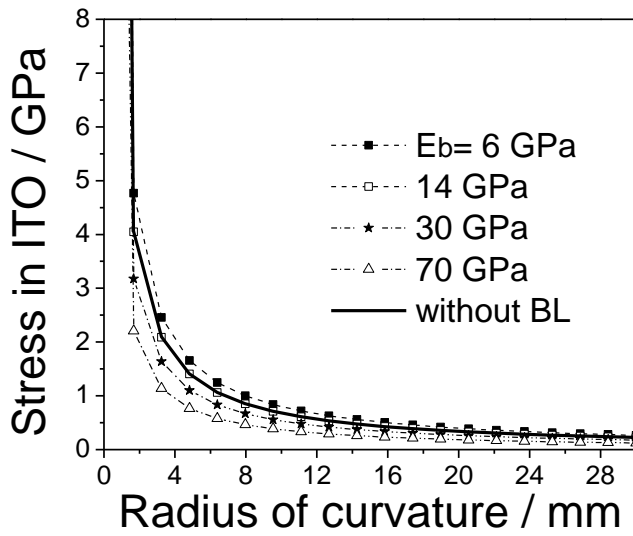


Fig. 6.5 The stress in ITO against the device bending radius with different buffer layer

Young's modulus in the five-layers structure:

PET(100µm)/Buffer(20µm)/ITO(100nm)/OLED(100nm)/Aluminium(100nm).

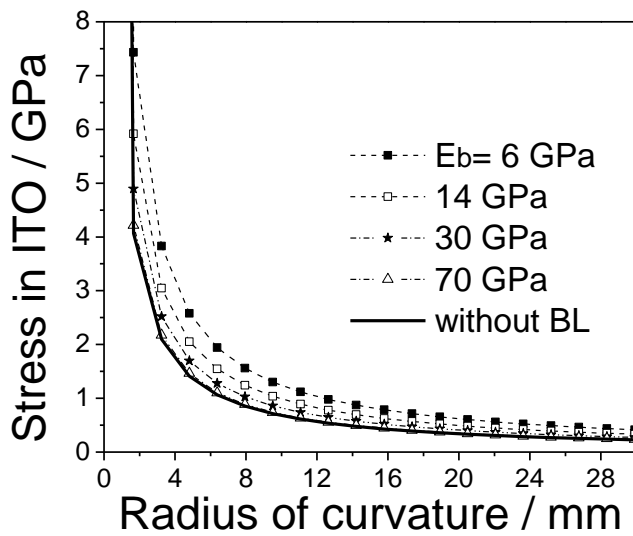


Fig. 6.6 The stress in ITO against the device bending radius with different buffer layer

Young's modulus in the five-layers structure:

PET(100µm)/Buffer(100µm)/ITO(100nm)/OLED(100nm)/Aluminium(100nm).

This simulation presents a very interesting result. For the former thickness, it seems that the larger the Young's modulus, the better. But the effect will saturate eventually. However, the latter suggests that when the BL is as thick as the PET layer (100  $\mu\text{m}$ ), the stress in ITO will never be reduced no matter what material is chosen.

## **6.4 Summary**

An alternative approach to calculate the stress developed in a thin film multi-layer has been adopted. With this method, the position of the NL can be determined and a concept of visualising changes in stress as the structural architecture is fine-tuned has emerged. A plastic/glass composite substrate with the thickness of 140  $\mu\text{m}$  and 35  $\mu\text{m}$  respectively, acting to provide a flexible barrier to oxygen and water vapour, has been predicted to reduce the stress in ITO deposited on the glass surface by a factor of 2.5, compared with 175  $\mu\text{m}$  of either glass or PET on its own. The yield strength of ITO (the limit beyond which material deformation is irreversible) corresponding to a failure strain of *ca.*1%, is 1.2GPa [15]. The support composition above can be shown to adequately protect a thin ITO layer to bend radii significantly less than 1cm; indeed, the stress in the ITO layer is predicted to reach its yield strength value at a bend radius as low as 3.3mm. This prediction is particularly interesting, since currently, flexible glass as thin as 50 $\mu\text{m}$  has been achieved, and the prospect of 30 $\mu\text{m}$  is reported to be within reach [16]. The discussion of breaking stress in the flexible glass itself is beyond the scope of this thesis, but will be disclosed in the forthcoming patent literature [17]. As a guide, flexible glass with a thickness in the region of 30 $\mu\text{m}$

exhibits a breaking stress of *ca.*0.15GPa. It is estimated that a composite glass/PET support of 175 $\mu$ m total thickness could withstand a bend radius of 1.2 cm for a range of 10-40 $\mu$ m glass thickness without breakage.

Finally, a practical five-layer OLED device structure has been simulated using the reduced elastic modulus values for NPD and Alq<sub>3</sub> measured in chapter 5. It shows that the choice of the BL material's modulus, and its thickness relative to that of the underlying PET, are crucial in reducing the stress in ITO. For BL thicknesses equal to that of the PET, the BL is unable to decrease the ITO stress, regardless of its modulus. One has to bear in mind that all the materials in this simulation are assumed to be elastic. The mechanism of creep (changing of strain under fixed applied stress) and stress relaxation (changing of stress under fixed applied strain) is omitted. The mechanism of cracking is also not considered. There will be some cracks generated initially on each film during their fabrication, and the initial pattern of these cracks would not be expected to be the same for every sample. Nevertheless, reducing the stress in the most brittle layer should still slow down or prevent cracks from migrating further, thereby extending the device lifetime.

Practically, for commercial FOLED devices, it is generally necessary to cover the device with an extra encapsulation layer. With a careful choice of the thickness and elastic property of this encapsulating layer, it is possible to further reduce the distance between NL and the brittle anode layer thus diminishing the stress even to zero. However, the problem of deformation or delamination between layers, either due to thermal stress or bending, may become the dominant concern in the FOLED device degradation.

The next chapter presents a study of how the bending stress affects the EL performance of the FOLED devices.

## 6.5 References

- [1] M. Hack and V. Adamovich, *7th International Conference on Electroluminescence of Molecular Materials and Related Phenomena* (2008).
- [2] S. Forrest, *7th International Conference on Electroluminescence of Molecular Materials and Related Phenomena* (2008).
- [3] "Organic light emitting diodes for general illumination" ed. M.Stolka, *OIDA* (2002), P52.
- [4] H. Aziz and G. Xu, *Synthetic Metals*, 80 (1996), 7.
- [5] S. Gardonio, L. Gregoratti, P. Melpignano, L. Aballe, V. Biondo, R. Zamboni, M. Murgia, S. Caria, and M. Kiskinova, *Organic Electronics*, 8 (2007), 37.
- [6] D. G. Howells, B.M. Henry, Y. Leterrier, J.-A.E. Månson, J. Madocks, and H.E. Assender, *Surface and Coatings Technology*, 202 (2008), 3529.
- [7] S. K. Park, Jeong I. Han, D. G. Moon, and W. K. Kim, *Jpn. J. Appl. Phys.*, 42 (2003), 623.
- [8] C. Hsueh, *J. Appl. Phys.*, 91 (2002), 9652.
- [9] J. Case and A. H. Chilver, *Strength of Materials and Structures-An introduction to the mechanics of solids and structures* Second edn (Edward Arnold, 1971), pp. 189-201.
- [10] A. Plichta, A. Weber, and A. Habeck, *Flexible Electronics-Materials and Device Technology*, 769 (2003), 273.
- [11] *Flexible Flat Panel Displays* ed. G.P.Crawford Joh Wiley, Chichester, 2005, Ch. 4 "Barrier Layer Technology for Flexible Displays" G.L.Graff, P.E.Burrows, R.E.Williford and R.F.Praino, pp 57-77.
- [12] Y. Leterrier, L. Médico, F. Demarco, J.-A.E. Månson, U. Betz, F. Escolà, M. Kharrazi Olsson, and F. Atamny, *Thin Solid Films*, 460 (2004), 156.
- [13] W. C. Oliver, G. M. Pharr, *J. Mater. Res.*, Vol. 7, No.6 (1992), 1564.
- [14] A. A. Pelegri, X. Huang, *Composites Science and Technology*, 68 (2008), 147.
- [15] *Flexible Flat Panel Displays* ed. G.P.Crawford Joh Wiley, Chichester, 2005, Ch. 6 "Mechanics of ITO on Plastic Substrates for Flexible Displays" P.C.P. Bouten, P.J.Sikkeveer, Y.Leterrier pp 99-120.
- [16] Methods for the production of flexible glass are disclosed in the following patents: WO 2005/110741 and WO 2008/093153.
- [17] Patent applied for: assignee Eastman Kodak Company, Rochester, New York.



## ***Chapter 7***

### ***Electroluminescence characterization of FOLED devices under two types of external stresses caused by bending***

In the previous chapter, the stress in ITO of the multi-layered FOLED device was simulated. Here in this chapter, the conventional bottom-emitting FOLED devices were fabricated and the EL performance was measured when the external stress was applied to the device. This work has been published in Organic Electronics **Volume 11, Issue 11, November 2010, Pages 1870-1875**

#### ***7.1 Background***

Multilayer thin-film organic light emitting diodes (OLEDs), since being introduced in 1987 by VanSlyke and Tang[1], have reached the commercial stage in recent years as more and more gadgets, notably Google's smart phone Nexus One, become equipped with a delicate OLED display panel. Moreover, OLED technology, as an eco-friendly method of generating light, has attracted the interest of many big lighting companies such as Thorn, Philips, Osram, and General Electronics in the last few years. These trends indicate that the technology of putting OLED and electrical circuits onto a glass substrate is getting steadily more mature. Meanwhile, however, liquid crystal

display (LCD) technology, OLED's biggest rival and currently the most popular display technology, has advanced. The viewing angle has improved by various technologies such as in-plane switching[2] (IPS) and multi-domain vertical alignment[3] (MVA), and the power consumption lowered by using light emitting diodes (LEDs) as backlight source, so that the advantages that OLEDs once held have been gradually eroded. Nevertheless, the potential to be transparent or flexible still allows OLED technology distinguish itself from the others. So far, the most prominent manufacturers incorporating OLEDs, such as Sony and Samsung, have demonstrated their flexible OLED (FOLED) display prototypes at some industrial exhibitions. Whilst their examples may demonstrate that the OLED device can still emit light while being bent, the extent to which the luminescence efficiency and brightness would be affected because of bending, or how tightly it could be bent, has not been reported. The answer to both these questions constitutes the first step in evaluating the possibility of whether an OLED device could be made flexible.

The stress within the OLED thin-films of a flexible OLED (FOLED) device is mainly from three sources: residual stress, thermal stress, and the external stress. Residual stress is from the deposition process no matter it is thermal evaporated, spin-coated, or printed. It is unavoidable for a soft substrate based OLED device[4]. Thermal stress comes from the different coefficients of thermal expansion of the adjacent layers when the environmental temperature changes[5]. External stress comes from the application of an external bending moment[6]. For example, when the FOLED device is bent, strain is introduced in the thin-films and stress is generated. Stress can make each film to crack or buckle when the deformation exceeds what it can bear. In a conventional multi-layer OLED device structure, the indium-tin-oxide (ITO) is the most vulnerable film with the Young's Modulus of 120 GPa and yield stress of 1.2

GPa. The theoretical calculation of the stress in ITO of the five-layered stack structure was simulated in the previous chapter and the results were also published[7]. On the other hand, the mechanical studies of ITO under external stress have also been widely conducted experimentally[8]. Stretching-type stress can cause ITO to crack and increase its sheet resistance [9]. However, compression-type stress could promote buckling at first, and eventually crack or delaminate when the stored energy exceeds what the film can bear. When the ITO/plastic composite film is bent, the ITO film can suffer from either compressive or tensile stress, and this depends on the way it is bent. Comparing these two types of strain conditions, people have found the increase in sheet resistance behaves asymmetrically. This might arise from the residual stress of the ITO/Plastic composite, which is usually compressive in terms of the ITO layer[10] or the different course for the cracking or buckling to the electrical resistance. Thus the two different types of stress may also change the electroluminescence (EL) of OLED device differently. Apart from these stress effects, creep[11] (which is more likely to happen to the metal thin-film and plastic substrate) and film delamination[12] are two other key factors which affect soft multilayer thin-film structures.

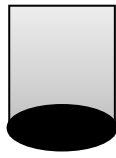
## ***7.2 Experiment***

The ITO/polyethylene terephthalate (PET) composite substrate used in this study was purchased from Sigma-Aldrich, with the ITO thickness to be 100 nm and sheet resistance to be  $60\Omega/\square$ . The substrate was then cleaned with acetone and isopropanol

in the ultrasonic bath for 7 minutes each, and exposed in the UV-Ozone Oven for another 7 minutes.

The component layers of the OLED device with the structure aluminium (100 nm)/lithium fluoride (0.8 nm)/ tris-(8-hydroxyquinoline) aluminum ( $\text{Alq}_3$ ) (40 nm)/ N,N'- Bis(naphthalen-1-yl)-N,N'-bis(phenyl)benzidine (NPB) (50 nm)/ ITO (100 nm)/ PET (0.127 mm) were deposited by evaporation under vacuum ( $2 \times 10^{-7}$  mbar) using the Kurt J. Lesker small molecule deposition system. The FOLED device was mounted on the sample holder and the brightness was measured by the Konica-Minolta LS-110 Luminance meter as shown in figure 7.1. The holder enables the device to be bent about one axis with 3 different conditions: R1 = position A, R2 = position B, and R3 = position C in both concave and convex directions. Furthermore, the device pattern (as shown in figure 6.2) was designed in order that during the bending tests, the active area (5 mm x 10 mm) was located around the furthest point of the curve from the electrical contact caused by bending, i.e., the axis referred to above was parallel to the short side and the area between the electrical contacts and the active area was relatively flat.

In order that uninterrupted optical access can be made in the “bent” positions, a 2-point bending method was used. However, this method has the disadvantage of having to define the radius of curvature at the device position ( $R_c$ ). Two methods were applied to estimate  $R_c$  for bending positions A, B, and C. First, 5 cylindrical rods were fabricated with radius 7 mm, 8 mm, 9 mm, 10 mm, and 12 mm as shown in figure 7.3, and used to compare with the curvature at the three positions. As a result,  $R_c$  for position A, B, and C are approximately 12 mm, 10 mm, and 8 mm. For confirmation, the second method was also applied in each case, but is more complicated.



Konica-Minolta LS-110  
Luminance meter

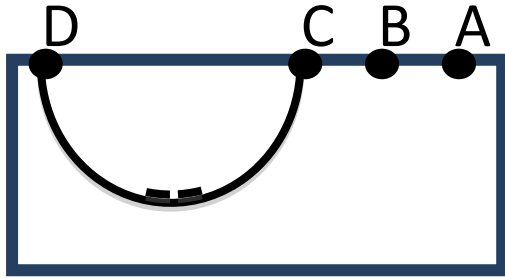


Fig. 7.1 The FOLED device was mounted and bent on the sample holder to be measured by the Konica-Minolta LS-110 Luminance meter fixed above the sample holder as shown in figure 7.1. The curved line is the FOLED device. It is fixed at the left end of the long side (position D). The dash line is the active OLED area which emits light. The right end is to be fixed at the position A, B, and C for different radius of curvature.  $\overline{DC} = 25$  mm,  $\overline{DB} = 35$  mm,  $\overline{DA} = 45$  mm.

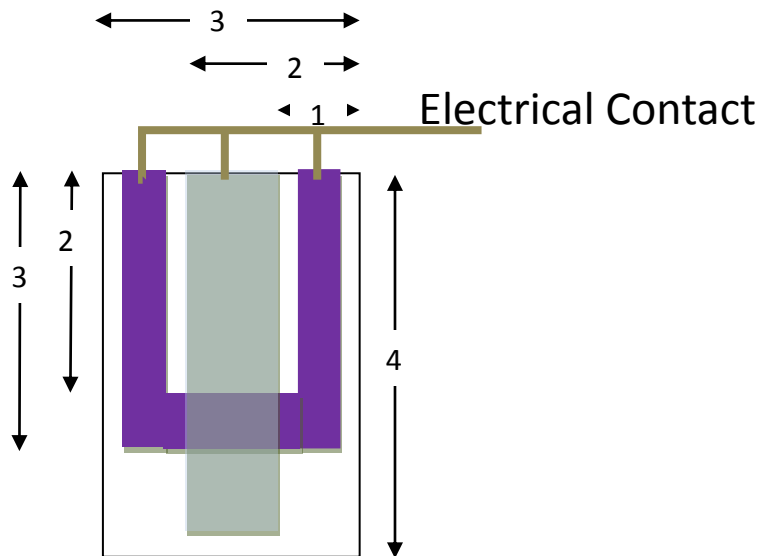


Fig. 7.2 The FOLED device plan. The darker area is the ITO layer. The lighter oblong shape covered on it is the aluminium layer. The dimensions are in unit of mm. The OLED is thermal evaporated everywhere on the 40 mm x 30 mm PET substrate and between these two electrodes. The OLED active area is 10 mm x 5 mm.



Fig. 7.3 The cylindrical rods used to estimate the bending radius of curvature of the device.

Images of the FOLED devices bent at the three positions were taken separately and input to the software Origin 7.0 with a magnification of 2.5. Three curves were then traced and centered on  $x=5$  as shown in figure 7.4, and the 2<sup>nd</sup> derivative was calculated and plotted in figure 7.5.

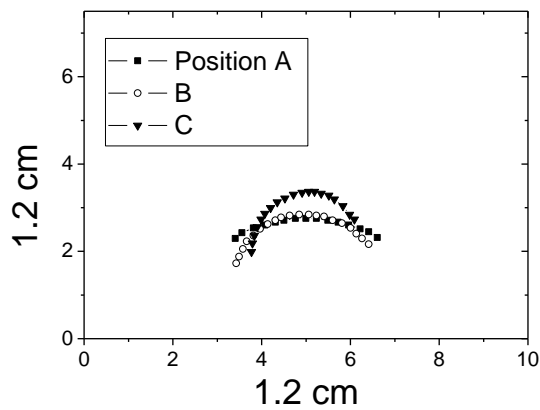


Fig. 7.4 The traced curves from the 2.5 x images of the FOLED device bent with position A, B, and C.

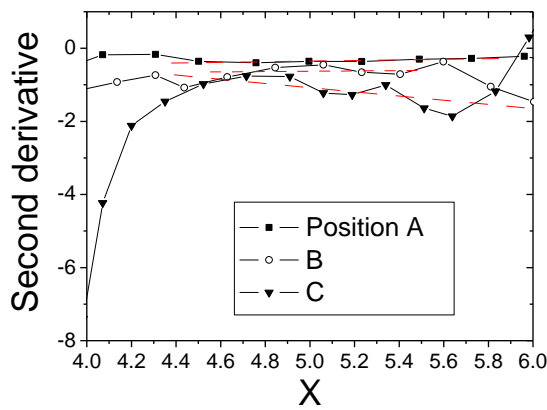


Fig. 7.5 the 2<sup>nd</sup> derivative of the curves in figure 7.4 around the active OLED area (x=5)

The semi-circle as a function of x centered on  $(x_0, y_0)$  is:

$$y(x) = y_0 + \sqrt{R_c^2 - (x - x_0)^2} \quad (7.1)$$

And the 2<sup>nd</sup> derivative of (1) when  $x = x_0$  is:

$$y''(x_0) = \frac{-1}{R_c} \quad (7.2)$$

From figure 7.5, the average of the 2<sup>nd</sup> derivative of bending position A, B, and C between  $x = 4.4$  to  $5.6$  are about  $-0.37$ ,  $-0.68$  and  $-0.8$ . Therefore the  $R_c$  of figure 7.4 are  $3.2$  cm,  $1.9$  cm, and  $1.5$  cm. But because the curves were traced from a  $\times 2.5$  image, so the real  $R_c$  of the FOLED device of bending position A, B, and C are  $12.8$  mm,  $7.6$  mm, and  $6$  mm.

Finally, when the device was bent, the focus of Konica-Minolta LS-110 Luminance meter was adjusted in order to focus on the active area and make the accurate measurement of the device brightness.

### 7.3 Results and discussion (I)

Test run	1	2	3	4	5	6	7	8	9	10	11	12	13	14	15
Rc of FOLED in Expt.1	N/A	<b>R<sub>1</sub></b>	<b>R<sub>2</sub></b>	<b>R<sub>3</sub></b>	<b>R<sub>2</sub></b>	<b>R<sub>1</sub></b>	N/A	<b>R<sub>1</sub></b>	<b>R<sub>2</sub></b>	<b>R<sub>3</sub></b>	<b>R<sub>2</sub></b>	<b>R<sub>1</sub></b>	N/A	<b>R<sub>3</sub></b>	N/A
Rc of FOLED in Expt.2	N/A	<b>R<sub>1</sub></b>	<b>R<sub>2</sub></b>	<b>R<sub>3</sub></b>	N/A	<b>R<sub>3</sub></b>	N/A								
Rc of FOLED in Expt.3	N/A	<b>R<sub>3</sub></b>	N/A	<b>R<sub>3</sub></b>	N/A										
Rc of FOLED in Expt.4	N/A	<b>R<sub>3</sub></b>	N/A	<b>R<sub>3</sub></b>	N/A										

\*  $R_1$  = position A,  $R_2$  = B, and  $R_3$  = C

Table 7.1 The experimental details about the bending curvature at different runs.

The experiments included several runs with different  $R_c$  and bending stress type as listed in table 7.1. Different devices were used for each Expt. 1, 2, 3, and 4 in order to control the defect type caused by each direction of stress. Second, the device was not encapsulated, which means the EL efficiency would decay with time under



normal operation in the air, even without bending. Consequently, the EL lifetime experiment was first conducted at a current density of  $9.4 \text{ mA/cm}^2$  (about 4.6 V and  $100 \text{ cd/m}^2$ ) as shown in figure 7.6. It showed that after about 10 minutes, the device was relatively stable at least for the next 50 minutes. Therefore, the bending experiments were only conducted after the fresh devices were operated at  $9.4 \text{ mA/cm}^2$  after 10 minutes and did not extend beyond 1 hour in duration. This ensured that the EL performance change in the experiment was mainly caused by the mechanical bending process.

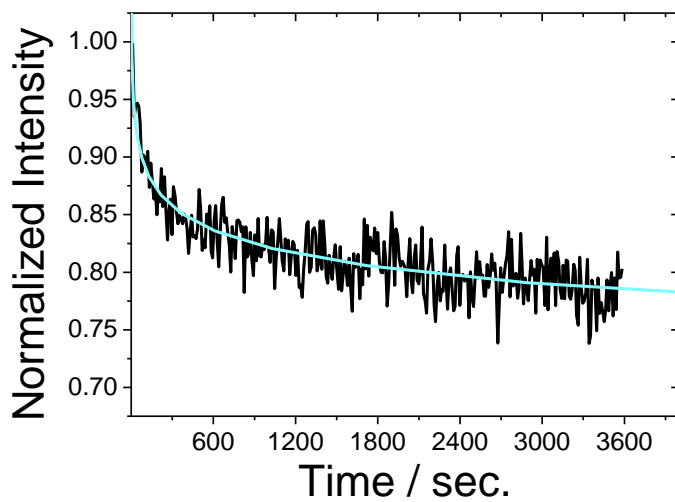


Fig. 7.6 The lifetime measurement of the non-encapsulated FOLED device under constant current supply at  $9.4 \text{ mA/cm}^2$ .

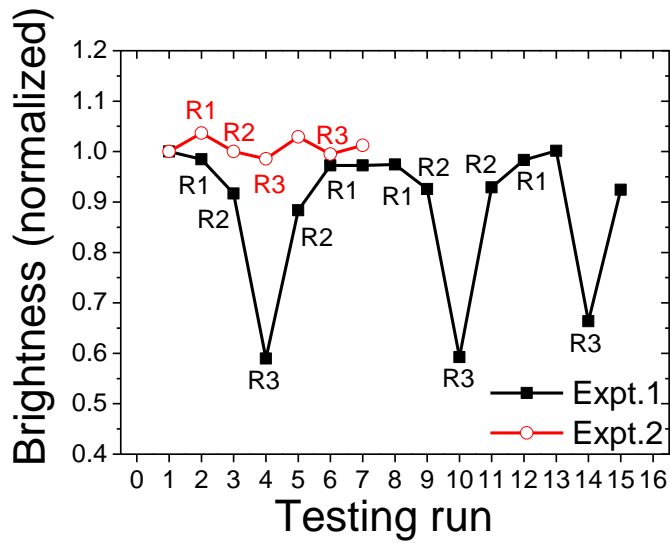


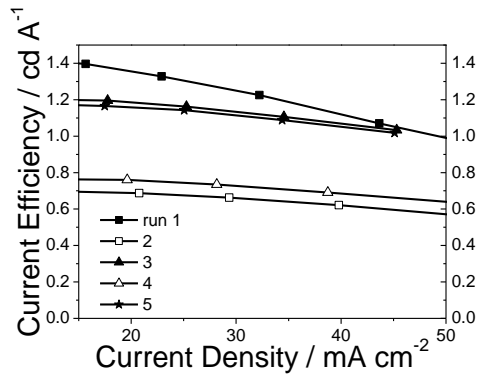
Fig. 7.7 The brightness of the FOLED device against the testing runs. In the Expt. 1 (filled square), the OLED device was given a tensile stress while in the Expt. 2 (open circle), a compressive stress.  $R_x$  denotes the radius of curvature:  $R_1 =$  position A,  $R_2 =$  B, and  $R_3 =$  C.

Figure 7.7 shows how the brightness (normalized) of the OLED device changed with the different bending conditions. The OLED was stretched in Expt.1 (filled square), and compressed in Expt.2 (open circle). With the constant current supply at  $9.4 \text{ mA/cm}^2$ , the brightness of the device in Expt.1 reduced slightly first when being stretched with  $R_c =$  position A, and lowered to 90% with  $R_c =$  position B. When it was bent more tightly with  $R_c =$  position C, the brightness drops dramatically to under 60%. It seemed that the device was sustainable under the strain up to a critical point: in this case  $R_c$  between position B and C. The strain of the thin-film caused by bending can be calculated by equation (3) if the bending is homogeneous and  $R_c$  is known.

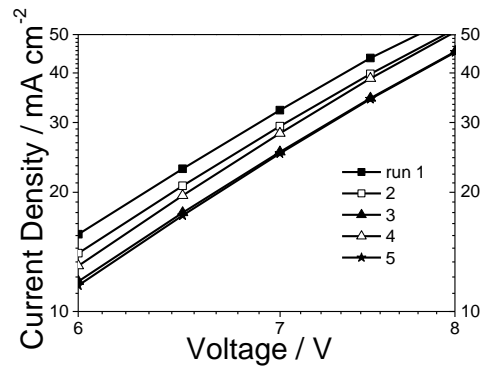
$$\varepsilon = \frac{y}{R_c} \quad (7.3)$$

$\varepsilon$  is the strain, and  $y$  is the distance between the layer and the neutral axis (see chapter 2 and 6). With the condition described of a 2 point bending method, it is assumed that

over the small area of the device, the strain produced is homogeneous. It is also assumed that the position of the neutral axis was at the midpoint of the substrate (as the substrate is much thicker than the coated films),  $y=0.0635$  mm. Therefore for the case of  $R_c = 10$  mm and 6 mm for bending position B and C, the strain of the OLED layers  $\sim 0.65\%$  to  $1\%$  respectively. After this point, one or more layers appear to crack. Candidate layers could be the ITO anode, as it is the most brittle material of the device, or the ductile aluminium cathode layer as the yield stress decreases dramatically when being as thin as 100 nm[13], or even the organic layers, of which the Young's modulus is between 60~120 GPa when being coated on a harder substrate such as the silicon wafer[14]. Surprisingly, this damage was reversible as shown in the testing runs 5 – 7 where the device was relieved gradually until completely flattened. The cycle was then repeated one more time. The brightness again was decreased to lower than 60% after the critical bending point and recovered to almost 100% in run 13 when the bending was relieved again. In the 3<sup>rd</sup> cycle, the device was bent with  $R_c =$  position C directly and relieved again in the next run. It shows that although the brightness did not drop as much as the previous two cycles, the recovery was nevertheless not complete. The damage caused by sudden hard bending seems to be more pronounced. On the other hand, when comparing run 2 and run 8 (with  $R_c =$  position A in both runs), although run 8 was after the likely severe damage caused to the device in run 4, the brightness of each run was not too different. This may be due to the fact that when the device was operated, the higher temperature allowed the layers to creep when the strain was less severe. When the OLED was compressed as in Expt.2, the brightness was almost unchanged even when  $R_c =$  position C.

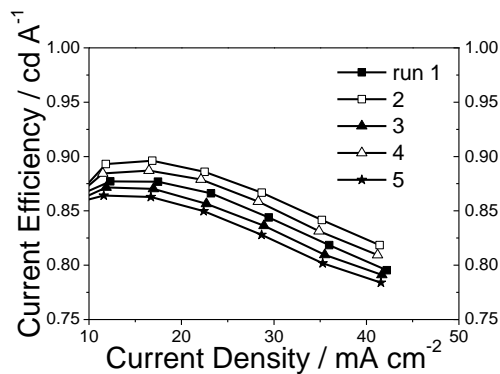


(7.8a)

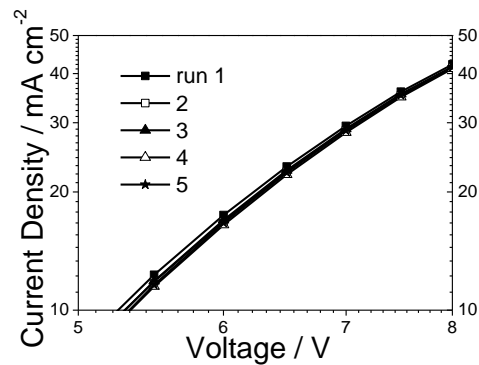


(7.8b)

Fig. 7.8a and 7.8b Current efficiency and JV characteristic of the FOLED device Expt.3 against the testing runs. The device was given a tensile stress with  $R_c =$  position C in run 2 and 4 (open symbols). The device was unbent in run 1, 3, and 5 (filled symbols).



(7.9a)



(7.9b)

Fig. 7.9a and 7.9b Current efficiency and JV characteristic of the FOLED device Expt.4 against the testing runs. The device was given a compressive stress with  $R_c =$  position C in run 2 and 4 (open symbols). The device was unbent in run 1, 3, and 5 (filled symbols).

In order to confirm this result, two more devices were tested and measured in an integrating sphere (Labsphere LMS-100), which had been calibrated according to the

FOLED sample holder, as Expt. 3 and Expt. 4 in table 7.1. The integrating sphere is a hollow spherical chamber with a highly reflective material coated on the inner surface and a small photodiode. The sample to be measured is mounted in the middle of the chamber so that ideally all the out-coupled light can be collected by the photodiode. In the figure 7.8a (Expt. 3), the device was bent in a concave manner to produce a tensile stress with  $R_c =$  position C in the run 2 and 4, and relieved in the run 1, 3, and 5. In the figure 7.9a (Expt. 4), on the other hand, the device was bent in a convex manner to produce a compressive stress with  $R_c =$  position C in the run 2 and 4, and relieved in the run 1, 3, and 5. Both experiments confirmed the two important results observed by the luminance meter in the figure 7.7: the recovery of EL when tensile stress was removed and the different response of the device EL to the opposite direction of the stress. The JV characteristic also shows no difference about whether the device was having compressive strain or not (figure 7.9b) and become less stable when having tensile strain (figure 7.9a).

To understand more about these observations, the devices were examined by atomic force microscopy (AFM) immediately after the bending experiments, and the images are shown in figure 7.10 (Expt.1) and figure 7.11 (Exp.2). The rough surfaces in the images were the typical thermal evaporated aluminium layer surface as it was the outmost layer of the device. Although it was reported that for a freestanding or polymer-supported aluminium thin-film, the rupture

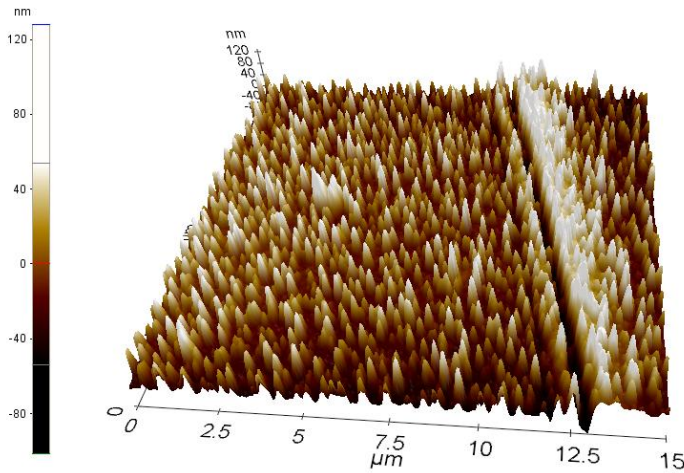


Fig. 7.10 The AFM images of the aluminum surface of the FOLED device in Expt.1 after the bending tests. The device was given a tensile stress.

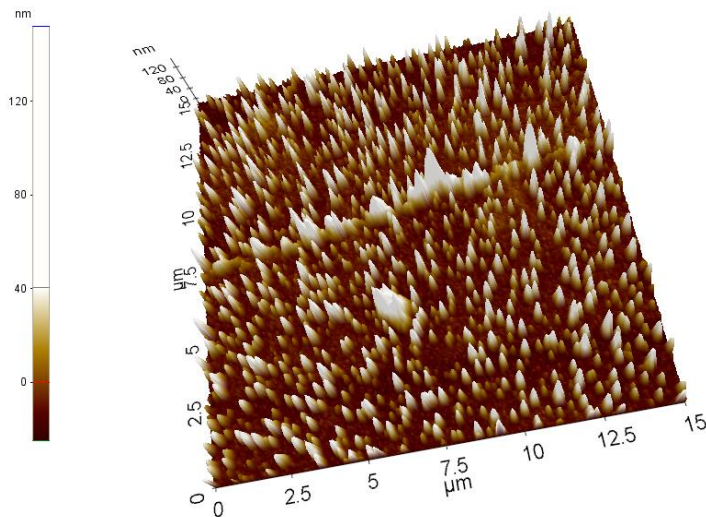


Fig. 7.11 The AFM images of the aluminum surface of the FOLED device in Expt.2 after the bending tests. The device was given a compressive stress.

strain is normally between 1% to 2% [15], which is about the maximum strain caused by bending position C in Expt.1 (~1%). Therefore the deep and clear cracks were observed in the figures 7.10. On the other hand, in the figure 7.11 only some buckle-like lines were observed, and these lines were merely rougher surfaces with taller spikes, and this may explain why the EL brightness of the Expt.2 and Expt.4 remained

relatively unchanged as shown in figure 7.7 and 7.9. Although the AFM images could only reveal the surface of the aluminium layer as it was the outermost layer, the other layers of the OLED, notably the ITO layer, might have the same types of defects, cracks or buckling, as the aluminium layer. One thing to be noticed here is that these AFM measurements were not conducted during the bending experiments but 1 to 2 hours after, therefore some cracks or buckles might recover already thus were not observable, but they still provide some information about how these two kinds of stress damaged the devices differently. It is also worth mentioning here that although the compressive strain looks harmless to the FOLED device, it did however cause the outermost aluminium layer to detach initially. The devices completely failed when being bent tighter than some critical radius. This is a known issue for multilayer thin-films when adherence of the layers is poor. But as long as the whole active area did not completely delaminate, and it was still adherent in the flat regions either side of it, i.e. it was still held in place, the layers would come back into contact when the bending moment was removed. Nevertheless, creep, which accelerates as the temperature rises as a result of the resistive heating while the device is operated, would improve the adherence. This process only takes 10's of seconds. For example, in the Expt.2 the device would completely fail initially when under a compressive strain with  $R_c =$  position C. On removing the bending moment, the device would 'repair' and work with the original EL efficiency. By operating the device for 10 to 20 seconds further at the current density of  $9.4 \text{ mA/cm}^2$  (about 4.6 V), and then bending the device with  $R_c =$  position C again, the device would then not fail but would perform as well as before the bending, as shown in curve Expt.2 of figure 7.7.

## ***7.4 Results and discussion (II)***

It has been demonstrated in the previous section that the tensile stress caused more damage to the FOLED device than the compressive stress. Now, according to the calculation in chapter 6 of this thesis, it is possible to reduce the bending stress and subsequently protect the device from bending by inserting a buffer layer, i.e. glass, between ITO and PET substrate. Since the glass-buffered ITO/PET substrate is still unavailable, the alternative composite substrate, supplied by Dupont-Teijin Film and with 4  $\mu\text{m}$  buffer layer between ITO and PET, was used in the mechanical study here. Dupont-Teijin would not disclose fully the material used as the buffer, so we only know it is made of some epoxy type of annealed polymer. However the plain PET film coated with such material as the planarization layer was also supplied as a reference, so this gives us the chance to study the Young's modulus of this buffer layer.

The nano-indentation measurement was conducted for the BL( $\sim 1\mu\text{m}$ )/PET composite film, which was stuck on the silicon wafer, and the curve of reduced elastic modulus against contact depth ( $h_c$ ) is shown in figure 7.12. When  $h_c$  is 750 nm, the elastic property is dominated by the PET substrate, which is about 4-5 GPa, and when  $h_c$  approaches to the surface, the modulus begins to reflect the elastic property of the buffer material, which is between 9-10 GPa. Although one has to bear in mind that the real value might be larger when the measured object was coated on the softer base according to what we have learned in the chapter 5.



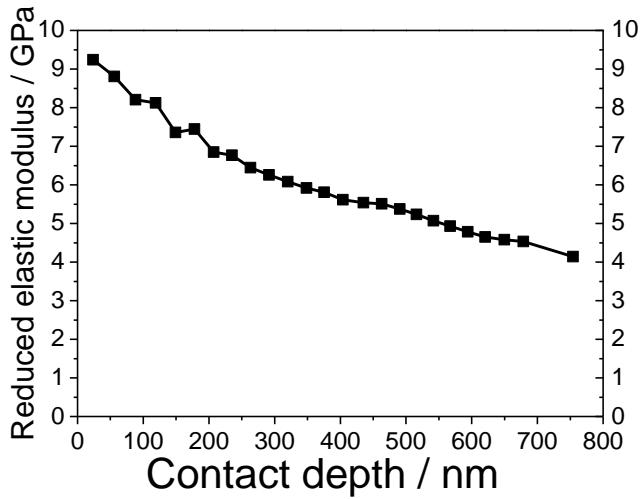


Fig. 7.12. The reduced elastic modulus of the buffer material vs. the contact depth.

Using the simulation method introduced in the chapter 6, with the reduced elastic modulus of the PET, BL, ITO, OLED, and metal being 4, 10, 120, 80, and 78 GPa respectively, and the thickness of each layer being 0.12 mm, 4  $\mu\text{m}$ , 100 nm, 100nm, and 100 nm, and assume the bending radius of curvature is 8 mm, the stress in the ITO of the FOLED device is then calculated and plotted in figure 7.13. It is seen that the stress in ITO has its minimum when the BL is  $\sim 6 \mu\text{m}$ , and with the thickness of BL of 4  $\mu\text{m}$ , the stress in ITO reduced for  $\sim 1\%$ .

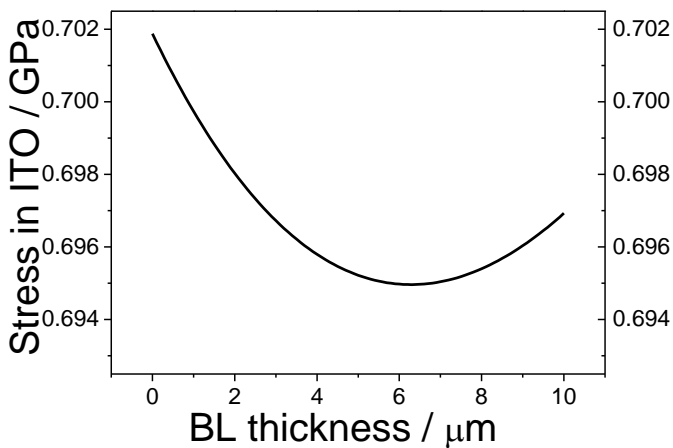


Fig. 7.13. The stress in ITO varies depending on the thickness of the buffer layer.

Test run	1	2	3	4	5	6	7	8	9	10	11	12	13	14	15	16	17
Rc of FOLED in Expt.5	N/A	<b>R<sub>1</sub></b>	<b>R<sub>2</sub></b>	<b>R<sub>3</sub></b>	<b>R<sub>2</sub></b>	<b>R<sub>1</sub></b>	N/A	<b>R<sub>1</sub></b>	<b>R<sub>2</sub></b>	<b>R<sub>3</sub></b>	<b>R<sub>2</sub></b>	<b>R<sub>1</sub></b>	N/A	<b>R<sub>3</sub></b>	N/A	<b>R<sub>3</sub></b>	N/A
Rc of FOLED in Expt.6	N/A	<b>R<sub>1</sub></b>	<b>R<sub>2</sub></b>	<b>R<sub>3</sub></b>	<b>R<sub>2</sub></b>	<b>R<sub>1</sub></b>	N/A	<b>R<sub>1</sub></b>	<b>R<sub>2</sub></b>	<b>R<sub>3</sub></b>	<b>R<sub>2</sub></b>	<b>R<sub>1</sub></b>	N/A	<b>R<sub>3</sub></b>	N/A	<b>R<sub>3</sub></b>	N/A
Rc of FOLED in Expt.7	N/A	<b>R<sub>1</sub></b>	<b>R<sub>2</sub></b>	<b>R<sub>3</sub></b>	N/A	<b>R<sub>3</sub></b>	N/A	<b>R<sub>3</sub></b>	N/A								

Table 7.2 Table 7.1 The experimental details about the bending curvature at different runs.

Three devices (Expt.5, 6 and 7) fabricated on the BL(4 $\mu$ m)/PET with the structure of aluminium (100 nm)/lithium fluoride (0.8 nm)/ Alq<sub>3</sub> (40 nm)/ NPB (50 nm)/ ITO (100 nm)/ BL(4 $\mu$ m)/ PET (0.127 mm), and the EL brightness were measured at different tensile stress by R<sub>c</sub> (radius of bending curvature) as shown in table 7.2. The curves of the normalized brightness variation in each run together with the reference device (Exp.1) are shown in figure 7.14. It is found that both Expt.5 and 6 devices show a better resistance to the tensile stress than the device Expt.1: the brightness dropped 10-15% at R<sub>c</sub> = R<sub>3</sub> for devices with the BL compares to 40% at the same R<sub>c</sub> for device without the BL.

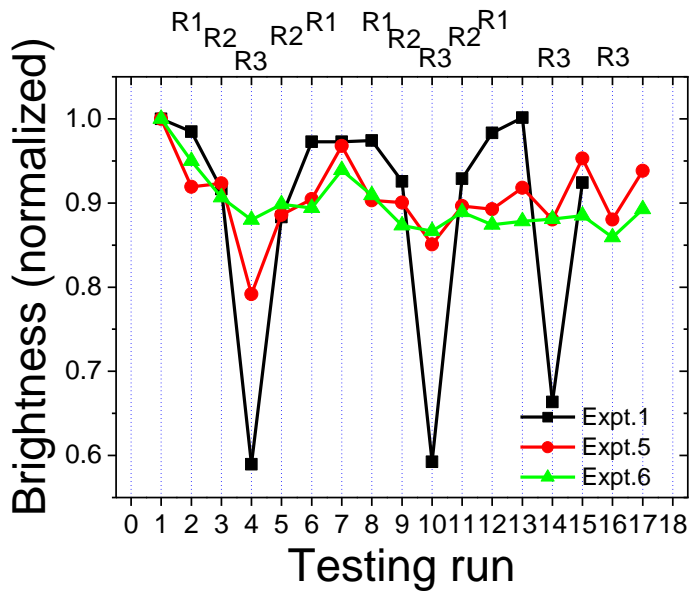


Fig. 7.14 The normalized brightness of the FOLED device against the testing runs when OLED layers were given a stretched strain. The Expt. 1 (filled square) is the reference device and the Expt. 5 (open circle) and 6 (filled triangle) shows the devices with  $4\mu\text{m}$  thick of buffer layer.

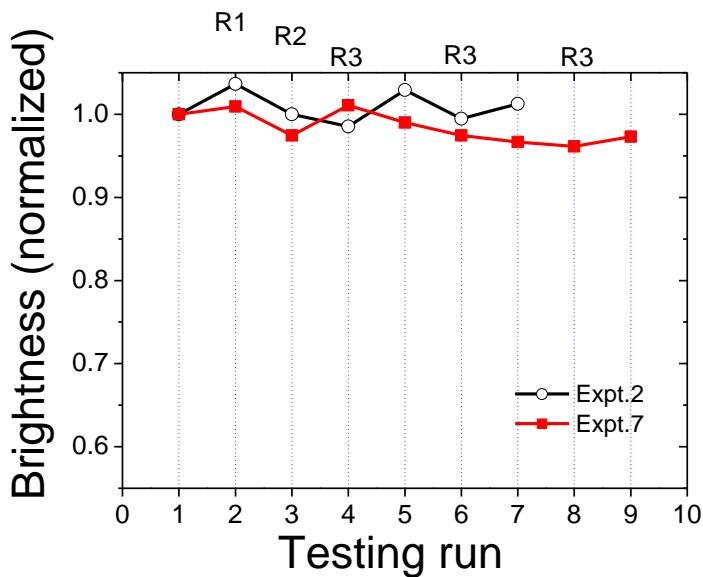


Fig. 7.15 The normalized brightness of the FOLED device against the testing runs when OLED layers were given a compressive strain. The Expt. 2 (open circle) is the

reference device and the Expt. 7 (filled square) shows the devices with 4 $\mu$ m thick of buffer layer.

The surface of the aluminum cathode of the device Expt. 5 and 6 were also examined with the optical microscope as shown in the figure 7.17. Not surprisingly, the surface looks unharmed after the tensile stresses were applied and no cracks were found when surfing through the whole device surface. One can ask how this 1% decrease of the stress in the FOLED layers can make such a big difference? First, when  $R_c = 8$  mm, the stress in 100 nm thick aluminum thin-film might have surpassed its yield stress as shown in the figure 7.16, which means the plastic deformation has occurred during the bending experiment. Therefore any reduction of the stress can help to reduce the possibility of cracking. Secondly, the value of the Young's modulus of the BL material might be underestimated due to the limit of the experimental method. Further simulation of the stress in ITO with BL Young's modulus of 20 and 30 GPa showed a dramatic decreasing of the stress by 8.6% and 14.3% respectively. So this again shows the importance of choosing the BL with the right elastic property. A small difference and make a huge effect to the device mechanically.

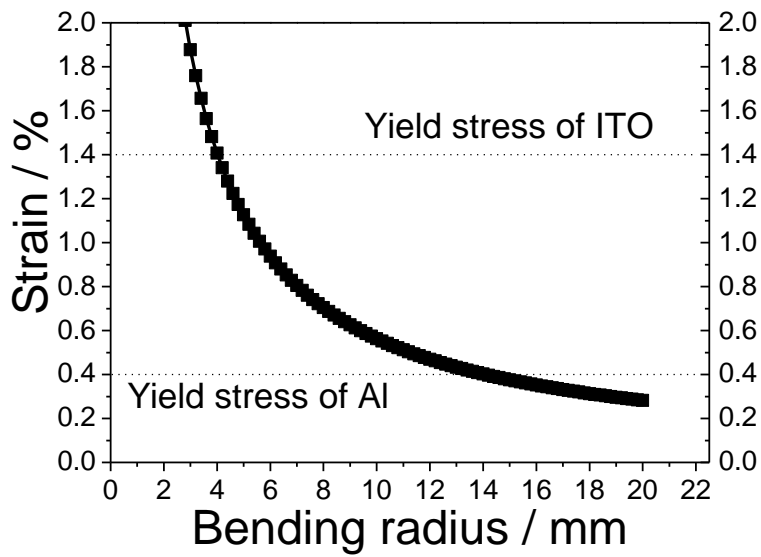


Fig.7.16. Strain of the OLED thin-films (including ITO and Al) vs.  $R_c$  for the device structure: aluminium (100 nm)/ OLED (100 nm)/ ITO (100 nm)/ BL(4 $\mu$ m)/ PET (0.127 mm).

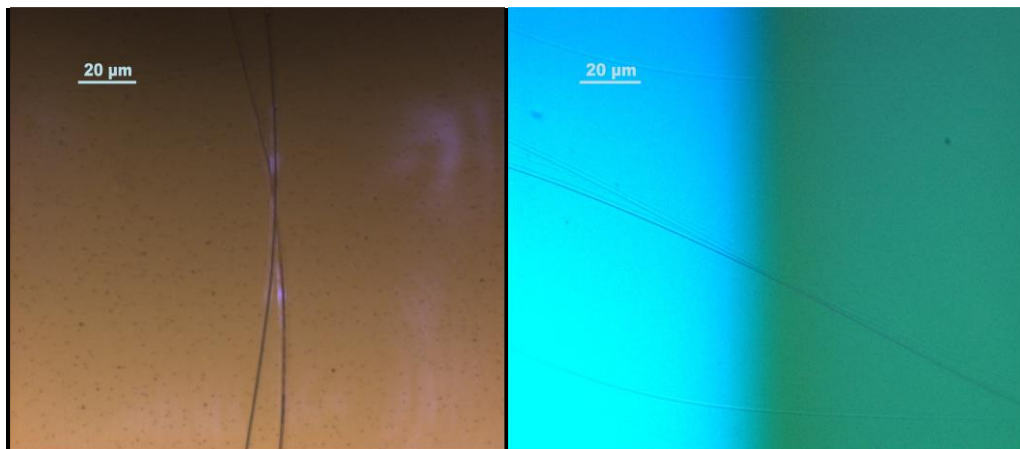


Fig.7.17. Microscopy image of the aluminum surface of the device Expt.1 (left) and Expt.5 (right). Cracks caused by bending can be observed clearly on device Expt.1, while on the device Expt.5, there were only some scratches observed.

## 7.5 Summary

It has been shown here that the conventional bottom emitting FOLED device can work with at least 90% of the original efficiency when the OLED layers were

subjected to bending in a cylindrical sense about one axis and given a tensile stress with  $R_c =$  position B, and almost 100% of the original efficiency when given a compressive stress with  $R_c =$  position C. The damage caused by the bending is reversible. For the case of tensile stress (stretching), the device recovered better when bending was applied slowly and step by step from  $R_c =$  position A to C. When it was bent with  $R_c =$  position C directly, the device only recovered to 95% after the bending was removed. For the case of compression, one possibility may be that the aluminium cathode detaches initially when being bent with  $R_c =$  position C. But after the bending is relieved and the device operated for another 20 seconds at the current density of  $9.4 \text{ mA/cm}^2$  (about 4.6 V), thus giving the aluminium layer enough time to creep, the device could function while being bent with  $R_c =$  position C, and with the same efficiency as before the bending.

For the FOLED devices with the  $4\mu\text{m}$  thick BL inserted between the ITO and PET substrate, the reducing of brightness caused by the tensile stress at  $R_c = R_3$  improved from 40% to 10-15%. The microscopy study of the aluminum surface also suggested the device was prevented from cracking during the bending test. This proves that with the proper choice of BL material and thickness, the FOLED devices can be protected from bending either at the roll-to-roll manufacture process or the daily use of the bendable light-emitting products.

To reduce the critical bending radius of curvature further and block the oxygen and water outside of the device, glass as the buffer material is still desirable. In addition, to avoid delamination when a compressive stress is applied, the adhesion of the OLED layers needs to be improved.

## 7.6 References

- [1] C. W. T. a. S. A. Vanslyke, "Organic electroluminescent diodes," *Applied Physics Letters*, vol. 51, pp. 913-915, 1987.
- [2] Y. C. Yang and D. K. Yang, "Wider viewing angle in in-plane switching mode Liquid crystal displays by self-compensated phase retardation films," in *2009 Sid International Symposium Digest of Technical Papers, Vol Xl, Books I - Iii*, J. Morreale, Ed. Campbell: Soc Information Display, 2009, pp. 1563-1566.
- [3] Y. C. Lu, C. S. Cheng, C. J. Hu, C. M. Chang, F. Y. Gan, and Sid, "New multi-domain vertical alignment LCD with high contrast ratio," in *2007 Sid International Symposium, Digest of Technical Papers, Vol Xxxviii, Books I and Ii*. vol. 38 Playa Del Rey: Soc Information Display, 2007, pp. 725-727.
- [4] F. M. Dheurle and J. M. E. Harper, "Note on the origin of intrinsic stresses in films deposited via evaporation and sputtering," *Thin Solid Films*, vol. 171, pp. 81-92, Apr 1989.
- [5] C. H. Hsueh, "Thermal stresses in elastic multilayer systems," *Thin Solid Films*, vol. 418, pp. 182-188, Oct 2002.
- [6] C. J. Chiang, C. Winscom, S. Bull, and A. Monkman, "Mechanical modeling of flexible OLED devices," *Organic Electronics*, vol. 10, pp. 1268-1274, Nov 2009.
- [7] G. P. Crawford, "flexible flat panel displays," in *Wiley-SID Series in Display Technology*, A. C. Lowe, Ed. Brown University, USA: John Wiley & Sons, Ltd, 2005, pp. 99-120.
- [8] S. K. Park, J. I. Han, D. G. Moon, and W. K. Kim, "Mechanical stability of externally deformed indium-tin-oxide films on polymer substrates," *Japanese Journal of Applied Physics Part I-Regular Papers Short Notes & Review Papers*, vol. 42, pp. 623-629, Feb 2003.
- [9] Y. Leterrier, L. Medico, F. Demarco, J. A. E. Manson, U. Betz, M. F. Escola, M. K. Olsson, and F. Atamny, "Mechanical integrity of transparent conductive oxide films for flexible polymer-based displays," *Thin Solid Films*, vol. 460, pp. 156-166, Jul 2004.
- [10] C. F. Y. Leterrier, L. Médico, F. Demarco, J.-A. E. Månson, P. Bouten, J. DeGoede, and J.A. Nairn and Nairn, "Mechanical properties of transparent functional thin films for flexible displays," in *46th Annual Technical Conference Proceedings: Society of Vacuum Coaters 505/856-7188*, 2003.
- [11] J. S. L. William N. Findley, and Kasif Onaran, *Creep and Relaxation of Nonlinear Viscoelastic Materials with an Introduction to Linear Viscoelasticity* vol. 18. Amsterdam, New York, Oxford.: North-Holland Publishing Company, 1976.
- [12] S. Li, J. Wang, and M. D. Thouless, "The effects of shear on delamination in layered materials," *Journal of the Mechanics and Physics of Solids*, vol. 52, pp. 193-214, Jan 2004.
- [13] G. T. Mearini and R. W. Hoffman, "Tensile properties of aluminum/alumina multi-layered thin films," *Journal of Electronic Materials*, vol. 22, pp. 623-629, Jun 1993.

- [14] C. J. Chiang, S. Bull, C. Winscom, and A. Monkman, "A nano-indentation study of the reduced elastic modulus of Alq(3) and NPB thin-film used in OLED devices," *Organic Electronics*, vol. 11, pp. 450-455, Mar.
- [15] T. Li, Z. Y. Huang, Z. Suo, S. P. Lacour, and S. Wagner, "Stretchability of thin metal films on elastomer substrates," *Applied Physics Letters*, vol. 85, pp. 3435-3437, Oct 2004.



## *Chapter 8*

### *Conclusion*

During the year 2010, whilst finalizing this thesis, the progress of OLED technology has drawn the attention of the web media. The proliferation of news and rumors, such as which manufacturers are using OLED for their latest device or which manufacturer will produce OLED lighting panel at as early as 2011, has gradually convinced people that OLED is closer than ever to becoming a widespread technology. In display applications, having a device with a super-OLED display is increasingly normal in daily life, although the production of OLED panels is still far below the required level to meet the strong demand.

In the mean time, despite the fact that they are not expected to be available in foreseeable future, the “flexible OLED” already generates 210 results when entered into YouTube today: A clip of the 4.1-inch rollable OLED display prototype with a resolution of 432 by 240 pixels released by SONY has over 200,000 hits in less than 5 months . All of the above imply that the mass production of glass-based rigid OLEDs is just a matter of time. The issues that remain to be solved are more engineering than the academic in nature.

On the other hand, there are still questions about the viability of rigid-OLED technology in displays due to the recent developments of the super-LCD. Therefore

making an OLED device on flexible substrates is a critical strategy to exploit the uniqueness of the OLED technology. A plastic-based OLED is so lightweight that the large area panel on the ceiling seems to be more reasonable. It also saves money and is more beneficial to the environment at the same time when it comes to transportation. The flexibility in shape also allows new applications to be developed. Finally, the flexible substrate makes a roll-to-roll fabrication process possible. These make this thesis, which is focused on the electrical and mechanical characterizations of flexible OLED devices fabricated by evaporation, a reasonable starting point to understand the issues that FOLED will face. It has been shown in chapter four that if the OLED structure is fixed and only the ITO/PET substrate was used to replace the ITO/glass substrate, the brightness of the FOLED device is reduced by ~ 50% compared to the rigid OLED. Out of the 50% reduction, 20% was contributed by the micro-cavity effect due to the different ITO thickness, 10% by the lower transmittance of the ITO/PET substrates and the remaining 20% by the lower injecting current due to the rougher ITO surface on the ITO/PET substrate and the poorer electrical contact for the soft base.

The first issue of the microcavity effect can be solved by optimizing the ITO thickness for the FOLED device, hence even when the current ITO low-temperature sputtering technique is still used and the roughness and the transmittance remains poor, the FOLED device can achieve 70% of the rigid-OLED brightness with the same applied voltage.

When transferring to flexible substrate, some common concerns have been that the coefficients of thermal expansion are mismatched between PET and ITO layers and the small molecules are not ductile enough for bending. Since the latter is a more

serious issue for FOLED as explained in the chapter 6, the elastic properties of Alq<sub>3</sub> and NPB were investigated in order to calculate the mechanical stress in the thin films of the device. The results suggest that it is likely that metal-based small molecules, such as Alq<sub>3</sub>, should be avoided because Alq<sub>3</sub> has a Young's modulus of ~ 100 GPa, which is close to ITO. NPB, on the other hand, has a Young's modulus of ~40 to 60 GPa, between the PET and ITO and close to aluminum thin-film. So it is still considered to be suitable for FOLED devices.

Nevertheless, even when using brittle materials such as Alq<sub>3</sub> and ITO for the OLED, the bending experiment in Chapter Seven shows that when the bending direction is favourable, i.e. producing compressive strain on the OLED layers rather than tensile strain, the FOLED device can perform at almost 100% of its unfolded output when being bent such that the radius of curvature is down to 8 mm. When tensile strain was applied, the brightness reduced to 60% when the radius of curvature was 8mm. The simulation in the Chapter Six predicted that a proper buffer layer inserted between ITO and PET can decrease the stress in the ITO, as well as OLED layers. In theory, the best buffer material would be glass. But the buffer material coated by Dupont-Teijin Films also successfully reduced the damage caused by bending as the simulation had predicted; the brightness drops to 85% when given a tensile strain compared to 60% when without the buffer layer.

Although the use of ITO as the anode has been disputed due to its brittleness, this thesis has shown that ITO/PET based FOLED devices are not only competitive to the rigid-OLEDs in EL performance and weight, but they also have the capability to be bent hard with the proper buffer layer and in the direction which produce compression on the device layer.

Although Polymer OLED is still seen as the final form of OLEDs in the flexible regime, the relatively mature industrial techniques of evaporated OLED has lowered the technical barrier to make the transfer to flexible substrates easily. This study suggests that evaporated OLED devices with ITO as the anode is still a suitable choice to allow an accelerated route to market for flexible lighting and displays.